Escape from Flatland:
strain and quantum size effect driven growth of metallic nanostructures

Tjeerd Bollmann

Committee members:

Prof. dr. G. van der Steenhoven	University of Twente (chairman)
Prof. dr. ir. B. Poelsema	University of Twente (promotor)
Prof. dr. J.W.M. Frenken	Leiden University (co-promotor)
Dr. R. van Gastel	University of Twente (assistent promotor)
Prof. dr. ing. A.J.H.M. Rijnders	University of Twente
Prof. dr. ir. H.J.W. Zandvliet	University of Twente
Prof. dr. rer. nat. W. Daum	Technical University of Clausthal
Dr. F. Meyer zu Heringdorf	University of Duisburg-Essen

This work is part of the research programme of the Foundation for Fundamental Research on Matter (FOM), which is part of the Netherlands Organisation for Scientific Research (NWO).

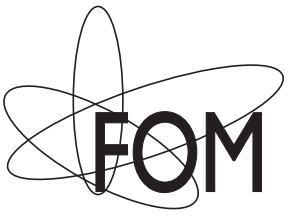

T.R.J. Bollmann
Escape from Flatland:
strain and quantum size effect driven growth of metallic nanostructures
ISBN 978-90-365-3226-6
DOI 10.3990/1.9789036532266

Published by the Physics of Interfaces and Nanomaterials Group, University of Twente.

On the titel: *'Flatland: A Romance of Many Dimensions' is an 1884 satirical novella by E.A. Abbott. It describes the adventures of A. Square, being visited by a Sphere, appearing as a circle in the fictional two-dimensional world of Flatland. He introduces his new apostle to the idea of a third dimension, hoping to eventually educate Flatlands population on the existence of Spaceland. On his question whether there could be more than three dimensions, the Sphere returns his student to Flatland in disgrace.*

Flip books: *Even pages, Pb/Ni(111) mesas reshape into hemispheres (Ch. 6). Odd pages, BiNi nanowire and QSE driven structure growth for Bi/Ni(111) (Ch. 3&4).*

Author email: tjeerd.bollmann@gmail.com

ESCAPE FROM FLATLAND:

STRAIN AND QUANTUM SIZE EFFECT DRIVEN GROWTH OF METALLIC NANOSTRUCTURES

PROEFSCHRIFT

ter verkrijging van
de graad van doctor aan de Universiteit Twente,
op gezag van de rector magnificus,
prof. dr. H. Brinksma,
volgens besluit van het College voor Promoties
in het openbaar te verdedigen
op vrijdag 23 september 2011 om 12.45 uur

door

Tjeerd Rogier Johannes Bollmann
geboren op 8 november 1982
te Doetinchem

Dit proefschrift is goedgekeurd door de promotores:
Prof. dr. ir. B. Poelsema
Prof. dr. J.W.M. Frenken
en door de assistent-promotor:
Dr. R. van Gastel

Contents

1 Introduction

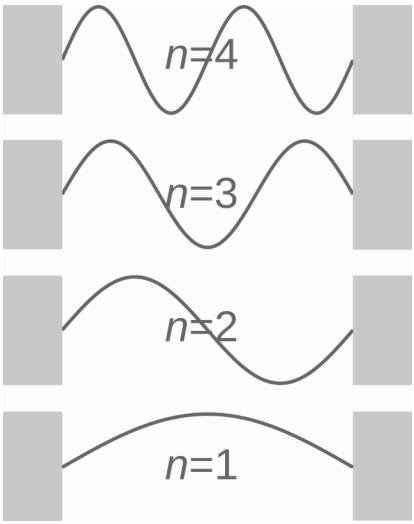

"Gott schuf die Materie, aber die Oberfläche ist ein Werk des Teufels!"

Wolfgang Ernst Pauli

"If you think you understand quantum mechanics, you don't understand quantum mechanics."

Richard Feynman

1.1 Thin film growth

Thin film growth is governed by a delicate balance between thermodynamic parameters such as surface and interface free energies and misfit related stress of both substrate and adsorbate as well as kinetic parameters such as surface diffusion and deposition rate. In the case that kinetic limitations can be easily overcome, characteristic strain stabilized growth modes may occur shown by the cartoons in Fig. 1.1. When adatoms attach preferentially to surface sites, layer-by-layer or Frank-van der Merwe growth occurs. The opposite case, stronger adatom-adatom interactions than those of the adatom with the surface results in large elastic strain, leading to 3D Volmer-Weber growth. The intermediate case, where a non-zero lattice mismatch results in increasing stress as we grow thicker films, can lead to 3D Stranski-Krastanov growth. The delicate interplay between strain stabilized nanostructures can be further complicated by surface alloying effects, that can even result in self-organization [1]. A typical example of this is the stripe phase formation of Pb on Cu(111) lead by a competition between a PbCu surface alloy and a Pb overlayer phase [2].

In the 1990s a novel growth mode was found, which resembles Stranski-Krastanov growth, but is qualitatively different from the classical growth modes in that quantum size effects (QSEs) seem to dominate any strain contributions, leading to non-trivial smooth film growth described as electronic or quantum growth, shown in Fig. 1.1(d). The deposition of Ag on GaAs at low temperatures, followed by heating to RT, results in atomically flat 6 layer thick films, with holes exposing the bare substrate. Similar behavior was found for the deposition of Pb on Si(111), leading to flat top islands with steep edges (mesas) and strongly preferred heights [3]. Depending on the semiconducting or metallic nature of the substrate, a wetting layer can be found passivating the substrate followed by the growth of QSE stabilized mesas. Exploiting the quantum mechanical principles while tuning and assembling these nanostructures, offers a whole range of opportunities to explore the properties of precisely controlled functional nanomaterials.

1.2 QSE and thin film formation

Figure 1.1(d) illustrates the basic physics of QSEs affecting the growth and stability of thin films. In the exceptional case for a Fermi wavelength similar to the interlayer distance, the electronic states perpendicular to the thin film resemble the one-dimensional 'particle-in-a-box' known from introductory quantum mechanics. The wave function is expected to be quantized along the film normal as $d = n\lambda/2$ with $n \in \mathbb{N}_0$, d the thickness of the film and λ the electron wavelength. At the Fermi level, the general quantization condition becomes $d = n\lambda_F/2$ with λ_F the Fermi wavelength that shows a $\lambda_F/2$ oscillation resulting from empty subbands shifting through the Fermi level with increasing thickness, see e.g. the

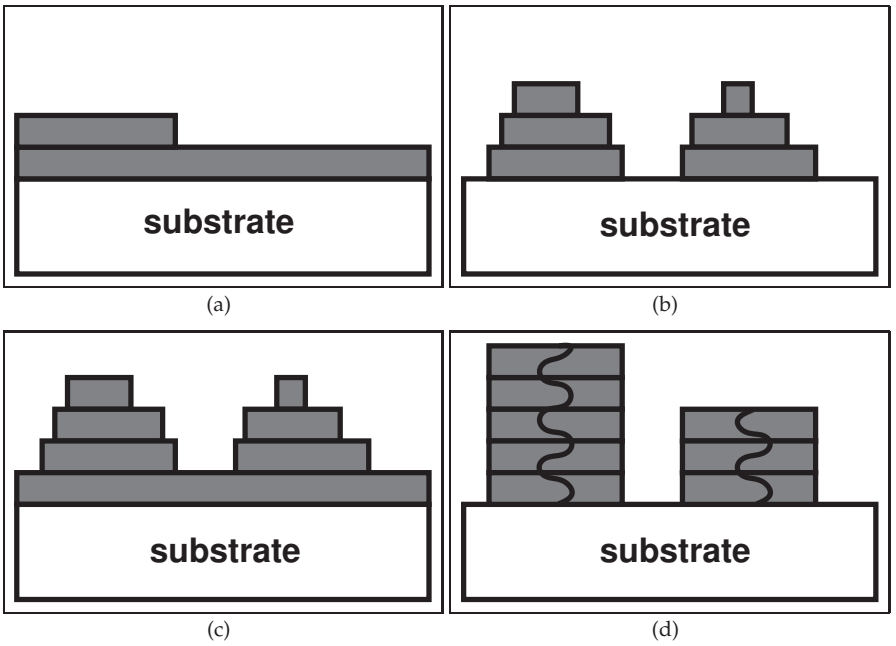

FIG. 1.1: Schematic illustrations of the Frank-van der Merwe (a), Volmer-Weber (b), Stranski-Krastanov (c) and Quantum (d) growth modes. An example of the quantization condition of λ_F along the film normal is shown in (d).

band structure for a few layer high Pb film in Ref. [4]. It is not a priori obvious whether these quantum oscillations can be observed experimentally, since it depends on the commensurability of the interlayer distance. An example of Fermi wavelengths accommodating thin film structures is shown in Fig. 1.1(d).

Thin film (meta)stability is found for electronic compressibility in the case that $\partial^2 E_S/\partial^2 d > 0$, where E_S is the surface energy per unit area for a film of thickness d. Therefore a minimum of the Friedel oscillations coinciding with the film thickness can result in an additional energy gain. This can in turn result in certain thicknesses to be stable exhibiting thereby smooth film growth with certain QSE stabilized heights [5].

The predictive power of the simple free electron model is shown in experiments where the Fermi surface is 'tailored' by the substitution of Pb with Bi atoms to achieve a specific beating wavelength, see also Fig. 1.2. The electron density is increased through the addition of valence electrons (n_e) of Bi. This results in an increasing Fermi wave vector $k_F = \sqrt[3]{3\pi^2 n_e}$ with an increasing beating period, since the commensurability of k_F to the interlayer distance is not perfect. Although the free electron model is able to describe the oscillation pattern quite well, it is too crude to predict the exact stable film thicknesses [3, 6].

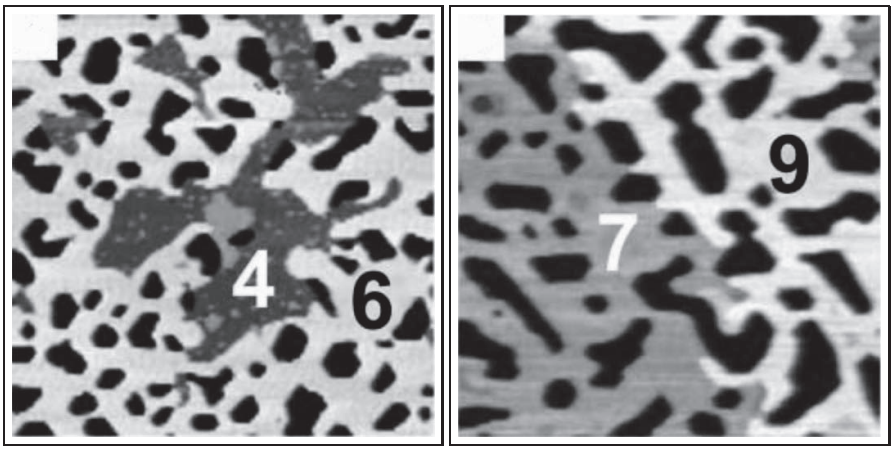

(a) (b)

FIG. 1.2: Scanning Tunneling Microscope (STM) images 400×400 nm^2 in size, revealing the quantum growth mode of $Pb_{89}Bi_{11}$ alloy films, with bilayer growth for 4 and 6 layers (a) crossing even-odd to 7 and 9 layers (b) thicknesses. The observed beating period is 13 atomic layers. The black pores in these high-resolution images are uncoated regions extending down to the wetting layer. The images were taken from [13].

In this emerging field, the growth of thin Pb(111) films has attracted particular interest. For this soft metal, electronic effects can (more) easily dominate over strain contributions. The role of QSE and Friedel oscillations is amplified by a Fermi wavelength that is nearly commensurate to the bilayer atomic spacing along the (111) direction. On top of a Si(111) and Ge(111) substrate passivated by a wetting layer, the stable island heights of 5, 7, 9, 11, 13*14, 16, 18, 20, 22*25 atomic layers, where the asterisk marks the even-odd crossovers [3], exhibit strong height-dependent oscillations in the workfunction [5, 7], interlayer distances [5, 8], superconductivity [9, 10], rate processes [11], oscillating Kondo temperatures [12], etc. Pb(111) films are rather special in that their Friedel surface oscillations decay as $1/z$ due to the Fermi surface nesting along the (111) direction, where for other known materials they decay as $1/z^2$ [5]. Therefore QSE driven growth of Pb(111) can persist even over 30 layer thick films.

1.3 Surface science with LEEM

Low Energy Electron Microscopy (LEEM) is a relatively new microscopy technique which is capable of direct imaging of surfaces at high resolutions up to 1-2 nm using aberration correctors [14–17]. Among competing real space imaging techniques, Scanning Electron Microscopy (SEM) lacks the surface specificity and surface diffraction capabilities of LEEM. Scanning Tunneling and Atomic

Force Microscopy (STM and AFM) do offer atomic resolution but lack the ability for direct imaging areas of microns in size as well as for operation at elevated temperatures.

Using the in situ capabilities of LEEM imaging in combination with its possibility to measure selected area Low Energy Electron Diffraction (μLEED), we are able to shine light on the processes that play a role in thin film growth up to a lateral resolution of about 7 nm in our instrument. By using LEEM we are able to image the growth of different nanostructures in real-time with an image size, referred to as Field-of-View (FoV), of 2-150 μm in diameter. Combination with (I/V-)μLEED measurements, where the intensity is measured while varying the incident electron energy, probing the ordering of the nanostructures can give us more insight on the properties of them. By comparing I/V-(μ)LEED measurements to Tensor LEED calculations, we can obtain information on the atomic species and positions of the atoms in the nanostructures on the surface as well. Measuring I/V-LEEM curves for the different nanostructures can also easily reveal QSEs through quantum interference peaks, in addition to (some) band structure properties. Therefore, LEEM is apart from its lack of atomic resolution, a very well suited instrument to measure both qualitative and quantitative properties of thin metal films and nanostructure growth.

1.4 Scope and outline of this thesis

This thesis is the result of over 4 years of research using the LEEM at the University of Twente. The subject of this thesis is to gain insight in the processes that lead to the self-organization of thin films and nanostructures, by studying their growth and properties. We investigated the growth of thin metal layers and nanostructures on both Ni(111) and W(100) surfaces using a combination of (I/V-)LEEM and (I/V-)μLEED measurements in combination with modeling and Tensor LEED calculations.

In Chapter 2 the experimental LEEM setup is discussed along with its possibilities. We also describe the cleaning procedures used for the Ni(111) and W(100) samples.

Chapters 3 and 4 comprise the experimental work on the growth of Bi on Ni(111). Chapter 3 focuses on the QSE driven growth and structure modifications of Bi films and their characterization. Perfectly accommodated Fermi wavelengths are found, indicative of not only quantized heights, but also of film structures driven by the QSE. The growth and characterization of both the Bi wetting layer and BiNi nanowires as well as their influence on meandering substrate steps is described in Chapter 4.

Chapter 5 and 6 comprise the experimental work on the growth of Pb on Ni(111). In Chapter 5, we discuss the growth and characterization of the Pb bidomain wetting layer, in which small Pb islands show QSE driven transitions measured in situ with LEEM. Qualitative agreement for the quantum and band

structure interference peaks is discussed. An unanticipated observation is highlighted in Chapter 6, where these about 40 layer high Pb islands decay within 1 - 10 ms by slowly heating them, to form compact 3D-structures. The involved mass transfer rates are many orders of magnitude higher than the maximum rates expected from traditional statistical physics. The origin of this novel phenomenon is nailed down to a subtle temperature induced instability in the bidomain wetting layer, which initiates an ultrafast transformation of the Pb mesas into their equilibrium shape.

The dessert, Chapter 7, reports on the growth and characterization of pseudomorphic and hut shaped Cu structures on W(100). The growth is discussed in view of stress and strain due to the lattice mismatch.

Three appendices are added where we describe the temperature calibration in our LEEM setup using the uphill flow of steps by sublimation, the comparison of Tensor LEED calculations to measured I/V-(μ)LEED curves and image analysis techniques. Since visual inspection is a comparative (not quantitative) process which is easily biased, we use the described computer techniques to enable us to quantify and visualize. It also enables us to measure features or trends which are not directly visually perceivable.

Experimental

2

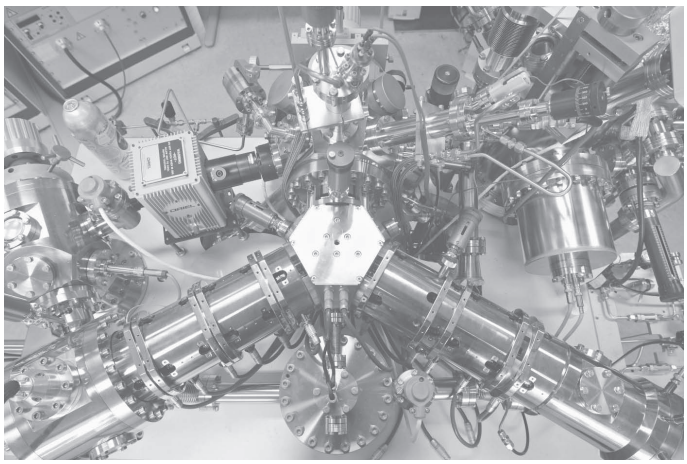

2.1 Low Energy Electron Microscopy

In surface science, visualization and characterizion of the structure and dynamics at surfaces and thin films plays a fundamental role. To microscopically probe a surface one can use electron tunneling, scattering or diffraction. Based on diffraction, Low Energy Electron Microscopy (LEEM) is the imaging counterpart of Low Energy Electron Diffraction (LEED) [14–16]. The LEEM technique was invented by Bauer in 1962 but not fully developed until 1985 [14, 18]. It took another 10 years before LEEM was commercially available.

In LEEM, electrons emitted from the (e.g. LaB_6) electron-gun, see schematic in Fig. 2.1, are accelerated to 15-20 keV. They are then focused using a set of condenser optics and sent through a magnetic beam deflector that is typically 60°, as in Fig. 2.1, or 90°. The electrons than travel through a cathode objective lens to be decelerated to low energies of typically a few eV since the sample is at a high negative potential. A slight difference in the sample and gun potential, corrected for work functions tunes the near-surface sampling depth of the low-energy electrons. The wavelength of these electrons is of the order of the interatomic distance. The elastically backscattered electrons then reaccelerate to the microscope potential and pass through the magnetic beam deflector again into the projector lenses. Imaging of the backfocal plane of the objective lens into the object plane of the projector lens, using an intermediate lens, creates a LEED pattern. By inserting the illumination aperture, see Fig. 2.1, into the Gaussian image plane of the objective one can select a spot on the surface down to a diameter of 1.4 μm. By inserting the contrast aperture in the field lens one can improve the real space image resolution. The acceptance cone of the imaging beam is selected, therefore the reflected electrons are limited by their parallel momentum. The image is focused on the Micro-Channel Plates (MCPs) using projector lense P2.

In LEEM the surface, or a part of it selected by the illumination aperture, is illuminated simultaneously. LEEM is therefore a direct imaging technique, in contrast to Scanning Electron Microscopy (SEM) and Scanning Tunneling Microscopy (STM). Due to its real-time imaging it is an excellent instrument to visualize and characterize processes like thin film growth, etching, strain relief, sublimation, phase transitions and adsorption in situ.

2.2 Imaging techniques

2.2.1 (μ) Low Energy Electron Diffraction

LEED is a technique to determine the surface structure of crystalline materials by bombardment with electrons. The obtained diffraction pattern can be used both qualitatively where the spot positions in the pattern give information on the symmetry of the surface structure, revealing its size and rotational align-

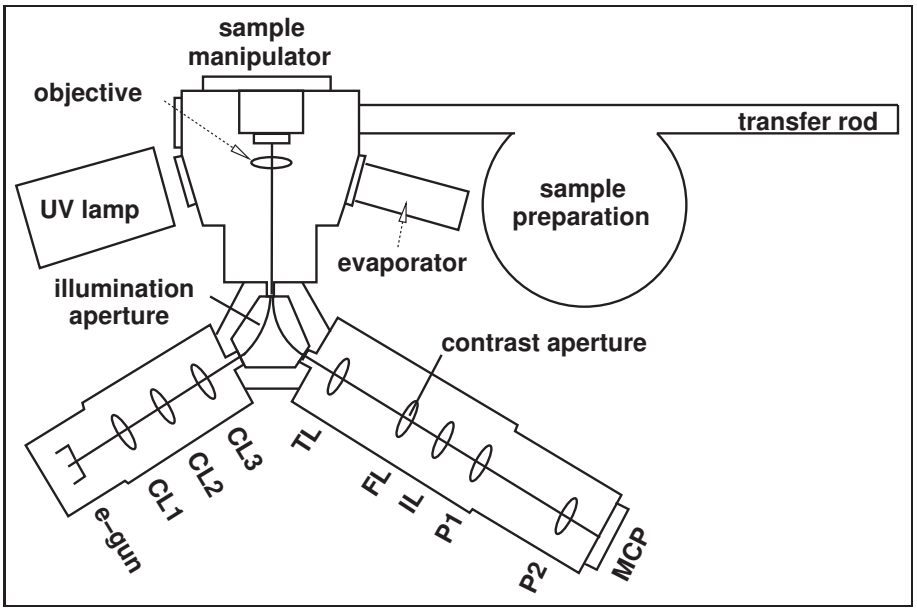

FIG. 2.1: A schematic representation of the optics in a LEEM. The electrons created by the electron gun (e-gun) are made into a parallel beam using condenser lenses 1 (CL1), 2 (CL2), 3 (CL3) and the objective onto the sample. The sample is at a high negative potential, therefore the electrons are slowed down between the objective lens and sample. The backscattered electrons are then reaccelerated. The diffraction pattern, or real space image by insertion of the contrast aperture, generated in this way can be projected onto the Micro-Channel Plates (MCPs) using the transfer lens (TL), field lens (FL), intermediate lens (IL), P1 and P2 lens. The illumination aperture allows control of the area of the sample that is illuminated up to 1.4 μm.

ment with respect to the substrate, and quantitatively where the spot intensities as a function of incident electron energy (I/V-curves) reveal information on the atomic species and positions on the surface compared to calculations [1]. The diffraction pattern is formed in the back focal plane of the objective lens and projected onto the projective lens (P1) using the intermediate lens (IL). An example of a LEED pattern can be found in Fig. 2.2(a) for a carbon covered Ni(111) surface generating a moiré pattern. By insertion of the illumination aperture into the image plane of the objective we can select a spot on the surface down to a diameter of 1.4 μm to image its diffraction pattern, see also Fig. 2.1. This is a very useful technique since one can deconvolute a diffraction pattern containing information of a large part of the sample simply by choosing a selected area and

[1] In LEEM the incident beam is perpendicular to the surface. Since the I/V-LEED curves depend on incoming angle (see e.g. [19]), no corrections for this for comparison to computational obtained LEED calculations need to be done.

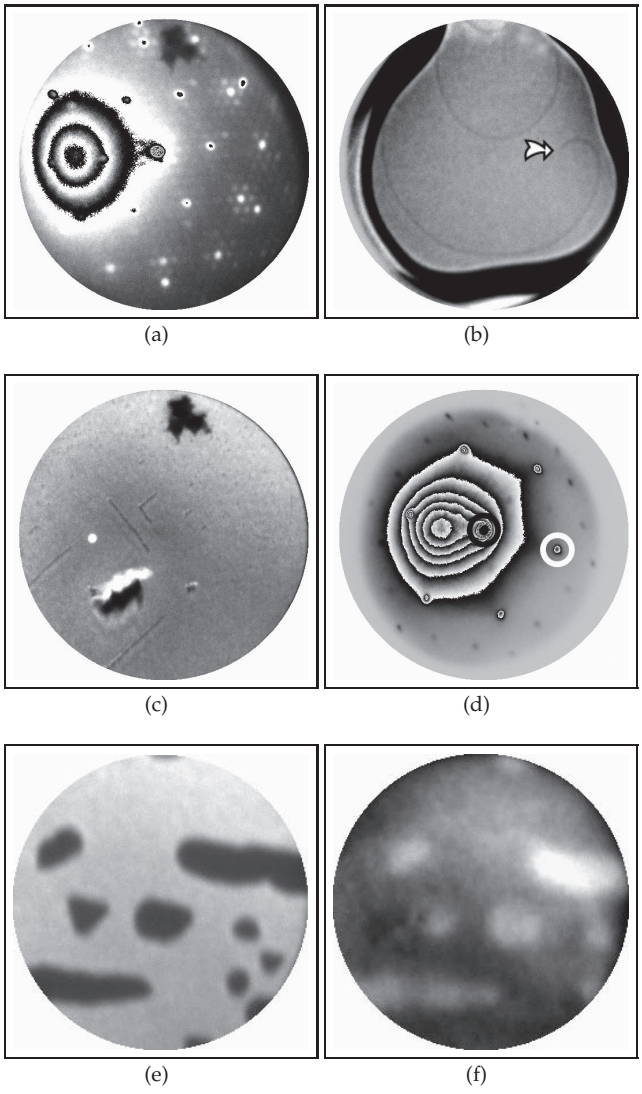

FIG. 2.2: (a) LEED pattern recorded at RT of C covered Ni(111). Electron energy 63.0 eV. (b) Atomic steps on Ni(111). The arrow indicates a screw dislocation. At the sample temperature of 1150 K steps are retracting, spiraling over the screw dislocation. FoV 10 μm, electron energy 1.6 eV. (c) Photo-Emission Electron Microscopy (PEEM) image, FoV=100 μm, recorded for Cu covered W(100) at 675 K. The bright circle is illuminated with electrons through the smallest illumination aperture of 1.4 μm. (d) LEED pattern of Pb covered Ni(111) at 474 K, electron energy of 40.0 eV, where bright field imaging selecting the intensity indicated by the black circle results in Fig. 2.2(e) and dark field imaging selecting the intensity indicated by the white circle results in Fig. 2.2(f). For both images FoV=4.8μm, electron energy 20.0 eV.

retrieve its diffraction pattern.

2.2.2 Phase contrast

Phase or interference contrast makes use of the interference of the diffracted waves in vertical direction which are reflected from terraces on opposite sides of a step. Using the specularly reflected electrons, known as bright field imaging, contrast is generated at steps in this way. By (de)focussing the imaged steps in LEEM, we are able to identify the step sense [20]. Figure 2.2(b) shows an example of atomic steps imaged by phase contrast.

2.2.3 Bright-field and dark-field contrast

Different reflectivity of different surface structures at a selected electron energy gives rise to contrast as well. This contrast mechanism is called bright-field contrast and is used in bright-field imaging. The reflected intensity as a function of electron energy (I/V-curves) can be used as a fingerprint for different surface structures. Contrast obtained by selecting a non-specular diffraction beam using the contrast aperture is called dark-field contrast and allows in dark-field imaging. By using this aperture, we are able to analyse the origin of a particular diffraction spot in real space. Figure 2.2(d) shows a μLEED pattern where the bright field imaging shows islands, see Fig. 2.2(e). The diffraction spot indicated by the white circle can be assigned to these islands by dark field imaging, shown in Fig. 2.2(f), in which the bright intensity corresponds to the positions of the islands compared to bright field imaging in Fig. 2.2(e).

2.2.4 Photo-Emission Electron Microscopy

By using a UV lamp illuminating the sample, photoelectrons are emitted when the photon energy exceeds the threshold for photoemission. In that case photoelectrons are emitted from the surface and imaged. Contrast will depend on the workfunction of the material and the illumination wavelength used. In our experimental setup a Hg discharge lamp was used giving a photon energy of 4.9 eV. In Fig. 2.2(c) an example of a Photo-Emission Electron Microscopy (PEEM) image is shown that is illuminated by electrons as well, shown as a small bright spot, limited by the smallest illumination aperture. Since its introduction in the 1930s, the technique has vastly improved. Synchrotron radiation nowadays provides PEEM with tunable, linear polarized, left and right circularized radiation in the soft X-ray range. It can give topographical, elemental, chemical and magnetic contrast of surfaces [21, 22].

2.2.5 Mirror Electron Microscopy

In Mirror Electron Microscopy (MEM) the electrons are only allowed to interact with the near-surface region on the sample by applying a sample bias so that the electrons are reflected just before reaching the sample. It is very complex to understand where the contrast mechanism exactly comes from. Height variations as well as local workfunction differences change the properties of the retarding field, thereby changing the reflected electron beam. The reflected intensity is high since no diffraction events took place.

2.3 Instrumentation

For the experimental work described in this thesis a Spin-Polarized LEEM (SP-LEEM) was used, manufactured by Elmitec GmbH as shown in Fig. 2.3. This instrument is capable of LEEM, PEEM, and magnetic sample imaging: SP-LEEM. Connected to the LEEM instrument is a homebuilt preparation chamber, shown in Fig. 2.1, where we are able to sputter and flash the sample, use Auger Electron Spectroscopy (AES) to measure sample composition and perform elemental analysis as well as a residual gas analyzer to monitor the quality of the vacuum. The base pressure in the LEEM chamber is 1×10^{-10} mbar, where for the preparation chamber it is 5×10^{-10} mbar.

2.4 Sample Preparation

2.4.1 Ni(111)

A Ni(111) sample, 10 mm in diameter and 1.5 mm thick was purchased from the Surface Preparation Laboratory. Prior to insertion in UHV the sample was annealed for 48 hours to a temperature of 1450 K in an Ar/H_2-atmosphere to remove bulk sulfur. For crystal cleaning three basic methods are used: (i) chemical cleaning, (ii) sputtering and (iii) cleaving in vacuum. Method (i) and (ii) are generally followed by vacuum annealing to restore an ordered, clean surface. For the preparation of the Ni(111) sample, methods (i) and (ii) are used. A "cook book" method for the cleaning of Ni crystals can be found in Ref. [23]. Typical bulk impurities of Ni surfaces are C, S, Cl, N and O. In particular C and S turn out to be persistent contaminations that segregate to the surface when the crystal is heated. Ref. [23] claims that by exposing the crystal to gas phase H_2, the S segregation is enhanced by a factor of $\sim$25 as compared to segregation in vacuum. A H_2 treatment is therefore the first step in the sample preparation process. When we bring the sample in the vacuum setup we use AES to identify the remaining contaminations, see Fig. 2.4. The contaminations in the AES spectrum of Ni(111) consist mainly of one peak at 276 eV which is attributed to C. At temperatures $>$800 K the C peak is somewhat reduced. Upon cooling down

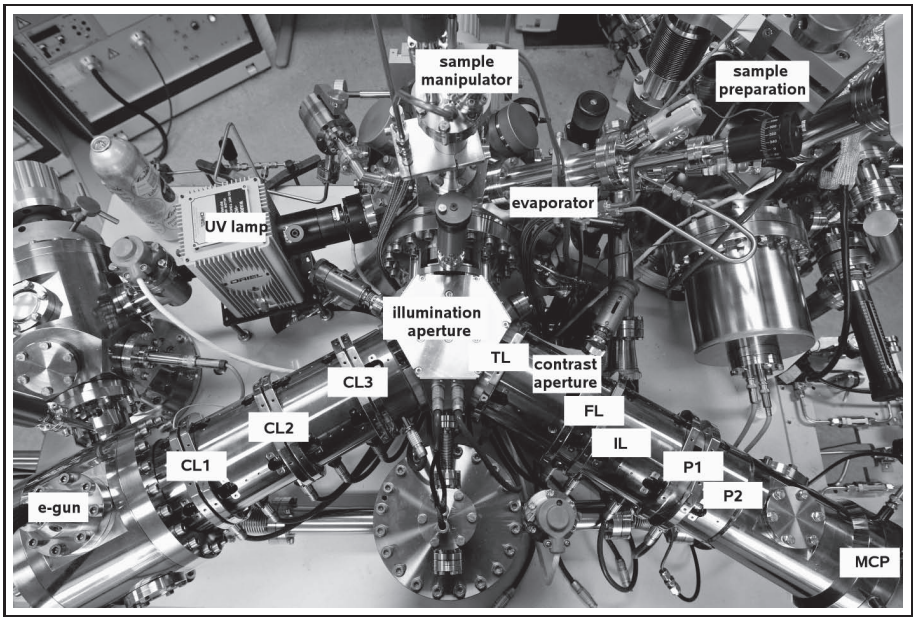

FIG. 2.3: The SP-LEEM in the lab of the Physics of Interfaces and Nanomaterials group at the University of Twente. All labels in the image correspond to the schematic representation in Fig. 2.1.

to RT the C diffuses back to the surface. An attempt to effectively remove the C by sputtering using e.g. 250-1000 eV Ar^+ bombardment, will fail because of the very low sputtering yield of carbon being $\sim$0.1 atom per incoming Ar ion. To reduce the C contamination on the Ni(111) surface, a reaction with O_2 at a temperature of about 1200 K and pressures as high as 10^{-8} mbar were used for short times. The removal of the C can be monitored by following the change in the gas phase partial pressure of CO. Until the concentration of bulk C is seriously depleted, the surface C concentration and therefore, the evolution of CO will remain constant. Ref. [23] proposes a possible reaction mechanism. By this heat treatment a small O peak shown in AES at 516 eV has grown. At temperatures above 1000 K the O disappears due to diffusion into the bulk. After this 1000 K anneal, S (150 eV), N (378 eV) and Cl (171 eV) peaks are clearly visible. One possible way to remove these impurities is sputtering at RT. Sputtering at higher temperatures fails to remove the S to any degree. Presumably, the rate of diffusion of S to the surface at higher temperatures is greater than, or at least equal to, the rate of removal by sputtering. Oxidation of the surface does not seem to be a problem for Ni(111). By applying a few sputtering cycles, the O peak (516 eV) is removed. These short anneals do result however in a small increase of S and Cl. The final step in sample treatment consisted of cycles of 1 keV Ar^+ bombard-

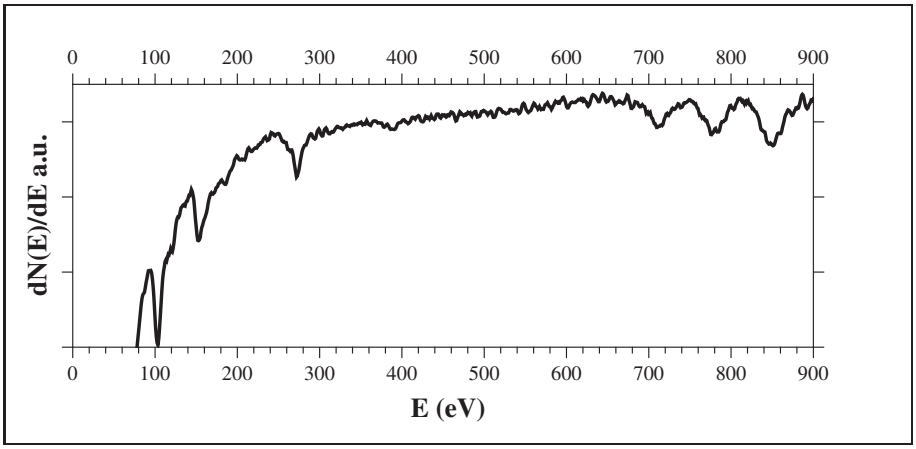

FIG. 2.4: An AES spectrum of Ni(111) after a few cleaning cycles. The main contaminants C (272 eV) and S (152 eV) are present at the surface. The peaks at 102, 716, 782 and 848 eV correspond to Ni.

ment at RT at an ion-current density of $\sim$1.6 μA/cm^2 for 30 minutes under an angle of 45° and subsequent flash-annealing to a temperature of about 1150 K. The sample temperature was calibrated using the rectraction of steps over time at a temperature where sublimation is expected as described in reference [24]. For more details see Appendix A.

2.4.2 W(100)

The tungsten sample was also purchased from the Surface Preparation Laboratory and was 10 mm in diameter but only 0.5 mm thick. Typical contaminants are carbon and oxygen, in which case the LEED pattern shows either a c(2×2) or a $(n \times 1)$ structure, where $n = 5$ is the most typical one [25]. We also found (6×1) and (4×1) structures. Annealing a W crystal usually leads to a segregation of C, which is most prominent at temperatures around 1300 K and can easily be monitored using LEED. By annealing in O_2, the segregated C can react with O_2 to form volatile CO. Annealing at higher temperatures for a longer time, however, causes a lot of heat dissipation into the UHV parts and causes a bad vacuum. Besides that, a layer of tungsten oxides is formed which can be removed by flashing to temperatures over 2200 K [26]. In order to avoid the heat dissipation causing a bad vacuum we used the cleaning procedure as described in Ref. [27] in the sample preparation chamber, see also Fig. 2.1. The procedure consists of two-step-flashing. We start by cycles of low power flashes to a temperature of around 1200 K using a O_2 background pressure of 3×10^{-8} mbar. Every cycle consists of dosing to about 1.5 L followed by a flash with a power of about 130 W. This procedure is monitored using Thermal Desorption Spectroscopy (TDS) measuring

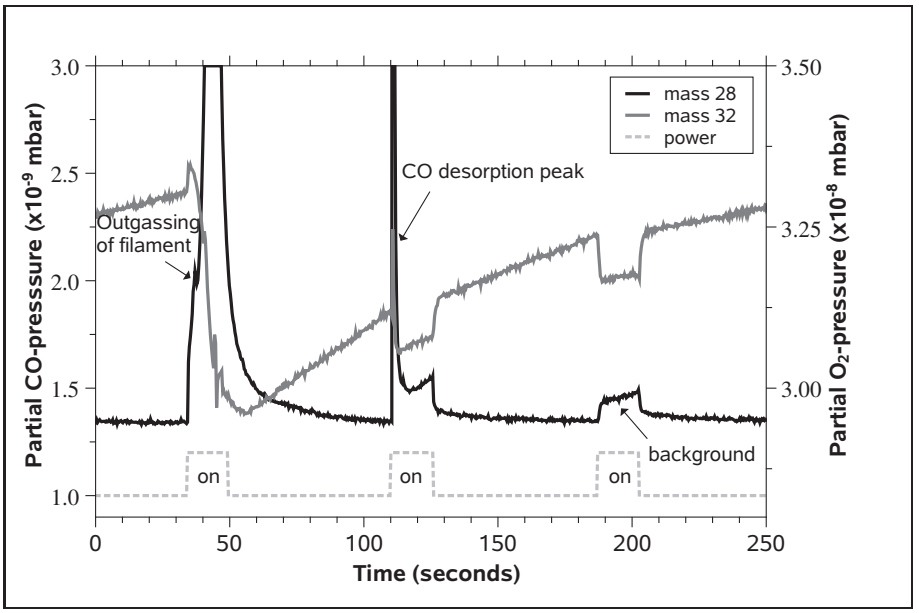

FIG. 2.5: Thermal desorption spectra during three subsequent low power flashes of W(100) that has been prepared several times. Initially the crystal contains a submonolayer surface coverage of C. Both the CO and O_2 pressures are monitored. The first peak shows outgassing of the filament and CO desorption. The second peak shows only CO desorption whereas the third low power flash only shows a background pressure due to heating.

the partial pressure of both CO and O_2. The procedure using low power flashes stops when the CO desorption peak has almost vanished, see Fig. 2.5. After that we moved the sample to the LEEM chamber where a (few) high power flash(es) with a power of 175 W followed to desorb the tungsten oxides at a temperature of about 2000 K. This procedure may be followed by sputtering cycles as described for Ni(111) followed by a high power flash.

2.5 Sublimation source

For the deposition of Pb and Cu we used a homebuilt Knudsen cell. To deposit Pb, only radiative heating was used whereas for Cu this was combined with electron bombardment to achieve a temperature of the Knudsen cell above the melting temperature of the material contained. An inner, electrically isolated shield functions as a Wehnelt cylinder. An outer shield is in direct contact with the base of the source and is cooled by a water flow. Using a manual shutter we are able to control the flux.

For the deposition of Bi we made use of a commercially available Knudsen cell that is heated by radiative heating. The flux can be stopped by a manual shutter.

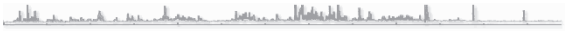

Quantum Size Effect driven structure modifications of Bi-films on Ni(111)

3

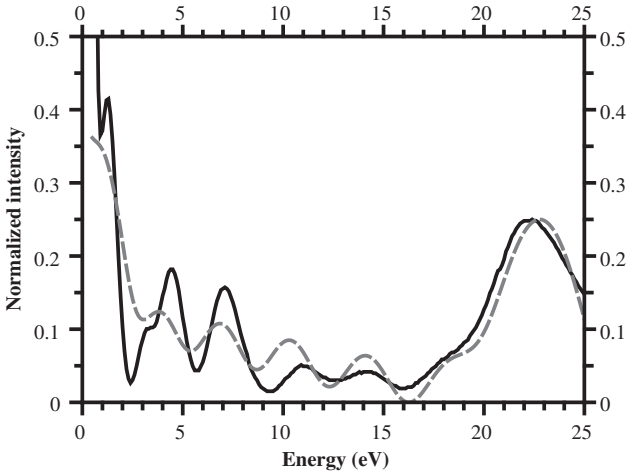

The Quantum Size Effect (QSE) driven growth of Bi film structures on Ni(111) was studied in situ using Low Energy Electron Microscopy (LEEM) and selective area Low Energy Electron Diffraction (μLEED). Domains with a (3×3), $\left[\begin{smallmatrix} 3 & -1 \\ 1 & 2 \end{smallmatrix}\right]$, and (7×7) film structure are found with a height of 3, 5, and 7 atomic layers respectively. Comparison of I/V-μLEED curves with Tensor LEED calculations shows perfectly accommodated Fermi wavelengths, indicative that not only the quantized height, but also the film structure is driven by QSEs.

3.1 Introduction

The structure and morphology of thin metal films can alter the physical properties of a material so that they become different from those of the bulk material. This can be a result of e.g. film structure and/or the usually disregarded QSE. For thin Bi (a prototype group V semimetal) films these effects can play a dominant role in determing the film structure, since its electronic properties are a result of the tiny overlap between the valence and conduction bands. The films therefore balance between being a metal or semiconductor [28]. A rather unusual growth mode that has a profound influence on thin film morphology, can occur due to the QSE and is referred to as quantum or electronic growth. QSEs give rise to specific preferred film heights as the result of a characteristic relationship between the Fermi wavelength and the interlayer spacing [29–31]. Thin Pb(111) films are the main representative of this class of materials since their bilayer increment almost perfectly accommodates 3/2 Fermi wavelengths, resulting in a quasi bi-layer oscillation of the thin film stability and its physical properties [32]. Bulk Bi is very similar to Pb since the Fermi energy calculated from a free electron model of bulk Bi is only 0.43 eV higher [33]. The slight structure distortion along the trigonal axis of bulk Bi is however known to cause the band structure to become semimetallic. This results in exotic properties such as long(er) Fermi wavelengths [34]. Besides that, Bi is also a soft semimetal, making electronic effects more pronounced than strain effects. This property makes thin Bi films prime candidates for allotropism. For Bi on Ni(111), a (7×7) and $(\sqrt{7/4} \times \sqrt{7/4})$-R19° overlayer structure was found in literature [35]. From a straight forward textbook free electron calculation, the (7×7) overlayer structure should be able to accommodate 3/2 Fermi wavelength (within 10%) in a bilayer increment as well. Deposition on a suitable substrate therefore makes Bi a candidate for electronic growth, as we will show in this Chapter.

Here, we present a study that investigates the growth of thin Bi domains on Ni(111) at temperatures ranging from 423 K up to 474 K. Using in situ LEEM and μLEED we are able to probe the properties and ordering of different Bi film structures. Our observations show that the structure of the domains that grow is driven by the QSE that results from the accommodation of $n/2$ Fermi wavelengths.

3.2 Experimental

The experiments were performed in an Elmitec LEEM III instrument. A Ni(111) surface was cleaned by cycles of 1 keV Ar^+ bombardment at RT, followed by flash annealing to a temperature of 1150 K. The cleanliness of the sample was monitored using Auger Electron Spectroscopy (AES) and LEEM. LEEM images revealed terraces with a width of $\sim$1 μm. All sample temperatures are subject to a measurement uncertainty of 5% and were calibrated using the uphill motion of

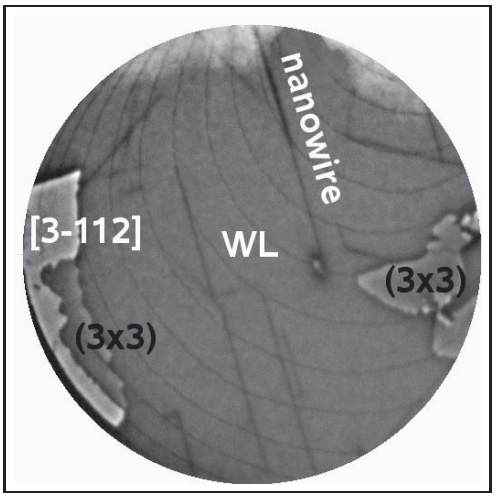

FIG. 3.1: LEEM image of a (3×3) domain and a [3-112] domain, both surrounded by the (7×7) wetting layer. FoV=10 μm, electron energy 2.0 eV, 474 K, $\theta_{Bi/Ni} = 0.66$ ML.

steps over time at a temperature where sublimation is expected, as described in Ref. [24]. Bismuth was deposited from a Knudsen cell.

3.3 Results and discussion

To determine the properties of the first Bi layer on top of the Ni(111) surface we performed μLEED illuminating a circular area of 1.4 μm in diameter during growth at 474 K. A $(\sqrt{3} \times \sqrt{3})$-R30° surface alloy shows its maximum peak intensity at a coverage of 0.33 ML, where 1 ML corresponds to 1 Bi atom per Ni surface atom, in agreement with literature [35–38]. Dealloying then leads to the creation of a wetting layer and peaks associated with an incommensurate Bi overlayer appear in the μLEED moiré pattern at a coverage of 0.45 ML. These Bi peaks shift outwards with increasing coverage, indicating a continuous in-plane compression of the lattice constant, yielding an incommensurate Bi film until a stable commensurate (7×7) surface structure locks in. The latter forms when the lattice constant (3.50 Å) stabilizes and was used for an exact in situ calibration of the deposition rate. The measured rate is identical to that obtained from the maximum peak intensity for the $(\sqrt{3} \times \sqrt{3})$-R30° surface alloy. The Bi (7×7) wetting layer structure, known from literature [35], has a unit cell of 25 atoms and is depicted in Fig. 3.5(d).

After completion of the wetting layer, Bi nanowires appear with an orientation that is three-fold symmetric, see Fig. 3.1. The details of these wires are discussed in Chapter 4. From a coverage of 0.51 ML onward two different domains

appear, as is illustrated by Fig. 3.1. μLEED reveals the domain structures to be (3×3) and $\left[\begin{smallmatrix} 3 & -1 \\ 1 & 2 \end{smallmatrix}\right]$. The LEED patterns and unit cells are shown in Figs. 3.5(b) & (c), and (e) & (f), respectively. The in-plane lattice constants of these film structures are 3.74 Å and 3.80 Å at single layer coverages of 0.444 ML and 0.429 ML. For convenience we will write the matrix as [3-112]. Both types of domains grow at an anomalously low rate, suggesting that the domains are substantially higher than one atomic layer. An estimate of the heights can be obtained by comparison to the Bi deposition rate. Describing the total coverage ($\theta_{Bi/Ni}$) as the sum of the fractional areas (ϕ_i) corresponding to the different film structures times their respective layer coverage (θ_i), one can calculate the average height of the domains using the relation:

$$\theta_{Bi/Ni} = \sum_i \phi_i \theta_i = \phi_{WL} \times 0.510 + \phi_{[3-112]} \times 0.429 \times n_{[3-112]} + \phi_{(3\times3)} \times 0.444 \times n_{(3\times3)}$$

where $n_{(3\times3)}$ and $n_{[3-112]}$ are the number of atomic layers of the two film structures. The (3×3) domains occur more abundantly than [3-112] domains and several measurements of the exclusive growth of (3×3) domains reveal an average height of 3.0 ± 0.1 atomic layers. In a similar manner an average height of 5.1 ± 0.2 atomic layers is found for the [3-112] domains. From conservation of the amount of deposited material, we can also derive that both the (3×3) and [3-112] film structures grow directly on the metallic Ni(111) substrate and are surrounded by the (7×7) wetting layer. This in contrast to the wetting layer of Bi on Si(111), where the semiconducting substrate is first passivated by the wetting layer before electronic growth starts [34, 39]. We emphasize that a careful inspection of the I/V-LEEM data on different (20×20) pixel sized spots across identical domains confirms a very high degree of uniformity and thus indicates constant height for a particular domain. This is further corroborated by the evolution of the various fractional coverages during deposition.

The evolution of the various domains has been evaluated in the coverage range $\theta_{Bi/Ni} = 0.5$-1.23 ML. In Fig. 3.2(a) we demonstrate that, next to the wetting layer, the [3-112] and the (3×3) domains coexist and do not grow sequentially. Initially, the fractional coverage of both domains is similar, but soon the (3×3) domains prevail. This suggests that the latter structure is more stable. This is confirmed by the occasional decay of the [3-112] domains in favor of the (3×3) domains during deposition at a constant temperature of 474 K.

By measuring the fractional areas, ϕ_i, of the domains i and accounting for their slightly different in-plane densities, θ_i, one can in fact determine the total coverage $\theta_{Bi/Ni}$, using the relation described above. The heights of the wetting layer, the (3×3) and the [3-112]-domains were determined previously at 1, 3 and 5 layers, respectively. The result is shown in Fig. 3.2(b). We observe a linear increase of the total coverage, as is expected for a constant deposition rate. From the slope we obtain a deposition rate of $1.04 \pm 0.04 \times 10^{-4}$ ML/s in close

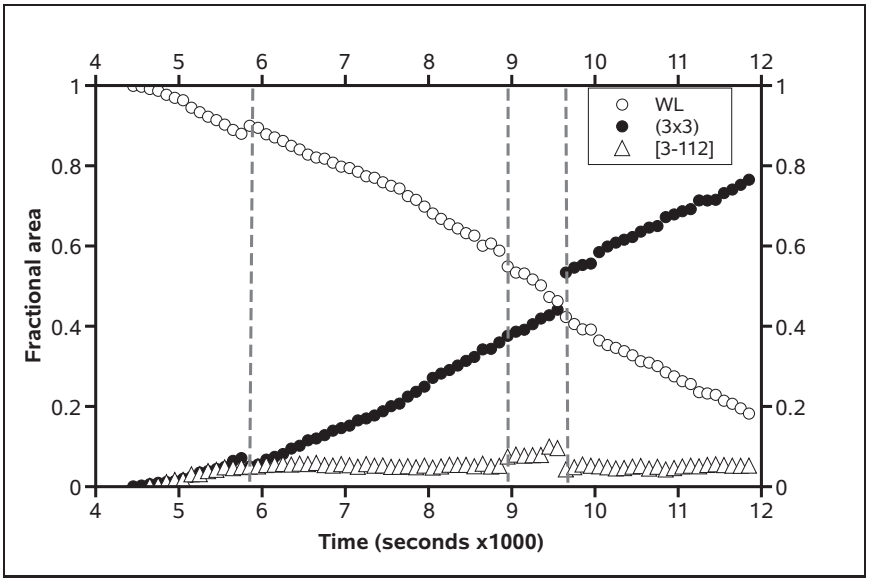

(a)

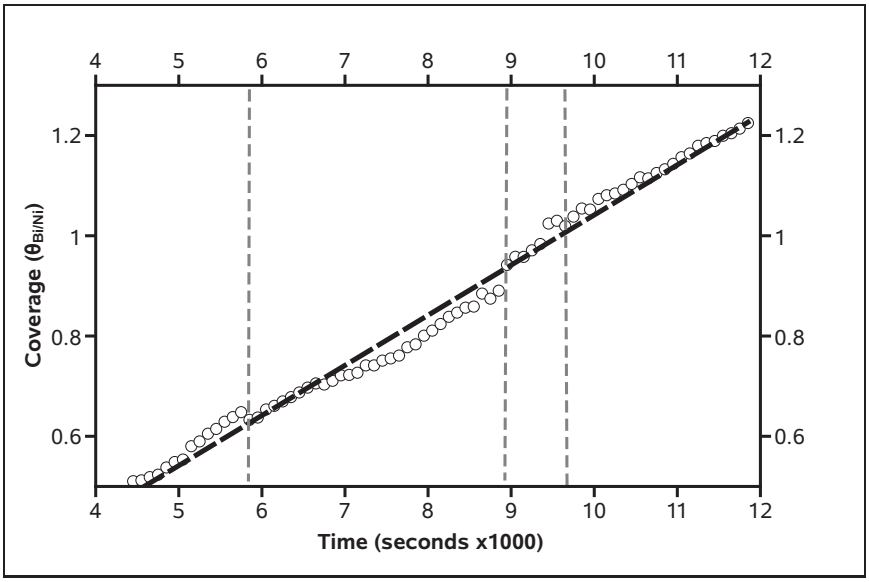

(b)

FIG. 3.2: (a) The evolution of the fractional area during deposition of Bi on Ni(111) at 474 K shown in Fig. 3.3. The wetting layer (WL) (○), (3×3) (●) and [3-112]-domains (△) are labeled. The dashed lines indicate readjustment of the instrument to correct slight drift during the experiment that lasted more than three hours. (b) The total coverage, calculated using the equation described in the text.

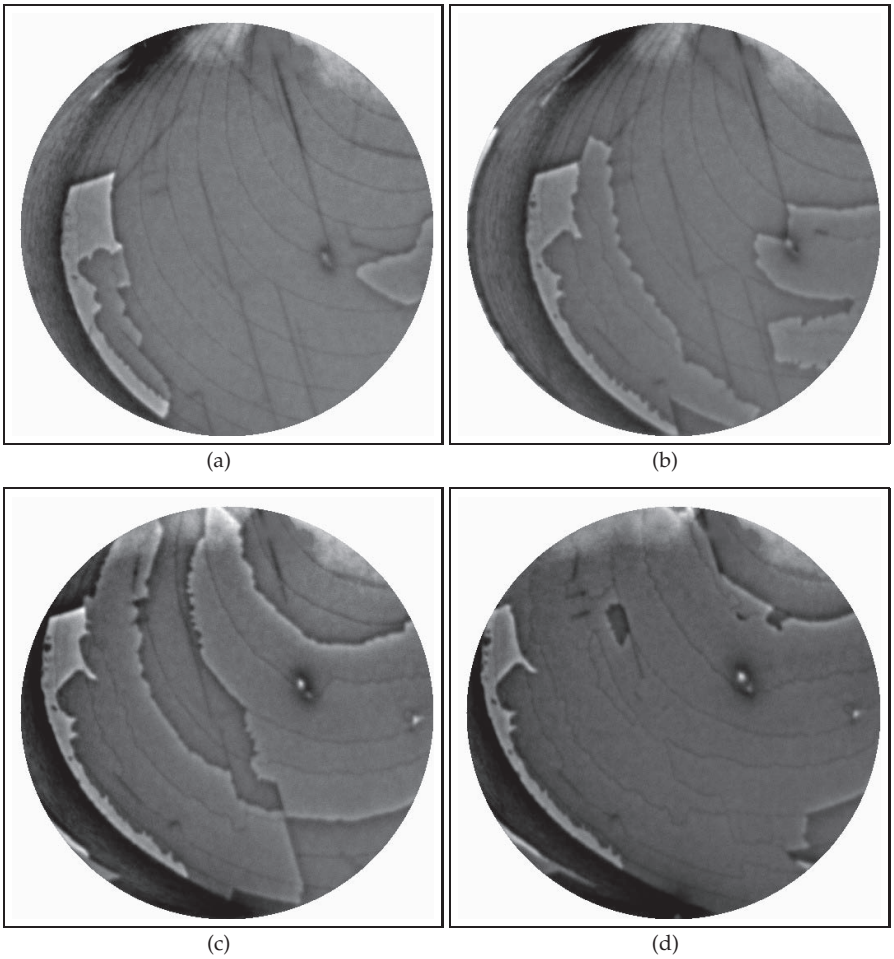

FIG. 3.3: Snapshots of the LEEM images acquired at 6000 (a), 8000 (b), 10000 (c) and 12000 (d) seconds; FoV=10μm and electron energy 2.0 eV. The different domains are shown as the dark (WL), the dark grey ((3×3)) and the lighter grey areas ([3-112]).

agreement with the values of 1.12×10^{-4} ML/s, determined from the maximum intensity of the diffraction peaks corresponding to the $(\sqrt{3} \times \sqrt{3})$-R30° BiNi surface alloy and 1.15×10^{-4} ML/s, extracted from the completion of the wetting layer. We consider this convincing agreement as strong evidence for our earlier assignments of the height and the density of the various domains. The slight deviations are attributed to the finite size of the already large Field of View (FoV) of 10 μm. Note that the choice of the FoV is subject to a compromise: a larger field of view would provide a better representation of the total coverage, but only at the cost of a less accurate determination of the various fractional coverages. This trade off is also responsible for the minor discontinuities of the curves in Fig. 3.2(a), less obvious, in the total coverage in Fig. 3.2(b). The discontinuities are caused by slight adjustments of the sample position to correct for thermal drift during the experiment, which lasted over three hours. We emphasize that already during the initial stages of growth, when Bi mesas form, about 50% of them assumes a height of 5 layers and the other half a height of 3 layers. We consider this as strong additional evidence for the importance of quantum size features in the Bi/Ni(111) system.

To confirm the origin of the anomalous growth, electron reflectivity curves were measured for both domains as a function of electron energy, see Fig. 3.4(a) and (b). Quantum size oscillations are observed for both domains. For the (3×3) domains two quantum interference peaks are found, whereas for the [3-112] we find four, confirming the previously measured heights. The structure and morphology of Bi films on Ni(111) therefore appears to be almost exclusively determined by QSE.

During experiments at a slightly lower temperature of 422 K a third film structure of type (7×7) was observed, which was found completely surrounded by (3×3) domains. A height of 7 layers was derived from the growth rate. All μLEED patterns and their corresponding real space unit cells are shown in Fig. 3.5.

To establish whether $n/2$ times the Fermi wavelength can be accommodated by the three film structures, the interlayer spacings have to be accurately measured. To achieve this, we compare the specular beam intensity to Tensor LEED calculations since this peak contains the required information (interlayer distance) most directly. It is in fact the only possible way to determine the interlayer spacing in our instrument. We also note that all μLEED patterns shown in Fig. 3.5(a-c) are six-fold symmetric. This indicates that the domains are in hexagonal AB stacking, as is also found for Bi on Si(111)-(7×7) [34]. In spite of the uncertainties caused by the limited reliability of the used electron-matter interaction potential at very low energies, good semi-quantitative information was obtained. I/V-μLEED curves were calculated using the Erlangen Tensor LEED package `TensErLEED` [40], where phase shifts were calculated using the `EEASiSSS` package [41]. We have restricted our analysis to the energy window 20-100 eV. The lower limit is determined by the complexity of the electron solid

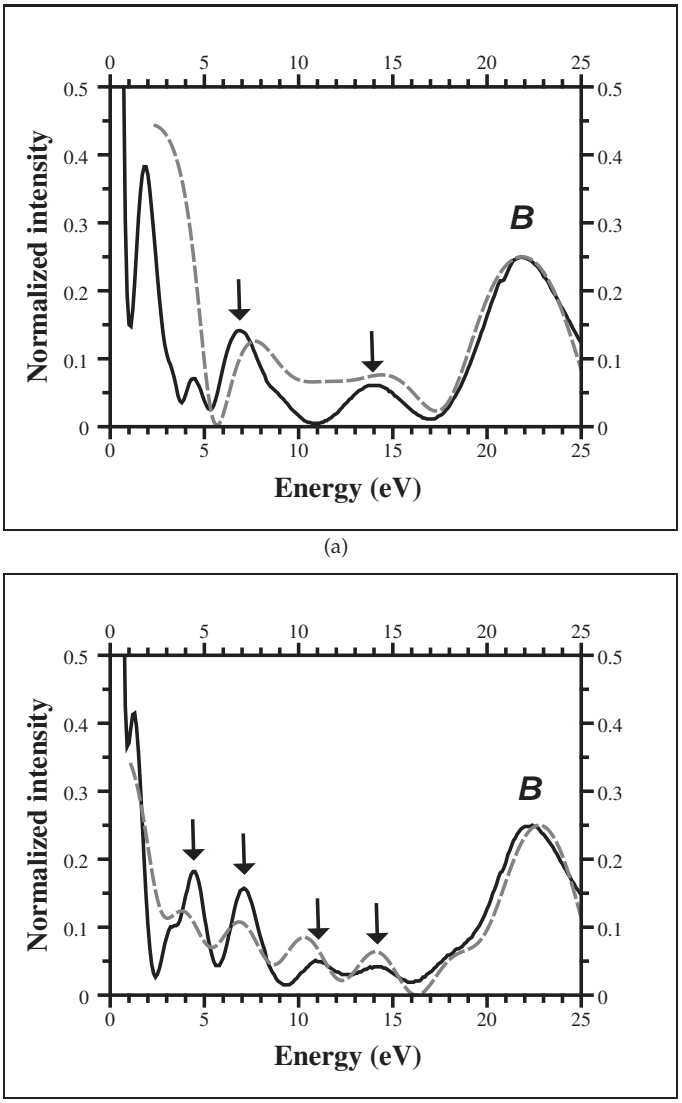

FIG. 3.4: Quantum interference peaks in I/V-LEEM measurements as indicated by the arrows: two for the three atomic layer high (3×3) (a) and four for the five atomic layer high [3-112] Bi films on Ni(111) (b). Experimental curves (black) and best fit (grey dashed) using the KP model. The Bragg peak at about 22 eV is indicated by *B*. For the used parameters see Table 3.1.

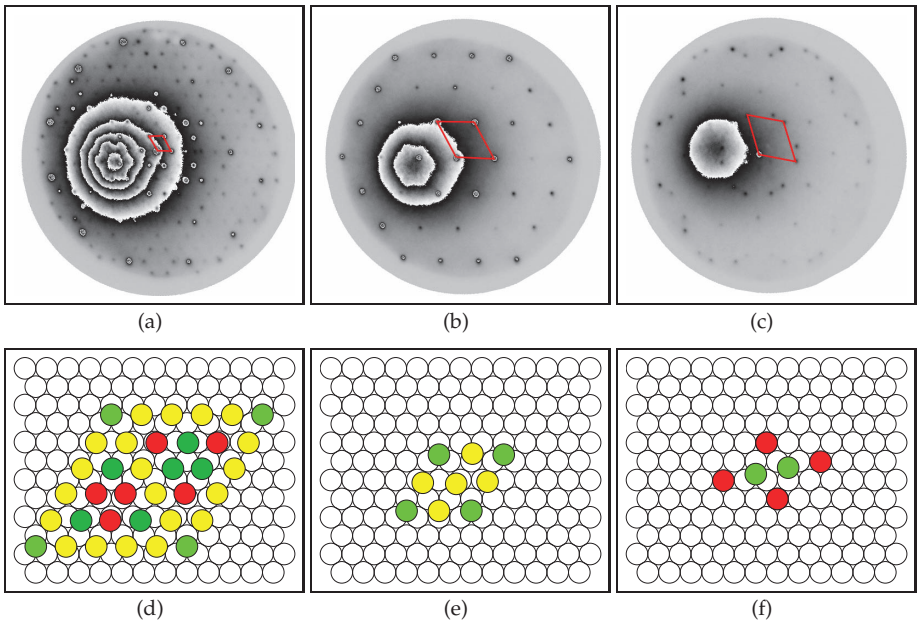

FIG. 3.5: μ-LEED images taken at 40.0 eV (a-c), and the corresponding real space unit cells (d-f) for the three different Bi film structures. Panels (a) and (d) show a (7×7) film structure with lattice constant 3.49 Å (θ =0.510 ML), measured at 422 K. (b) and (e) show a (3×3) overlayer with lattice constant 3.74 Å (θ =0.444 ML), and (c) and (f) show a [3-112] overlayer with a lattice constant 3.80 Å (θ =0.429 ML), both measured at 474 K. For the real space images (d-f) (darker) green corresponds to (close to) three-fold hollow, red to (near) on-top, yellow to intermediate positions, where in all cases only the contact layer with the Ni(111) surface is drawn.

interaction potential at low energies [42, 43]. The upper limit is determined by the S/N-ratio in our μLEED data. Despite the fact that the calculations were restricted to a simplified geometrical structure that does not take into account any relaxation and no fitting was performed, the Pendry R-factors quantifying the comparison are reasonable. A clear trend is found when comparing the experimental values with the calculated curves. This leads to a best fit for the interlayer distance of 3.21 Å for the (3×3) structure, 3.02 Å for the [3-112] structure and 2.90 Å for the (7×7) structure.

Using these calculated best-fit interlayer distances, a simple Kronig Penney (KP) model was used to model the QSE, see Ref. [20] for a full description. In short: The KP model uses two potential boxes for each layer, with depth V and width w, centered at the atoms (V_a,w_a) and in between the atoms (V_g,w_g). The substrate is given as a featureless box with depth V_{0s}. By requiring the wavefunctions and their first derivatives to match at the various transitions, including the

structure	V_a(eV)	V_g(eV)	V_{0s}(eV)	w_a(Å)	w_g(Å)
(3×3)	18.0	4.9	15.0	1.67	1.50
$[3 - 112]$	20.7	10.2	20.0	1.34	1.70

Table 3.1: Parameters as defined by Ref. [20] used for the KP model fits to the data points shown in Fig. 3.4. V_{0s} changes for the film structures since it represents the substrate to first layer potential.

structure	(3×3)	$[3 - 112]$	(7×7)
a_{nn}	3.74	3.80	3.49
h(#layers)	3	5	7
d_{TL}(Å)	3.21	3.02	2.90
ρ (atoms/nm^3)	25.79	26.48	32.69
$\#\lambda_F$	2.5	4.0	5.5
$\Delta a_{inter}/a_{inter}$	2.2%	1.7%	<1%

Table 3.2: Properties of the three different film structures found: in-plane lattice constant (a_{nn}), interlayer distance derived from Tensor LEED calculation (d_{TL}), density (ρ), fitted number of Fermi wavelengths ($\#\lambda_F$), and calculated deviation from interlayer distance as compared to Tensor LEED calculation ($\Delta a_{inter}/a_{inter}$). The (7×7) structure was measured at 422 K.

vacuum-film interface, we can derive the reflection coefficient at the latter interface, which represents the measured quantity. The result is $N - 1$ interference peaks for a N layer thick film.

A good fit, see grey curves in Fig. 3.4, is obtained using the parameters given in Table 3.1. In both curves the peaks at around 1.8 and 4.4 eV for (3×3) and 1.3 and 3.5 eV for [3-112] are likely a result of the band structure of Bi on Ni(111). For the thicker (7×7) structure the band structure and Bragg peak dominate the I/V-LEEM curve.

Using the best fit interlayer distances from Tensor LEED calculations, we can now find the number of Fermi wavelengths that all three different film structures accommodate. The height of the (3×3), [3-112] and (7×7) domains perfectly accommodate 2.5, 4.0 and 5.5 Fermi wavelengths (see Table 3.2), as calculated using the free electron model taking into account the different electron densities. The interlayer distances from Tensor LEED calculations deviate less than 2.5% from the interlayer distance calculated from the free electron model, see row $\Delta a_{inter}/a_{inter}$ in Table 3.2. The small mismatch between a perfect $n/2$ times the Fermi wavelength and the height calculations from experiment are perfectly within the error bar of the comparison between Tensor LEED calculations and the measured I/V-μLEED curves. For the higher film structures the error is reduced even further, well below 1%. The relaxation d_{12} found for the first layer spacing in QSE stabilized Pb-films [8] is of the order of a few percent, larger than expected for fcc(111) surfaces. Although the d_{12} relaxation plays a lesser role be-

cause of the larger mean free path at low energies, it may still contribute to the observed differences. We also note that a mismatch this small could in principle also originate from small phase shifts or other mechanisms that energetically stabilize certain film structures. The different film structures could give rise to small phase shifts, as has been observed experimentally [34]. From these results we can conclude that the free electron model can be used as a valid description for this system. The structural distortion along the trigonal axis is reduced for these three film structures in comparison to bulk Bi. This will result in changes in the band structure as mentioned before. The energetic preference to accommodate the Fermi wavelength in the (7×7) film structure is in fact so strong, that the density becomes even higher than what is known for bulk Bi [33], see also row labelled density in Table 3.2. The growth of thin Bi films on Ni(111), the quantized heights and film structures, can therefore be identified as almost exclusively determined by the QSE.

3.4 Summary

In summary, we have presented LEEM and μLEED measurements illustrating in situ the QSE driven growth of thin Bi film structures on Ni(111). The measured I/V-LEEM curves show well-defined quantum-size oscillations, that are in agreement with the results of a simple KP model. Three different film structures ((3×3), [3-112] and (7×7)) grow at specific heights of 3, 5 and 7 atomic layers. Comparing Tensor LEED calculations to I/V-μLEED curves we are able to calculate the height of these film structures, which perfectly accommodate $n/2$ times the Fermi wavelength and thereby illustrate the relevance of the QSE for quantization of island heights and ultimate film structure.

The influence of BiNi surface (de)alloying on meandering substrate steps

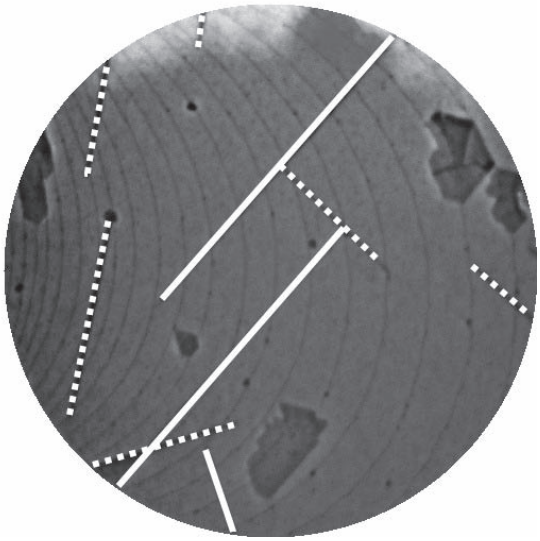

4

Using Low Energy Electron Microscopy (LEEM) and selective area Low Energy Electron Diffraction (μLEED) we have characterized both the (7×7) wetting layer and the $BiNi_9$ $\left[\begin{smallmatrix} 2 & 0 \\ -2 & 5 \end{smallmatrix}\right]$ nanowires that form during the growth of Bi on Ni(111). The 60 ± 20 nm wide nanowires have lengths up to 10 μm and a height of 4-6 atomic layers. After the formation of the wetting layer and nanowires, Quantum Size Effect (QSE) driven growth ensues, accompanied by the gradual disappearance of the nanowires and resulting meandering of the substrate steps. The displacements of substrate steps, directly imaged with LEEM, can be traced back to dealloying.

4.1 Introduction

To gain control over the self-assembly of nanostructures, the growth of nanowires is an important topic to understand in materials science [44, 45]. It is generally assumed that nanowires grow due to the competition between strain and surface energies, favoring one-dimensional structures above a certain size [46, 47]. The growth of Ag wires on Si(001) is e.g. explained by the 6% misfit strain between wire and substrate [48]. The downsizing of physical structures to small length scales can result in metal films and wires that show even more complex and different physical properties than those found for the bulk materials. For example, both strain-stabilized and electronically-stabilized structures have been widely reported on in literature [49]. A typical example of the former is the formation of a striped phase of Pb on Cu(111) as a result of a competition between the tensile and compressive strain of a PbCu surface alloy and a Pb overlayer phase [2, 50].

The formation of self-assembled nanostructures through a stabilizing interaction can be further complicated by surface alloying. Group V elements are particularly prone to this as they are known to exhibit allotropic transformations, as well as alloying on other metal substrates. Bismuth, a prototype group V element known for its allotropism, forms strained metastable thin films that exhibit phase transformations above a critical film thickness [51, 52]. For Bi on Ni the bulk alloy phase diagram reports the stoichiometric alloys BiNi and Bi_3Ni that are thermodynamically stable [53–55]. Therefore, alloying induced strain may be expected to play an important role in the growth of Bi on Ni(111). From several studies an initial $(\sqrt{3} \times \sqrt{3})$-R30° surface alloy was reported [35–38]. For higher coverages (7×7) and $(\sqrt{7/4} \times \sqrt{7/4})$-R19° overlayer structures were found [35]. The growth of one-dimensional nanostructures of Bi on Ni(111) has however not been reported in literature so far. We have previously shown Bi on Ni(111) to exhibit QSE driven growth and allotropism in Chapter 3.

In this Chapter, we present a study using in situ LEEM and μLEED to probe the properties and ordering of different Bi and Bi_xNi_y film and nanowire structures. Our observations show the alloying and partial dealloying of a $(\sqrt{3} \times \sqrt{3})$-R30° phase, eventually leading to a (7×7) wetting layer and stable $\left[\begin{smallmatrix} 2 & 0 \\ -2 & 5 \end{smallmatrix}\right]$ $BiNi_9$ nanowires, as well as nanowires with a proposed $\left[\begin{smallmatrix} 2 & 0 \\ -3 & 4 \end{smallmatrix}\right]$ structure. The nanowires are 60 ± 20 nm wide, several microns in length and a few atomic layers in height. Dealloying of the wetting layer as well as the gradual disappearance of the nanowires triggered by the formation of QSE stabilized structures as a result of continued deposition, results in meandering of the substrate steps. These step displacements can be directly imaged with LEEM.

4.2 Experimental

The experiments were performed in an Elmitec LEEM III instrument. A Ni(111) surface was cleaned by cycles of 1 keV Ar^+ bombardment at RT, followed by flash annealing to a temperature of 1150 K. The cleanliness of the sample was monitored by Auger Electron Spectroscopy (AES) and LEEM. LEEM images revealed terraces with a width of $\sim$1 μm. All sample temperatures are subject to a measurement uncertainty of 5% and were calibrated using the uphill motion of steps over time at a temperature where sublimation is observed, as described in Ref. [24]. Bismuth was deposited from a Knudsen cell.

4.3 Results

To determine the properties of Bi on Ni(111) we performed μLEED, illuminating a circular area of 1.4 μm in diameter during deposition at 474 K. Initially, the number of secondary electrons increases when the deposition of Bi is started, indicative of the formation of an adatom gas. Subsequently, the number of secondary electrons decreases and a $(\sqrt{3} \times \sqrt{3})$-R30° surface alloy appears, in agreement with literature [35–38]. Its maximum peak intensity was used to perform an in situ calibration of the coverage $\theta_{Bi/Ni} = 0.33$ ML, where $\theta_{Bi/Ni} = 1$ ML corresponds to 1 Bi atom per Ni surface atom. Dealloying then leads to the creation of a wetting layer. Peaks associated with an incommensurate Bi-rich overlayer appear in the μLEED pattern at a coverage of 0.45 ML. These Bi peaks shift outwards with increasing coverage, indicating a continuous in-plane compression of the lattice constant. Eventually, a commensurate Bi-rich film forms with a stable (7×7) surface structure at a coverage of 0.510 ML, see Fig. 4.1. The commensurate (7×7) surface structure forms when the in-plane lattice constant stabilizes at 3.50 Å and provides another opportunity for an exact in situ calibration of the coverage. The measured deposition rate of 1×10^{-4} Bi atoms per unit cell (uc) per second (Bi/uc/s) is identical to that obtained from the maximum peak intensity for the $(\sqrt{3} \times \sqrt{3})$-R30° surface alloy.

Assuming that at $\theta_{Bi/Ni} = 0.45$ ML dealloying of the $(\sqrt{3} \times \sqrt{3})$-R30° phase is complete and only Bi is populating the outermost layer, continued deposition should lead to an in-plane lattice constant compression caused by a linear increase in atomic density. One would then expect the in-plane lattice constant to be $\propto 1/\sqrt{ct}$, where c is the deposition rate from the vapor phase and t time. In Fig. 4.1 the lattice constant versus coverage is plotted, which surprisingly shows an almost linear decay. The continuous dealloying of the $(\sqrt{3} \times \sqrt{3})$-R30° surface alloy causes the effective deposition rate to increase linearly with time up to the coverage corresponding to the commensurate (7×7) surface structure: $c(t) \propto t$. Whether or not the surface alloy is completely depleted can not be deduced from this. μLEED measurements do not show ordered surface alloys for

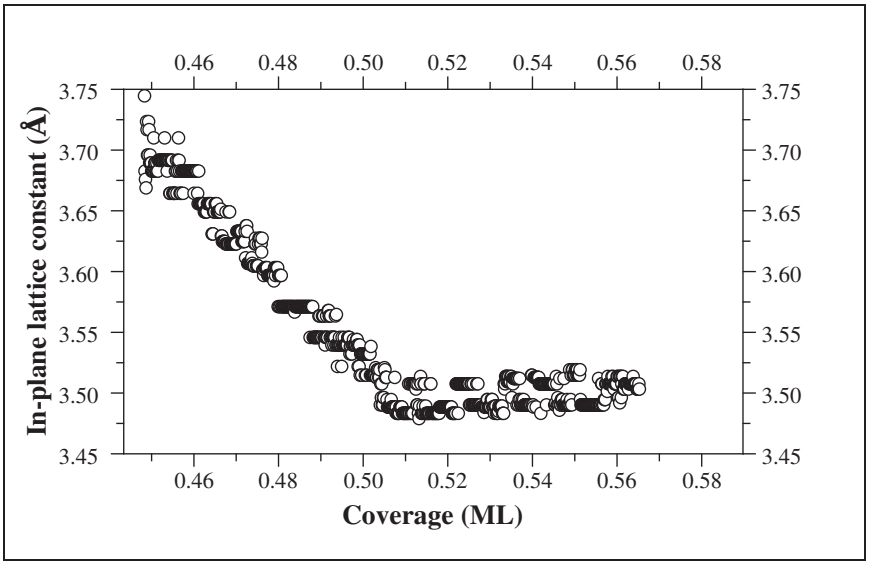

FIG. 4.1: The in-plane lattice constant, as derived from the position of the Bi(1,0)-peak as a function of coverage at 35.0 eV during Bi deposition at 474 K. The in-plane lattice constant of 3.50 Å corresponds to the completed (7×7) wetting layer with a coverage of 0.510 ML.

coverages $\theta_{Bi/Ni} > 0.51$ ML. The Bi (7×7) wetting layer structure, known from literature [35], is one atomic layer in height and covers 49 Ni unit cells which are filled by 25 Bi atoms, see also further below.

After completion of the wetting layer, Bi nanowires appear, as can been seen in Fig. 4.2(a). The nanowires grow in two sets of three-fold symmetric directions making an angle of 22°, shown in Fig. 4.2(b).The growth rate of all nanowires is similar and becomes smaller over time. The nanowires cross underlying Ni(111) steps without an appreciable reduction in growth rate. Nanowires with a length up to about 10 μm have been observed. A simple line-profile perpendicular to the nanowire gives a width of approximately 60 $\pm$ 20 nm, resulting in aspect ratios of the order of 100.

For structural characterization of the nanowires μLEED was used with a 1.4 μm aperture. Since the width of the nanowire is orders of magnitude smaller than the diameter of the aperture, the diffraction pattern is a superposition of two surface structures. Figure 4.3(a) shows a cumulative μLEED pattern, of the (7×7) wetting layer with a nanowire present. By summing the intensities over an energy range of 3.0 to 20.0 eV, all spots forming the superstructure become visible. Figure 4.3(b) shows a schematic diffraction pattern with in red the spots corresponding to the (7×7) wetting layer. Moving the aperture over a nanowire surrounded by wetting layer, we can identify the additional diffraction spots

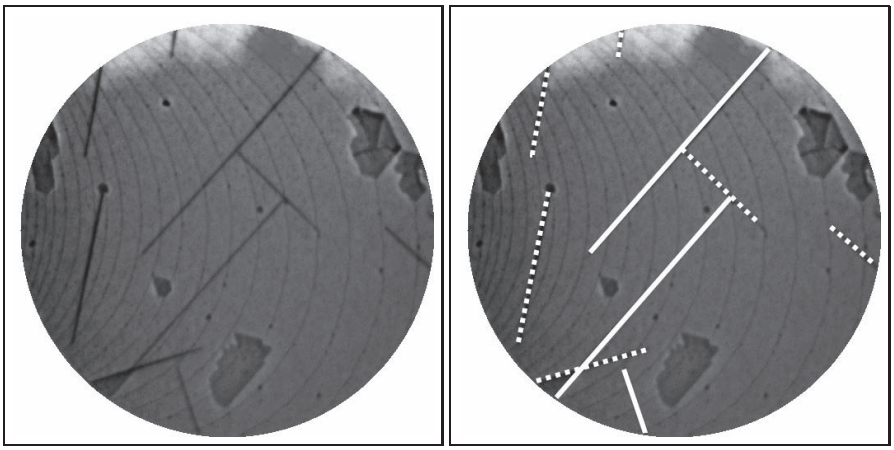

(a) (b)

FIG. 4.2: (a) LEEM image with nanowires and (b) the same with full and dashed lines drawn according to the two times three-fold symmetry. FoV=10 μm, electron energy 2.0 eV, T=474 K, $\theta_{Bi/Ni} = 0.57$ ML.

created by the nanowires, corresponding to the yellow spots in Fig. 4.3(b). The superstructure short axis is, along with the (7×7) wetting layer, aligned with respect to the $\langle 110 \rangle$-azimuth of the substrate. The superstructure has unit cell sides of 5.0 Å and 10.8 Å making an angle of 83°, corresponding to a $\begin{bmatrix} 2 & 0 \\ -2 & 5 \end{bmatrix}$ surface alloy as illustrated in Fig. 4.3(c). The unit cell contains 1 Bi atom and 9 Ni atoms in one plane and its short axis is aligned with the close packed direction of the Ni substrate. Additional information on the structure of the nanowires is obtained from a plot of the intensity of the (1,0) nanowire diffraction peak in Fig. 4.3(a) as a function of the electron energy, as is shown in Fig. 4.4. The intensity curve clearly shows interference features, related to the interlayer distance. From the energies corresponding to the maxima and minima we can derive the change of the normal component of the wave vector, Δk_z, for in-phase conditions, n, and out-of-phase conditions, $n + \frac{1}{2}$, respectively, where $n \in \mathbb{N}_0$. The result is plotted in Fig. 4.5 and shows an ideal linear relationship. From the slope of the straight line we obtain a vertical periodicity of 6.63 Å. This result is puzzling since we expected a value close to 2.03 Å, the Ni(111) interlayer spacing. This surprise actually presents an unexpected opportunity to gain further insight in the structure of the nanowires. The measured periodicity is obtained when we assume that the (2×1) Bi chains are along $[1\bar{1}0]$ and separated by 4 pure Ni chains, that are present throughout the nanowire, see also Fig. 4.3(c). In other words, in the fcc nanowire structure the (2×1)-BiNi $\langle 110 \rangle$-rows fill (113) intercalation planes separated by four Bi-free (113) layers. See Fig. 4.3(d) for a cross sectional view illustration. Note that intercalated structures have been found for other

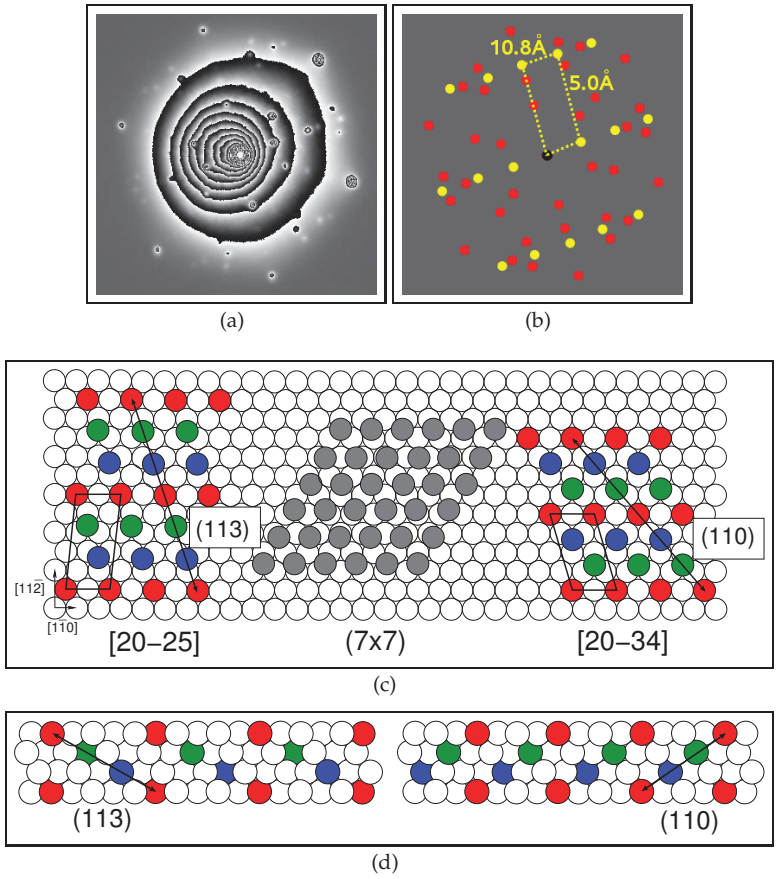

FIG. 4.3: (a) Cumulative μLEED pattern for energies from 3.0 to 20.0 eV in steps of 0.1 eV for the nanowire surrounded by wetting layer. (b) Schematic diffraction pattern corresponding to Fig. 4.3(a), where red spots correspond to the (7×7) wetting layer pattern and yellow spots correspond to the nanowire pattern. The superstructure of the nanowire is drawn. The short axis of the unit cell is aligned parallel to the close packed Ni $\langle 110 \rangle$-azimuth. (c) shows a top view cartoon of the real space unit cells for (from left to right) the $\begin{bmatrix} 2 & 0 \\ -2 & 5 \end{bmatrix}$ Bi surface alloy, the Bi (7×7) wetting layer and the $\begin{bmatrix} 2 & 0 \\ -3 & 4 \end{bmatrix}$ Bi surface alloy. For the surface alloy structures, the red Bi atoms are within the top layer of the substrate plane, which at the same time is the first layer of the nanowire. The blue Bi atoms are in the second nanowire layer. The green Bi atoms are in the third layer. The fourth layer Bi atoms are then in the red positions again. In other words: the Bi nanowire is viewed as a Bi-containing Ni film with fcc structure. The Ni atoms in the higher layers are not shown for display purpose. Panel (d) shows the cross sectional view of the Bi surface alloys for a four layer high structure. For the two Bi surface alloys the (113)- and the (110)-intercalation planes are indicated. The Bi-rich directions are the $[1\bar{1}0]$ direction and the $[12\bar{1}]$ and $[1\bar{1}2]$ directions that define the (113)- and (110)-planes, respectively.

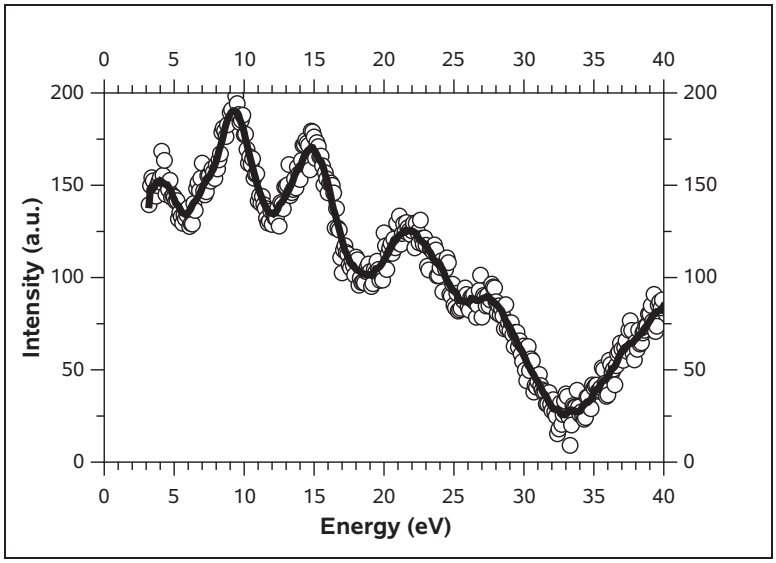

FIG. 4.4: I/V-μLEED data obtained from the (1,0)-peak of the structure shown in Fig. 4.3(a). The maxima and minima are used to calculate Δk_z components in Fig. 4.5. A linear background profile has been subtracted.

BiNi alloys [53, 56]. As a consequence the (111)-interlayer spacing is found to be 2.2 Å, i.e. marginally larger than the Ni-value. In order to observe the measured interference effects the film has to be at least four layers thick. An even stronger interference would result from a thicker film with for instance a height of 6 layers. The thickness of the nanowires must therefore be at least 6.6 Å. This is further discussed below. Note that the width of the (1,0) nanowire diffraction peaks is constant within the error margins, making interference due to atomic steps improbable [57]. This provides support for the assumption that the interference effects responsible for the particular behavior of the peak height in Fig. 4.4 are due to interference inside the crystal.

Shortly after nucleation of the $BiNi_9$ nanowires, different, coexisting domains with different heights and crystal structures appear which are electronically stabilized through the accommodation of their specific Fermi wavelength. The details of the electronic growth of these film structures are discussed in Chapter 3. Figure 4.6 shows these QSE stabilized islands, labeled with their height of three and five atomic layers. The height is measured with respect to the bare Ni(111) substrate. Two parallel nanowires are highlighted by the text 'nanowire'. As the coverage is increased we observe the QSE stabilized island of height three, on the left in Fig. 4.6, to cross steps of the substrate. We observe a slight roughening of the steps with increasing coverage upon examining the position of the step marked by the white dashed line, see Figs. 4.6(b) and (c). We also see a sig-

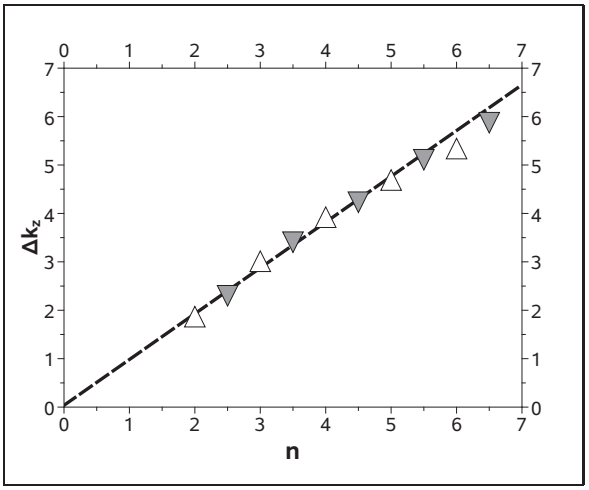

FIG. 4.5: Calculated Δk_z values found for in-phase n (up triangles) and out-of-phase $n + \frac{1}{2}$ (down triangles) conditions from the maxima and minima in the I/V-μLEED data shown in Fig. 4.4. The dashed line has a slope of 0.9455Å^{-1} where the coefficient of determination equals 0.991.

nificant displacement in the downward direction, from bottom-left to top-right. From this observation, as well as our coverage calibration, we conclude that the (7×7) wetting layer is not exclusively composed of Bi atoms, but in fact comprises the underlying substrate top layer as well. The (7×7) wetting layer has to contain a small amount of Ni, with the substrate top layer holding an equally small amount of Bi. The growth of QSE stabilized structures then leads to reordering of the wetting layer, fully dealloying the Bi and Ni in the process. The Ni then attaches to steps, causing them to meander slightly.

Figure 4.6(b) shows the blocking of the growth front of the QSE stabilized structure by a nanowire. As soon as the nanowire is surrounded by the three layer high structure, the nanowire gradually disappears into the QSE stabilized structure. Since the nanowires consist of 90% Ni atoms, their gradual disappearance also leads to meandering of steps in the downward direction, as shown in Fig. 4.6(c) by the black dashed line. By measuring the increase in terrace area due to the step advancement as a result of the dealloying of the nanowires with a 10% Bi content, the height of the nanowires is estimated to be 3.9 ± 0.5 layers, in agreement with the previous analysis from the I/V-μLEED measurement in Fig. 4.4.

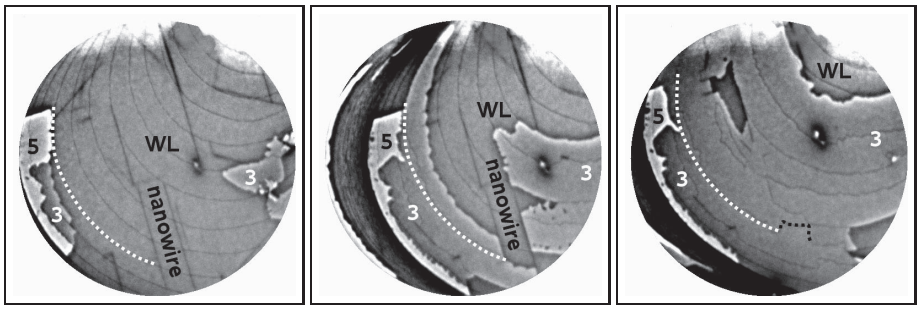

(a) (b) (c)

FIG. 4.6: (a-c) LEEM images showing nanowires acting as limitations for the expansion of the electronic driven growth of the domains. Dealloying of the nanowires and the wetting layer results in meandering steps. QSE driven islands are labeled with their respective height, WL denotes the (7×7) wetting layer. The initial Ni(111) substrate steps appear as curved dark lines, one example is indicated by the white dashed line in (c). The movement of the step position near a disappearing nanowire is shown by the black dashed line. FoV=10 μm, electron energy 2.0 eV, T=474 K, (a) $\theta_{Bi/Ni} = 0.65$ ML, (b) $\theta_{Bi/Ni} = 1.00$ ML, (c) $\theta_{Bi/Ni} = 1.35$ ML.

4.4 Discussion

From the cumulative μLEED pattern in Fig. 4.3(a) the surface structure of one of the three-fold symmetric nanowire types is found to be $\left[\begin{smallmatrix} 2 & 0 \\ -2 & 5 \end{smallmatrix}\right]$. Since the distance between embedded Bi-atoms is smallest along the $[12\bar{1}]$ direction, being $\sqrt{3} \times a_{nn}$, with a_{nn} the Ni nearest-neighbor distance, we expect the nanowires to grow along the $[\bar{3}21]$-azimuth. This actually offers an attractive explanation for the observation of approximately perpendicular nanowires, see Fig. 4.2, which are symmetry forbidden on an fcc(111) surface. With an evaluation scheme similar to the one leading to (113) Bi-rich planes intercalated with Bi-poor planes in a ratio of 1 to 5, we arrive at Bi-rich lines along $[1\bar{1}0]$ and $[1\bar{1}2]$ directions, which set up (110) planes as shown in Fig. 4.3(c) and (d) (right). The corresponding unit cell is written as $\left[\begin{smallmatrix} 2 & 0 \\ -3 & 4 \end{smallmatrix}\right]$. The Bi-content in this structure is 12.5%. From the smallest Bi distance of $\sqrt{3} \times a_{nn}$, the corresponding propagation direction of these nanowires is to be expected along the $[\bar{3}12]$-azimuth. As a consequence both sets of nanowires have angles of 22° or 82°, i.e. consistent with the angles measured in Fig. 4.2. Unfortunately, we have not been able to collect sufficiently reliable data for the latter set of nanowires and the (110) Bi-rich intercalated plane in a 1 to 4 ratio remains a speculation here. Both structures however do posses the essential property that is necessary for the formation of nanowires. The placement of the Bi atoms in the (113) and (110) crystal planes of both types of nanowires induces an anisotropy in the alloying induced strain. This is a key requirement

for the structure to form nanowires [46, 47].

Both the height and structure of the $BiNi_9$ nanowires have been characterized by (I/V-)μLEED. The perpendicular periodicity corresponds to three (111) Ni layers in an fcc stacking configuration, containing 10% Bi. In principle the interference could be the result of steps in the vacuum-nanowire interface too. The fact that the straight line in Fig. 4.5 intersects the origin, thereby indicating a negligible inner potential difference, seems to suggest that. However, the discussed interference effect should give rise to peak broadening under destructive interference conditions, e.g. Ref. [57]. Such effects are not supported by the experimental data, which could be due to the transfer width of the instrument in combination with the length scale of the atomic steps. However, since more explanations for the intersection of the origin in Fig. 4.5 may apply, including e.g. relaxation within the nanowire, we are inclined to think in terms of a well defined and constant height of the nanowires across their width profile.

4.5 Summary

Using LEEM and μLEED, we have characterized both the (7×7) wetting layer and $BiNi_9$ nanowires. The nanowires show lengths up to about 10 μm. Making use of I/V-μLEED data we found the height of the nanowires to be 4-6 atomic layers with respect to the substrate. The nanowires assume a $\begin{bmatrix} 2 & 0 \\ -2 & 5 \end{bmatrix}$ superstructure, containing 90% Ni. The nanowires have an fcc stacking with each fifth (113) intercalated plane containing 50% Bi. Due to the incomplete dealloying of the $(\sqrt{3} \times \sqrt{3})$-R30° surface alloy at coverages $\theta_{Bi/Ni} > 0.33$ ML, the (7×7) wetting layer in fact comprises two layers of which the lower one, the top substrate layer, contains a small but finite Bi content. The (7×7) wetting layer may contain a minor fraction of Ni. Upon the QSE driven growth of three and five layer high structures on top of the bare Ni(111) substrate, dealloying of the wetting layer and nanowires results in meandering of steps in the step down direction, as is imaged with LEEM.

Quantum Size Effects on surfaces without projected bandgap: Pb/Ni(111)

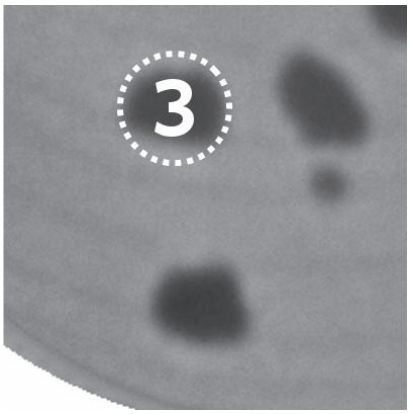

5

We have studied the initial growth of Pb on Ni(111) using Low Energy Electron Microscopy (LEEM) and selective area Low Energy Electron Diffraction (μLEED). First, a one layer high wetting layer develops consisting of small (7×7) and (4×4) domains. For larger coverages, Pb mesas are formed which are embedded in the wetting layer. In spite of the absence of a projected bandgap on clean Ni(111), we observe distinct Quantum Size Effect (QSE) driven preferred heights. These become apparent from a variety of frequently occurring island height transitions during growth, both on wide terraces and across substrate steps. Also the average island heights that evolve during deposition at 422 K and 474 K show a clear signature of QSE driven preferred heights. These distinctly include 5, 7 and 9 layers and thus correspond nicely to the values obtained in the key examples of QSE: Pb films on Si(111) and Ge(111). We suggest that the Pb induced surface modification of Ni(111) shifts the Fermi level into the gap of the interface projected Ni bulk bands, thereby effectively causing decoupling of the Pb states with the bulk Ni states.

5.1 Introduction

With their low surface free energy, Pb films tend to wet most surfaces. However, Quantum Size Effects (QSEs) often result in distinct preferred heights for isolated Pb islands [29]. The self-organization into these island heights due to QSEs, referred to as quantum growth or electronic growth, has been observed recently on different substrates and has been characterized with a variety of techniques [30, 49, 58, 59]. A prototypical example of QSEs is provided by thin Pb(111) films. For Pb(111) with $d \approx 0.75\lambda_F$, where d is the interlayer distance and λ_F the Fermi wavelength, every increment by two layers almost perfectly accommodates three additional antinodes of the Fermi wavefunction. Recently, many intriguing features were discussed for the growth of Pb on Si(111) [58, 60–63] where flat top Pb islands with steep edges grow to specific integer heights that are stabilized by QSEs. It was shown that Pb mesas grown on both Si(111) and Ge(111) are atomically smooth at substrate temperatures of 200-300 K. The growth shows a strong preference for a bilayer increment in height on top of a wetting layer which is thought to passivate the substrate. The stable thicknesses found for Pb/Si(111) are initially odd layer heights 5, 7, 9, 11 and 13, crossing over to even layer heights 14, 16, 18, 20 and 22 thick *on top* of the wetting layer. The crossing from preferred odd to even island heights and vice versa shows a long 9.5 layer beating pattern as a result of the slight incommensurability of the Fermi wavelength to the interlayer distance [3, 5].

Typically for QSEs to manifest themselves, quantum well states have to form in the metallic overlayer. This is for instance the case on Cu(111) and Ag(111) substrates, in contrast to Ni(111) [64]. Indeed Pb layers on Cu(111) show strong evidence for the presence of quantum well states [49, 65]. A closer inspection of the calculations by Goldmann et al. [64] shows that the projected band structure obtained for the clean Ni(111) resembles Cu(111) and Ag(111). At the Γ point, the projected bulk band maximum is only 0.2 eV above the Fermi level and the crystal derived surface bands are in its close vicinity. Therefore, Ni(111) is an interesting candidate to investigate whether an interface projected band gap develops upon the deposition of Pb, thereby facilitating quantum well states in thin Pb films.

Here we present a study of the growth of thin Pb films and islands on the Ni(111) substrate and their subsequent temporal evolution as a result of QSE driven growth. Using in situ Low Energy Electron Microscopy (LEEM) and selected area Low Energy Electron Diffraction (μLEED) we are able to probe properties of different selected microscopic sample areas in real time. Using LEEM we are also able to measure the island height evolution during growth, thereby revealing electronic growth driven transitions of Pb islands. Using μLEED we are able to probe the ordering of the Pb films and determine their structural properties.

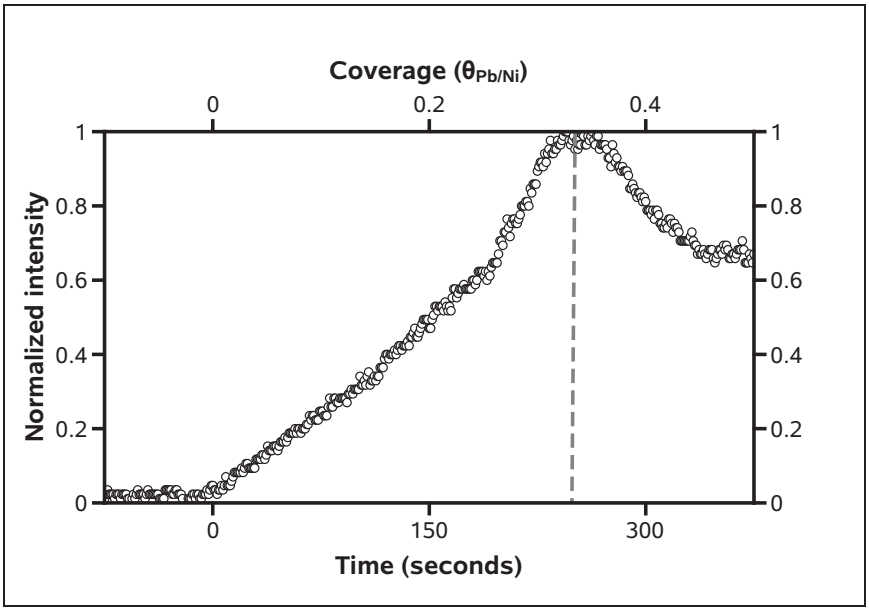

FIG. 5.1: Integrated spot intensity for the $(\frac{1}{3}, \frac{1}{3})$ surface alloy diffraction peaks. The shutter was opened at $t = 0$ seconds. The maximum at $\theta_{Pb/Ni} = 0.33$ ML is used for in situ calibration of the deposition rate.

5.2 Experimental

The experiments were performed in an Elmitec LEEM III instrument. A Ni(111) surface was cleaned by successive cycles of 1 keV Ar^+ bombardment at RT, followed by flash annealing to a temperature of 1150 K. The cleanliness of the sample was monitored by Auger Electron Spectroscopy (AES) and LEEM. LEEM images revealed terraces with a width of $\sim$1 μm. All sample temperatures are subject to an uncertainty of 5% and were calibrated using the uphill motion of steps over time at a temperature where sublimation is observed, as described in Ref. [24]. Lead was deposited from a Knudsen cell. According to the bulk phase diagram, Pb and Ni are immiscible in the bulk [66]. The typical deposition rate used in the experiments was about 1×10^{-3} ML/s where a coverage of $\theta_{Pb/Ni} = 1$ ML corresponds to 1 Pb atom per Ni surface atom.

5.3 Results and discussion

5.3.1 Wetting layer properties

To determine the properties of a single Pb layer on top of the Ni(111) surface we performed μLEED illuminating a circular area of 19 μm in diameter. When depositing Pb on the clean Ni(111) surface at a temperature of 474 K, we find a faint $(\sqrt{3} \times \sqrt{3})$-R30° surface alloy peak emerging, showing its maximum peak intensity at a coverage of 0.33 ML, corresponding to 250 seconds of deposition, see Fig. 5.1. The measured deposition rate is therefore 1.3×10^{-3} Pb atoms per unit cell (uc) per second (Pb/uc/s). The $(\sqrt{3} \times \sqrt{3})$-R30° surface alloy was also found in literature, where annealing to $T > 850$ K followed deposition at RT before alloy formation occurred [37, 38, 67, 68]. A further increase in coverage results in dealloying and the formation of a Pb wetting layer that covers the entire surface above $\theta_{Pb/Ni} \approx 0.40$ ML. From this coverage onward, new diffraction peaks emerge at a position corresponding to an in-plane lattice constant of 3.93 Å, giving rise to a weak moiré pattern. These Pb peaks move outward with increasing coverage, indicating a continuous compression of the aligned and incommensurate hexagonal Pb layer. The coverage in this wetting layer is increasing as a result of both the addition of Pb from the gas phase, as well as from continuous dealloying. The rate of dealloying is increasing with coverage, as can be concluded from the convex shape of the in-plane lattice constant versus coverage curve in Fig. 5.2(a). The wetting layer is completed when the compression of the in-plane lattice constant abruptly ends at a value of 3.50 Å. At this point the dealloying and the compression stops. It provides an excellent opportunity for an exact in situ calibration of the deposition rate. The resulting deposition rate is 1.33×10^{-3} ML/s , in agreement with the value obtained from the maximum peak intensity of the $(\sqrt{3} \times \sqrt{3})$-R30° surface alloy. We find no indication for the locking in of the previously reported (3×3) structure found at RT [38, 67, 68], at an in-plane lattice constant of 3.73 Å.

Beyond a coverage of $\theta_{Pb/Ni} = 0.51$ ML, the line profiles shown as insets in Fig. 5.2(a) exhibit an unexpected peak splitting. The splitting reveals two different domains in the wetting layer, as illustrated by the μLEED pattern. These two domains are the (7×7) and (4×4) structures with lattice constants of 3.50 Å and 3.32 Å. Both have been reported on in literature [67, 68] and are illustrated in Fig. 5.2(b) and (c). For increasing coverage the main spot intensity moves gradually from the less dense (7×7) domains at $\theta_{Pb/Ni} \approx 0.51$ ML to the denser (4×4) domains at $\theta_{Pb/Ni} \approx 0.55$ ML, as is reflected in the line profiles shown as insets in Fig. 5.2(a). This remarkable double domain structure of the wetting layer is unanticipated and found to disappear at 520-525 K, resulting in the anomalous transition of Pb mesas into hemispheres described in Chapter 6. With the nearest neighbor distance in bulk Pb being 3.50 Å and the known generic tendency for tensile surface stress [69], we suggest that the (7×7) domains in the wetting

layer involve tensile stress. A slight compression then locks the (4×4) domains.

To discuss the stability of both domains, we perform a coordination analysis. As a measure of the coordination of an individual Pb atom we take the sum of the lateral components of its position vector, measured along the directions of the 3 nearest Ni atoms underneath, relative to those values for an atom in a hollow site. For an on-top site, bridge site and three-fold hollow site we find a value of: 1.734, 0.444 and 0 respectively, expressed in Ni lattice constants. The average numbers for the (7×7) and the (4×4) structures are 0.550 and 0.618. This clearly suggests that the coordination is higher, and thus the binding stronger, for the (7×7) than for the (4×4)-structure, in line with our observations. The strong binding to the Ni(111) substrate results in the accumulation of lateral stress, forcing the system to relieve this by keeping the compressed (4×4) domains small and alternating them with the low tensile stress (7×7) domains. These Pb domains with different surface stress can give rise to self-assembly [1]. A typical example is the striped phase formation of Pb on Cu(111) driven by a competition between tensile and compressive stress of a PbCu surface alloy and a Pb overlayer phase [2]. Here, the energy involved in the creation of the domain walls is low due to the alignment to the Ni substrate and the similar atomic density of the (7×7) and (4×4) domains. This results in small domains with probably fast fluctuations. These domains are not resolved, probably because of the spatial resolution of our instrument of about 7 nm, possibly in combination with fast fluctuations at these temperatures.

For coverages $\theta_{Pb/Ni} > 0.55$ ML, small Pb islands form. For these and all other structures grown, μLEED shows only the bulk nearest neighbor distance for completely relaxed Pb(111), coexisting with the strained double domain wetting layer. This observation is an illustration of the low misfit energy, which also allows for the gradual in-plane lattice constant compression of the incommensurate wetting layer, as shown in Fig. 5.2(a). The relatively low misfit energy is attributed to the large difference in atomic radii for Ni and Pb.

From here onwards, we define the coverage $\theta_{Pb} = 1$ ML as being the equivalent of one bulk Pb(111) layer.

5.3.2 Electronic growth driven shape transitions of Pb islands

An eye-catching feature of the evolving morphology of the growing Pb film is the apparent difference in growth rates of the individual islands. A significant fraction of the islands even appear to shrink in fractional area. These remarkable events occur both for islands far away from substrate steps as well as for those located at or in the direct vicinity of substrate steps. They also occur both during initial and more advanced stages of growth and are all explained in the context of QSE driven stable island heights, as described in reference [32]. We consider them as strong indications of the importance of QSEs for Pb on Ni(111).

After completion of the wetting layer, Pb island nucleation is observed for coverages beyond $\theta_{Pb} \approx 1.08$ ML, imaged as dark features in Fig. 5.3 and Fig.

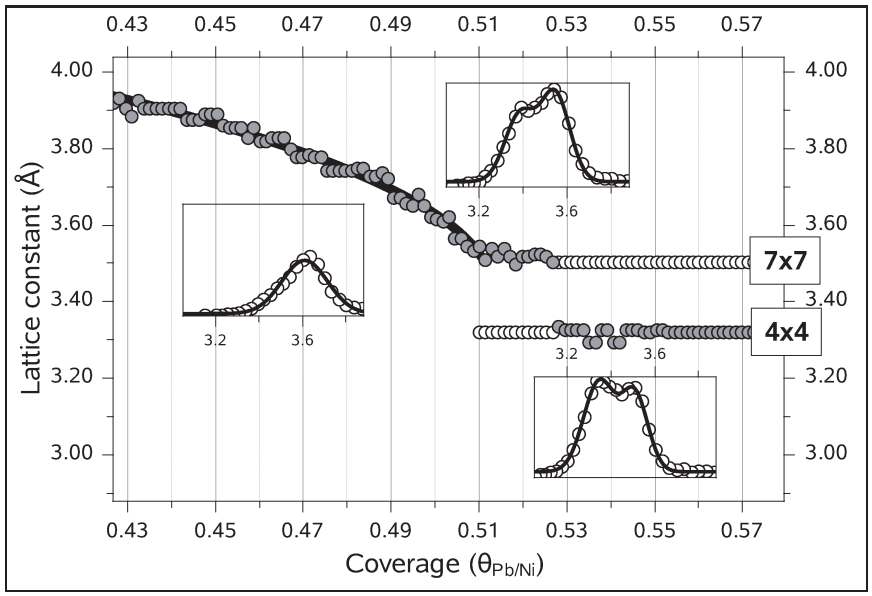

(a)

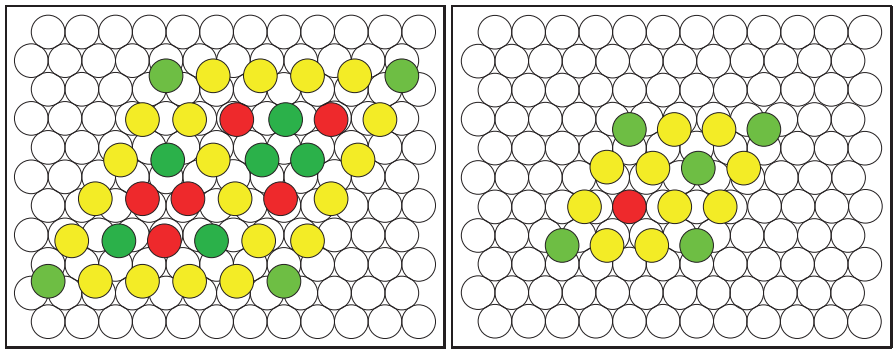

(b) (c)

FIG. 5.2: (a) The in-plane lattice constant as derived from the position of the Pb(1,0)-LEED spot (35.0 eV) during Pb deposition at 474 K. Snapshots of the corresponding peak lineprofiles are shown for the three different regions as described in the text. The in-plane lattice constant of 3.50 Å corresponds to the (7×7) structure of the wetting layer with a coverage of 0.510 ML, where the in-plane lattice constant of 3.32 Å corresponds to the (4×4) structure of the wetting layer with a coverage of 0.563 ML. (b) and (c) The real space unit cells for the (7×7) (b) and (4×4) (c) structures of the wetting layer. Colors green correspond to three-fold hollow, darker green to close to three-fold hollow, red to (near) on-top, yellow to intermediate positions.

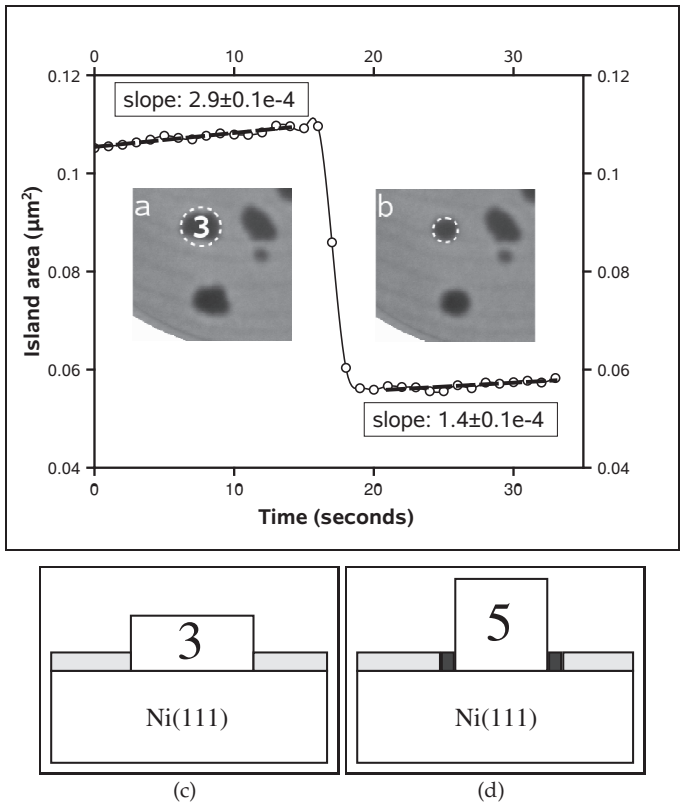

FIG. 5.3: Island area of the island shown in the insets versus time. Insets (a) and (b) show 1560×1560 nm^2 LEEM images recorded at an electron energy of 20.0 eV after deposition of θ_{Pb} =1.28 ML at 422 K. (c) and (d) Cartoons of the shape transition. Colors correspond to wetting layer (grey) and increase of fractional area of wetting layer due to island height transition (dark grey).

5.4. The experiment shown in Fig. 5.3 and Fig. 5.4 is performed at a slightly lower temperature of 422 K. During the growth of these small islands, we observe the sudden collapse of their fractional area within a few seconds. In Fig. 5.3 and Fig. 5.4 two examples are shown. Island areas are measured making use of common image analysis techniques such as background subtraction, Otsu's method to automatically perform histogram shape-based adaptive image thresholding [70], and standard erosion and dilation filters, see also Appendix C. Quite abundantly we can distinguish islands that undergo a reduction in fractional area between frames. The condition of mass conservation leads to the conclusion that the islands must undergo a height increase at the same time.

We first focus on the LEEM image insets in Fig. 5.3 and the corresponding car-

toons underneath. Going from image (a) to (b), taken only 7 seconds apart, we observe a distinct reduction in the fractional area of the highlighted island. This is exemplified in the plot in Fig. 5.3 showing the fractional area versus time. The ratio of the final and the initial projected areas, respectively A_5 and A_3, equals $R_A = 0.50$. Since neither mass transport between this island and any of its neighbors occurs, nor any intensity fluctuation in its surroundings takes place, mass conservation must apply. The reduction in fractional area must therefore be accompanied by a corresponding increase in height, see the cartoons in Fig. 5.3(c) and (d). The wetting layer (grey) has an approximately 8% higher density than the completely relaxed Pb(111) layers in the islands. The height of the islands is counted with respect to the substrate. Assuming mass conservation the following condition must apply: $3 \times A_3 = 5 \times A_5 + 1.08 \times (A_3 - A_5)$. This gives $R_A = \frac{A_3}{A_5} = 0.49$, i.e. the ratio R_A is identical to the measured value within the experimental uncertainties. The conclusion is that the transformation of the island is from a 3 layer high island into a 5 layer high island. Keeping in mind that the measurement takes place during the deposition of Pb, the growth rate of the islands must differ by a factor of 2. Indeed this is nicely confirmed by the two times higher expansion rate of the three layer high island compared to the five layer high one, as inferred from the measured slopes in Fig. 5.3. These findings provide strong support for the assessment of a transition from a three layers high island into an island with the preferred height of five layers. We attribute this bilayer height transition to QSEs.

A similar feature is illustrated for the LEEM image insets in Fig. 5.4. Here we start with a larger island situated near a descending step in the Ni(111) substrate. The reduction of the fractional area of this island is plotted in Fig. 5.4. The transition occurs in a more complex way, but the overall result is a ratio of the final fractional area to the initial one of 0.75. For a transition from a four layer high island to a preferred five layer high island, shown in the cartoons in Fig. 5.4(c) and (d), mass conservation conditions imply $4 \times A_4 = 5 \times A_5 + 1.08 \times (A_4 - A_5)$, which gives $R_A = \frac{A_4}{A_5} = 0.74$, consistent with the experimental value within the experimental uncertainties. The scatter in the growth rate is in this case much larger, but again the obtained result of the final growth rate being 0.64 times smaller than the initial one is consistent with the expected factor of $\frac{2}{3}$. So again, in this transition of the island we find strong evidence for a preferred island height of five layers. We conclude that the data in Fig. 5.3 and 5.4 demonstrate the importance of QSEs in this system. Note that the growth rate of the island in Fig. 5.3 is two times larger than that found for the island in Fig. 5.4. This difference is attributed to the influence of substrate steps in the vicinity of the islands.

From the conservation of the total amount of deposited material and the observed height transitions, we can also derive that the Pb(111) islands grow directly on the metallic Ni(111) substrate and are surrounded by the wetting layer consisting of both (7×7) and (4×4) domains. This is in contrast to Pb and Bi

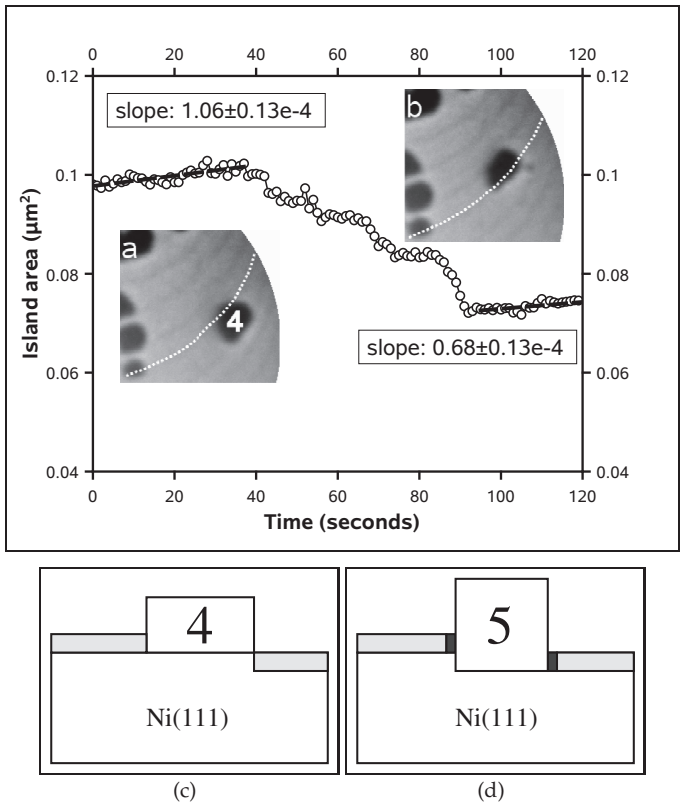

FIG. 5.4: Island area of the island shown in the insets versus time. Insets (a) and (b) show 1560×1560 nm^2 LEEM images recorded at an electron energy of 20.0 eV after deposition of θ_{Pb} =1.47 ML at 422 K. The island traverses the substrate step that is in contact with the island, indicated by the dashed line, from 40-90 seconds. The interaction with the step slows the transition down (compare Fig. 5.3). (c) and (d) Cartoons of the shape transition, colors as in Fig. 5.3(c) and (d).

on Si(111), where the semiconducting substrate is first passivated by the wetting layer before electronic growth starts on top of it [3, 34, 39].

After prolonged deposition at a slightly higher temperature of 474 K, islands can achieve large fractional areas. Adjacent islands can make concerted movements in an attempt to minimize their energy. Figures 5.5(a) and (b) show an example at an average film thickness of about 17.5 layers. A concerted movement across a step enables a height transition of one of the islands. The two islands taking part in this concerted movement are labeled by their contours in white and gray and are assumed to initially have the same uniform height, h, composed of n layers. The Ni substrate step in between these islands is marked

by the white dashed line. As a result of the net flow of Pb atoms from the grey labeled island towards the white labeled island across the substrate step, both islands reduce their projected area as is shown in Fig. 5.5(a) and (b). The filled circles in the graph in Fig. 5.5(c) show the total measured fractional area times a constant height h. Assuming that both islands initially are smooth and thus have a uniform height, as well as assuming mass conservation, a height doubling of the white labeled island results in the open circles in Fig. 5.5(c). This curve represents the fractional area multiplied with a time dependent height $h(t)$ for the white labeled island, where $h(t)$ is a step function that is equal to h for $\theta_{Pb} < 8.439$ ML and $2h$ for $\theta_{Pb} \geq 8.439$ ML. The transition region, $\theta_{Pb} = 8.439 - 8.447$ ML, shows that the atomic rearrangement takes less than 10 seconds. For the LEEM images shown in Fig. 5.5(a) and (b) the average island height, calculated from a total fractional island area of 47.7%, is about 17.5 atomic layers. It is therefore likely that the white labeled island makes a transition from a layer height of e.g. 9 layers to 18 layers. From literature it is known that Pb(111) films are rather special in that the Friedel oscillations at their surface allow strong QSEs to persist even over 30 atomic layers thickness [5]. The slight incommensurability of the Fermi wavelength to the interlayer distance results in periodic crossovers in the stability of odd versus even layer heights [32]. This provides strong support for the height transition of the white labeled island from an odd layer height below 11 (e.g. 7 or 9) atomic layers, to an even layer height (e.g. 14 or 18). From average island height measurements we also found stable island heights of 7 and 9 layers at 474 K, discussed below and visualized in Fig. 5.7. These are in agreement with the observation in Fig. 5.5 and the corresponding proposed height of less than 11 atomic layers. We note that a comparison of the growth rate of the resulting island with those found previously, see e.g. Fig. 5.4, is consistent with this assignment. We also note that the local free energy minima near the transition from odd to even crossover of preferred layer heights facilitate a big leap instead of an incremental increase of the island height [3].

Figure 5.6 shows another example of the strong preference for specific QSE stabilized heights. In the center of the 4 μm wide image in Fig. 5.6(a), a QSE stabilized island has expanded its area up to the full terrace width, where the bounding steps are marked by white dashed lines. As soon as it extends slightly over the descending step, the height on the lower terrace becomes one atomic layer higher which is energetically less favorable due to the bilayer periodicity of stable island thicknesses. Therefore, it becomes energetically more favorable for the island to split in two separate islands, one on each terrace with similar heights, see the cartoons in Fig. 5.6(c) and (d), despite the creation of additional island boundaries. The average island height in Fig. 5.6, calculated from the islands total fractional area, is about 15 layers. Since the heights of both islands are very similar, we are not able to assign exact island heights within the experimental error of the fractional area. Fourteen and sixteen layer high islands would be likely candidates.

In order to gather more dynamic and global information on the evolution of

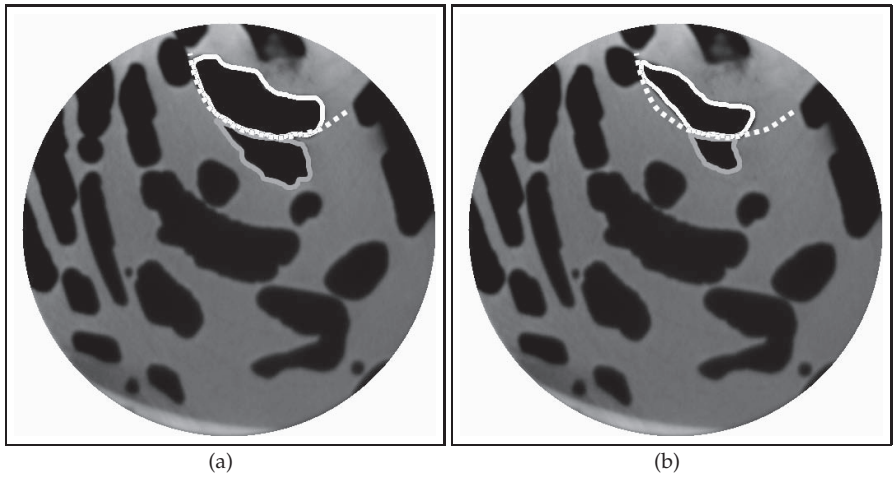

(a) (b)

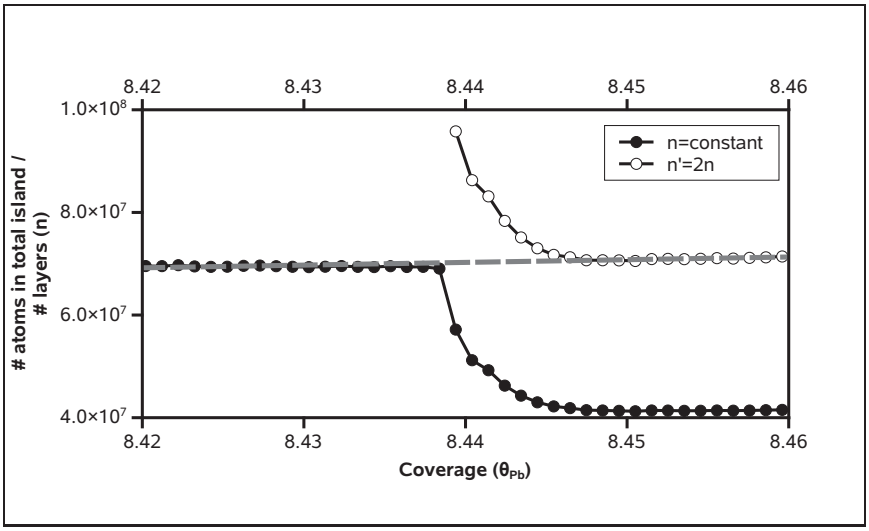

(c)

FIG. 5.5: (a) and (b) LEEM images (FoV=15 μm, electron energy is 20.0 eV, $\theta_{Pb} = 8.42$ ML and 8.46 ML) showing a concerted movement of the islands indicated by the white and grey contour. The substrate step in between is drawn as a white dashed line. (c) Graph of the calculated number of island atoms divided by the number of layers (n). A decrease in fractional area, is shown by the filled circles for n being constant. Assuming island height doubling $(n' = 2 \times n)$ of the white labeled island for $\theta_{Pb} \geq 8.439$ ML, results in conservation of the atoms contained in the island (open circles).

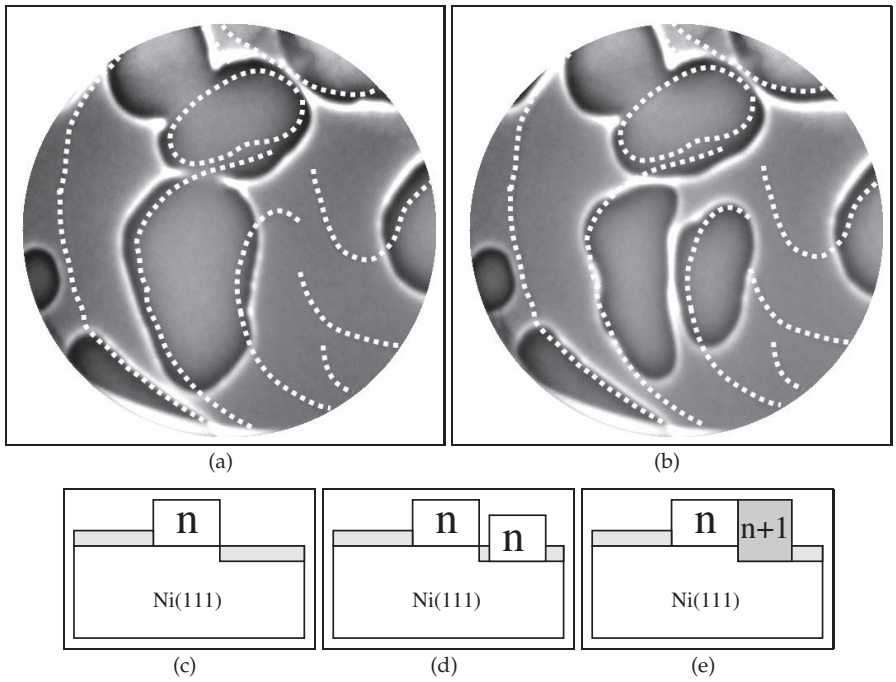

FIG. 5.6: (a) and (b) LEEM images (FoV=4 μm, electron energy is 5.0 eV, θ_{Pb} =4.57 ML and 4.79 ML) showing the splitting of an island over a substrate step in order to regain an energetically favorable QSE stabilized height. The substrate steps are drawn as white dashed lines. (c-e) Cartoons corresponding to the island splitting over a substrate step, where the final situation in (d) is stable according to the bilayer periodicity of stable island thicknesses. For the same reasoning (e) is unstable.

the island height, we measured the *average* island height for a large number of frames for coverages from θ_{Pb} = 1.0-2.5 ML. In Fig. 5.7 such measurements are shown for temperatures of 422 K and 474 K, where the island density for the latter is lower. From Fig. 5.7, the tendency of both curves to flatten at 5 layers for 422 K, at 7 layers, and less pronounced at 9 layers for 474 K, is attributed to a strong preference for QSE stabilized island heights. Islands reach an energetically stable height and merely expand laterally. Keeping in mind that we consider average values for the island heights and that we are dealing with a distribution of island heights, we have to consider the tendency for a preferred height as strong support for its existence. The measured QSE stabilized heights of 5, 7, and 9 atomic layers show bilayer periodicity and are in agreement with literature [3, 32, 71]. For the higher temperature of 474 K, the first stable height is 7 atomic layers. At a slightly lower temperature the first stable height appears to be 5 atomic layers. However, we have seen clear evidence for the ex-

Film thickness (layers)	2	3	4	5	6	7	8	9	10	11
Ni(111)	u	s	u	s	u	s	u	s	-	-
Ge(111)($\sqrt{3}\times\sqrt{3}$)-α [3]	-	-	-	s	u	s	u	s	u	s
Si(111)(7×7)-Pb [3]	-	-	-	s	u	s	u	s	u	s
Si(111)($\sqrt{3}\times\sqrt{3}$)-α [3]	-	-	-	s	u	s	u	s	u	s

Table 5.1: A summary of the observed stable heights found for Pb films *on top* of the Ni(111) substrate, 's' stands for stable, 'u' stands for unstable. For comparison the experimental observed stable heights for Pb films *on top of a wetting layer* on Ge(111) and Si(111) are shown, data taken from Ref. [3]. See also Fig. 5.3, Fig. 5.4 and Fig. 5.7.

istence of 3 layer high islands (see above). From the fact that the curve for the 422 K data starts at 4 layers for $\theta_{Pb} = 1.0$ ML, where exact data is missing up to $\theta_{Pb} = 1.15$ ML due to readjustment of the instrument, we are probably dealing with a mixture of both 3 and 5 layer high islands. The first are metastable at this temperature. Consequently, this data may provide the first experimental evidence for preferred 3 layer high islands in electronic growth of Pb films, as predicted from theory [3, 71]. The 'noise' at the start of the 422 K data can actually be traced back to transitions from 3 layers to 5 layers and is by no means just a statistical feature. For increasing coverages, the spread in island heights increases, and therefore the flattening in Fig. 5.7 becomes less pronounced.

Table 5.1 summarizes the observed stable heights in our experiments in comparison to those found for Pb on Ge(111) and Si(111) [13, 30]. Note that the growth of QSE driven Pb islands occurs *on top* of the wetting layer for Pb/Ge(111) and Pb/Si(111), where in the case for Pb/Ni(111) the islands grow directly on the bare substrate.

5.3.3 I/V-LEEM interpretation

We have discussed the electronic growth observations of Pb on Ni(111) using the morphological changes in our LEEM observations. We now focus on the interpretation of the I/V-LEEM curves obtained from the Pb islands. By varying the incident electron energy while measuring the reflected intensity, I/V-LEEM curves of the (0,0) beam at normal incidence can be obtained. Typically, these I/V-LEEM curves exhibit pronounced quantum interference peaks, resulting from the QSE. The positions of these peaks can be easily predicted by a simple Kronig Penney (KP) model, see Ref. [20] for a full description. In short: The KP model uses two potential boxes for each layer, with depth V and width w, centered at the atoms (V_a,w_a) and in between the atoms (V_g,w_g). The substrate is given as a featureless box with depth V_{0s}. By requiring the wave functions and their first derivatives to be continuous at the various transitions, including the vacuum-film interface, we can derive the reflection coefficient at the latter interface, which represents the measured quantity. The result is $N-1$ interfer-

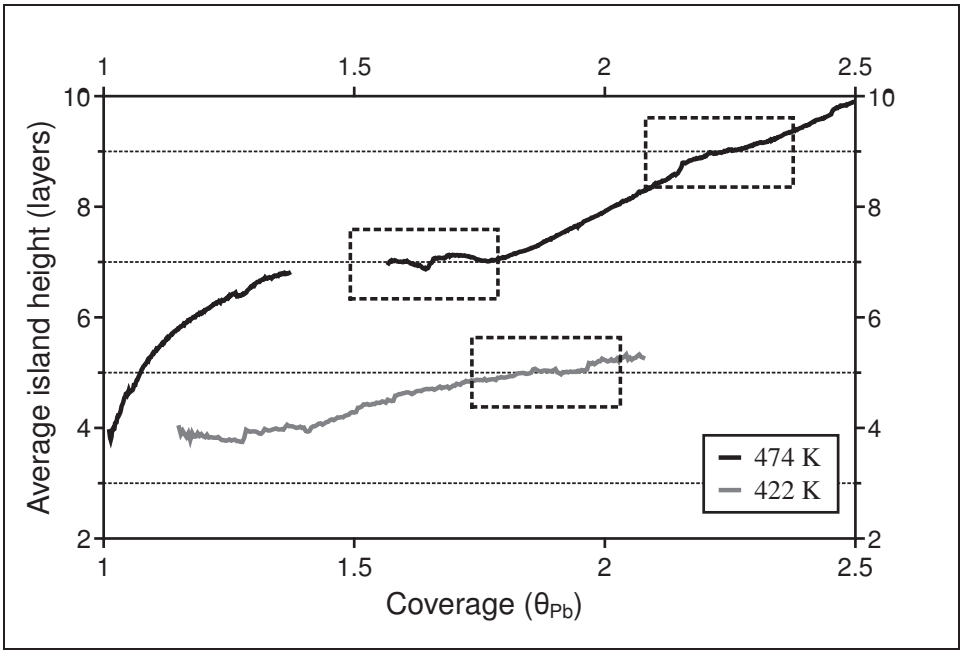

FIG. 5.7: The average island height as a function of coverage for temperatures of 422 K and 474 K. Stable island thicknesses of 5, 7, and 9 atomic layers are found.

Parameter	V_a(eV)	V_g(eV)	V_{0s}(eV)	w_a(Å)	w_g(Å)
Value	20.7	10.2	20.0	1.35	1.70

Table 5.2: Parameters used for the KP model shown in Fig. 5.8(a). The values are based on Table 3.1.

ence peaks for a N layer thick film. Analogous to the Pb on Ni(111) system, these predicted interference peaks were also found for the electronic growth of Bi on Ni(111) for island heights of 3 and 5 atomic layers, see Chapter 3.

Figure 5.8(a) shows the measured I/V-LEEM curves for a 5 atomic layer high island, where the height is determined with an evaluation scheme similar to the one used in Fig. 5.3 and Fig. 5.4. A small but distinct quantum interference peak can be found at 3.5 eV and 11.9 eV, marked by arrows. The peak intensity of the quantum interference peaks (I_{QSE}) is rather small in comparison to the Bragg peak intensity (I_{Bragg}) around 22.0 eV, marked by the character B in Fig. 5.8(a) and (b), with a typical ratio of $\frac{I_{Bragg}}{I_{QSE}} \approx 20$. The S/N-ratio is limited by the available intensity.

In order to qualitatively understand the distinct interference peaks in Fig. 5.8(a) we propose a simple KP model. Since no parameters for the Pb on Ni(111)

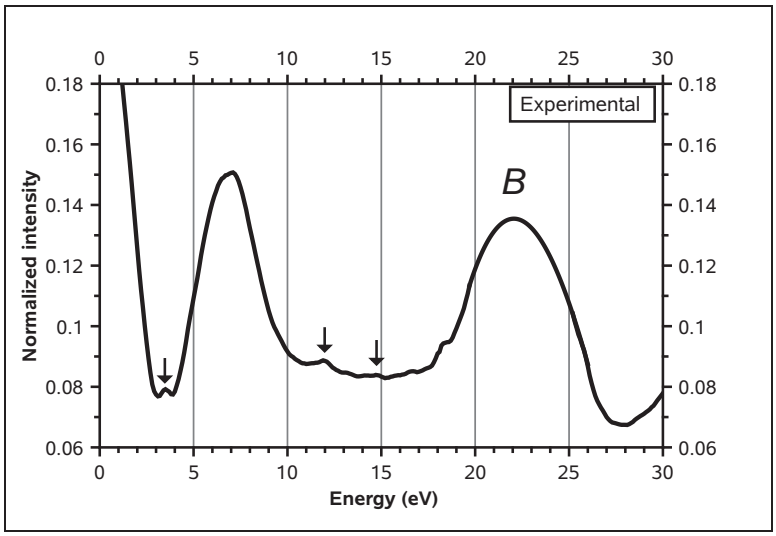

(a)

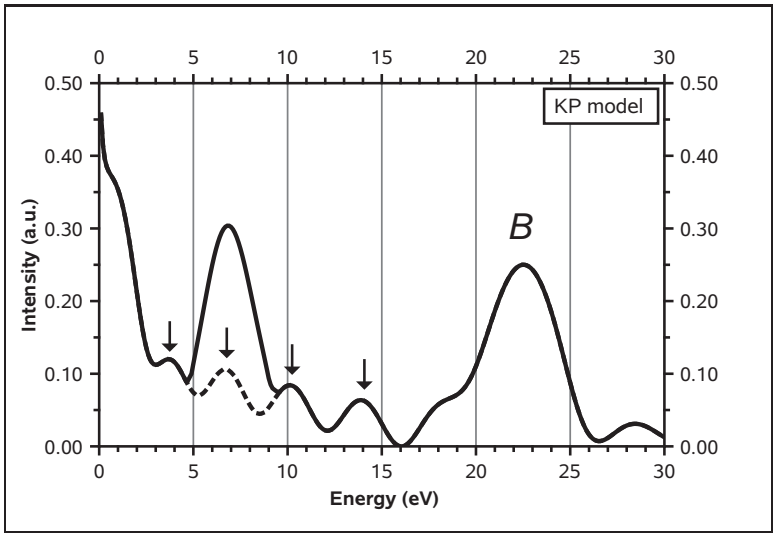

(b)

FIG. 5.8: (a) Measured I/V-LEEM curve for a 5 layer high Pb island on Ni(111) at 474 K, $\theta_{Pb} = 1.25$ ML. (b) Calculated I/V-LEEM curve based on the KP model using the parameters shown in Table 5.2. For the dashed region, addition of a parabola representing the band structure interference peak centered at 7 eV, gives qualitative agreement with the measured curve. The arrows indicate the positions of the $N - 1$ quantum interference peaks.

system are known to the best of our knowledge, the parameters are based on the best fit parameters for a 5 layer high Bi island on Ni(111) used in Chapter 3, see Table 5.2. Using these values, we are able to qualitatively reproduce the experimental I/V-LEEM data, see Fig. 5.8(a) and (b), with the exception of the intense peak at 7 eV. To fit the Bragg peak to the experimental data we use an interlayer distance, $w_a + w_g$, of 3.05 Å. This corresponds to a surface relaxation of almost 7% compared to bulk Pb. Large relaxations for the (four) outermost Pb(111) layers, larger than typically found for other fcc(111) surfaces, are known to dominate at temperatures over $0.5T_m$ [72], where bilayer modulations of the interlayer distance are reported as well [8]. The large surface relaxations found for Pb(111) cause the quantum interference peaks to broaden and thereby reduce their peak height. We show that the positions of the quantum interference peaks at energies of 3.7 eV, 10.2 eV, and 18.1 eV are in qualitative agreement with the experimental I/V-LEEM curve. The intensity ratio between the Bragg peak and the quantum interference peak at 3.7 eV for the KP model is about $\frac{I_{Bragg}}{I_{QSE}} = 10$. The higher ratio for the measured curve may well be explained by the peak broadening, along with the Debye-Waller factor and/or dynamic effects.

The intense peak at 7 eV in Fig. 5.8(a) is attributed to band structure effects. From literature it is known that sharp peaks in the reflectance correlate with band structure crossings and gaps along the ΓL line of the Brillouin zone [73]. Typically for fcc metals these sharp peaks lie near the Γ_2' point, Γ_7^- in double group notation [74]. The position of Γ_2' at 10 eV above E_F [75], correlates with the intense peak at 7 eV after the addition of the inner potential [76] and subtraction of the work function difference between the LaB_6 cathode [77] and thin Pb(111) films [7, 63]. Taking this band structure effect into account, we superimposed a peak at 7.0 eV in the KP model, drawn as a solid line in Fig. 5.8(b) in the energy range 4.6-9.5 eV. This results in qualitative good agreement with the measured I/V-LEEM curve in Fig. 5.8(a). Therefore, we conclude that the weak quantum interference peaks in the I/V-LEEM curve are also dominated by strong band-structure effects around 7 eV.

We have demonstrated a broad variety of mostly circumstantial evidence for the occurrence of QSEs in thin Pb layers on Ni(111). All features show a close resemblance to previous observations obtained for Pb on Cu(111) [65] and even on Si(111) and Ge(111) [3, 71]. Therefore, we can safely conclude that QSEs are present in thin Pb films on Ni(111) and govern the film morphology. As an explanation for the decoupling of the Pb states with the Ni bulk bands we refer to Ref. [67], which reports a workfunction reduction of not less than 0.7 eV for Pb modified Ni(111). This directly results in a clear band gap in the interface projected Ni bulk bands with the Fermi level about 0.5 eV above the band maximum in the Γ point. In this situation we fulfill all requirements for observing QSEs in Pb/Ni(111) as experimentally observed.

5.4 Summary

We have studied the growth and properties of thin Pb films on Ni(111). First, a one layer high wetting layer develops consisting of small (7×7) and (4×4) domains, where the former has a stronger binding to the Ni(111) substrate. This results in the accumulation of tensile lateral stress, forcing the system to relieve this by allowing the growth of compressively stressed (4×4) domains. Since the density in both domains is very similar and their azimuthal orientation is identical, the domain wall energy will be low. These low energy cost domain walls result in small domain sizes.

For coverages $\theta_{Pb/Ni} > 0.55$ ML, Pb mesas form, which are embedded in the wetting layer. We have shown distinct QSE driven preferred heights for the Pb mesas in a number of specific examples for relatively thin and thick films. This is apparent from island height transitions both on wide terraces as well as at substrate steps. The average island heights that evolve during deposition at 422 K and 474 K show a clear signature of QSE driven preferred heights, distinctly including stable heights of 5, 7 and 9 atomic layers.

All features closely resemble previous observations for Pb films on Cu(111) as well as on Si(111) and Ge(111) [3, 65, 71]. The identified QSEs in Pb/Ni(111) are attributed to Pb induced modifications of the Ni(111) interface, leading to a band gap in the interface projected Ni bulk bands.

Weak quantum interference has also been identified in I/V-LEEM measurements. The experimental I/V-LEEM curve is also dominated by strong band structure effects around 7 eV.

Anomalous decay of electronically stabilized Pb mesas on Ni(111)

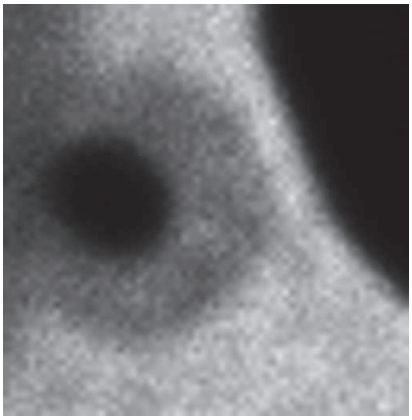

With their low surface free energy, Pb films tend to wet surfaces. However, Quantum Size Effects (QSEs) often lead to islands with distinct preferred heights. We study thin Pb films on Ni(111) using Low Energy Electron Microscopy (LEEM) and selected area Low Energy Electron Diffraction (μLEED). Indeed, the grown Pb mesas show distinct evidence for QSEs. At about 526 K metastable mesas reshape into hemispheres within milliseconds, driven by a huge reduction in interfacial free energy. The underlying diffusion rate is many orders of magnitude faster than expected for Pb on bulk.

6

6.1 Introduction

The substrate-vacuum, the film-vacuum and the film-substrate interface free energies are three main ingredients governing the equilibrium morphology of a film on a crystalline substrate. Following Young's equation the film wets the substrate when the substrate-vacuum free energy is higher than the sum of the film-vacuum and film-substrate free energies. Since their surface free energy is relatively low [78], Pb films have an inherent tendency to wet most substrates. Lattice misfit gives rise to an associated stress energy, building up with increasing film thickness. Beyond a critical thickness the film breaks up even if the interfacial energies predict wetting [79]. This feature is considered of lesser importance for Pb films since its lattice parameter is much larger than those of most metal substrates, which often leads to higher order commensurability or even incommensurability [68].

A usually disregarded contribution to the total free energy originates from quantum size effects (QSEs). QSEs give rise to specific preferred film heights as the result of a characteristic relationship between the Fermi wavelength, λ_F, and the interlayer distance, d [29–31]. With $d \approx 0.75\lambda_F$, Pb is the main representative of this class of materials. Odd layer numbers are preferred initially, later crossing over to even layer numbers [32]. These electronic effects have a profound influence on the film morphology in our LEEM and μLEED investigation of Pb films on Ni(111). In addition to QSEs, extremely fast mass transport in ultrathin Pb films on Si(111) has also been reported. Unanticipated fast expansion of Pb islands on Si(111) and anomalous refilling kinetics of laser induced holes have been attributed to fast collective motion inside the wetting layer [61, 80]. Here we show that ultrafast mass transport is not at all restricted to the wetting layer. Large Pb mesas on Ni(111) decay instantaneously, requiring mass transport rates many orders of magnitude larger than conventional ones for macroscopic Pb substrates [81, 82].

6.2 Results and discussion

Low Energy Electron Diffraction (LEED) has been used to monitor the evolution of the wetting layer during deposition of Pb on Ni(111) at 474 K at a typical rate of about 10^{-3} Pb atoms per unit cell (uc) per second (Pb/uc/s). From a coverage of $\theta_{Pb/Ni} \sim 0.15$ ML onwards, a faint $(\sqrt{3} \times \sqrt{3})$-R30° pattern emerges with its maximum intensity around $\theta_{Pb/Ni} = 0.33$ ML, indicating the formation of a surface alloy [37]. As coverage increases, dealloying and the formation of a Pb wetting layer is observed. An ordered wetting layer covers the entire surface above $\theta_{Pb/Ni} \approx 0.40$ ML and new diffraction peaks emerge at a position corresponding to an in-plane lattice constant of 3.93 Å. From $\theta_{Pb/Ni} \approx 0.40$ ML onwards these Pb-peaks move outward with increasing exposure, indicating compression of the aligned, incommensurable hexagonal Pb layer. The coverage in this layer is de-

termined by the combined result of continuously adding new material from the source and the ongoing dealloying. The latter process accelerates with coverage, as is concluded from the increasing shrinkage of the lattice constant (Fig. 6.1) until it is completed when the continuous compression ends abruptly at an in-plane lattice constant of 3.50 Å. This observation provides an excellent opportunity for an exact in situ calibration of the deposition rate. We obtain 8×10^{-4} Pb/uc/s.

Beyond $\theta_{Pb/Ni} = 0.510$ ML the line profiles in Fig. 6.1 exhibit a surprising peak splitting. It reveals the emergence of two coexisting domains with different in-plane lattice constants: 3.50 Å and 3.32 Å. These lattice parameters originate from (7×7) and (4×4) moiré patterns. Upon increasing the coverage from $\theta_{Pb/Ni} \approx 0.51$ ML to 0.57 ML the main spot intensity moves gradually from the less dense (7×7) domains to the denser (4×4) domains, see bottom panels in Fig. 6.1. This remarkable structure of the wetting layer requires discussion.

The nearest neighbor distance in bulk Pb is 3.50 Å. With the generic tendency for tensile stress at surfaces [69], we suggest that the (7×7) domains involve tensile stress. A slight compression of the Pb-layer is needed to lock-in a commensurate (4×4)-structure. As a measure of the coordination of an individual Pb-atom we take the sum of the lateral components of its position vector, measured along the directions of the 3 nearest Ni atoms underneath, relative to those values for an atom in a hollow site. For an on-top, bridge and, three-fold hollow site we find (expressed in Ni lattice constants): 1.734, 0.444, and 0 respectively. The respective average numbers for the (7×7) and the (4×4) structures are 0.550 and 0.618. This clearly suggests that the coordination is higher and thus the binding stronger for the (7×7) than for the (4×4) structure, in line with the observations. The strong binding to the substrate has a down side in the build-up of compressive lateral stress. The system can only relieve this by keeping the (4×4)-patches small and alternating them with low tensile stress (7×7)-patches. Differently stressed domains give rise to self-assembly [1]; compare e.g. Pb/Cu(111) [50]. Unfortunately, it is impossible to image these domains. This is due to either the small domain sizes, which are below the spatial resolution of the instrument ($\sim$7 nm) and/or too fast fluctuations of the domain boundaries. The energy cost of domain walls is low due to the alignment to the substrate and similar density, leading indeed to narrow domains and fast fluctuations.

Beyond $\theta_{Pb/Ni} \approx 0.55$ ML Pb mesas develop. These mesas are fully relaxed since μLEED only shows the bulk Pb lattice constant. This is in line with the low misfit energy, which allows the continuous compression of the wetting layer. From here onwards we define a monolayer (ML) as the equivalent of a bulk Pb(111) layer. The average height of the growing mesas as a function of the integral coverage, expressed in ML, is shown in Fig. 6.2 for 422 K and 474 K. The average height of the mesas growing at 474 K first increases then flattens out at an island height of 7 layers at a total coverage of 1.5-1.75 ML. At 422 K the average height flattens out at 5 layers high islands at 1.85-1.95 ML. The flat part of the curves reveals that the islands have preferred heights of 5 and 7 layers, but merely expand in a lateral fashion. These preferred heights indicate electronic

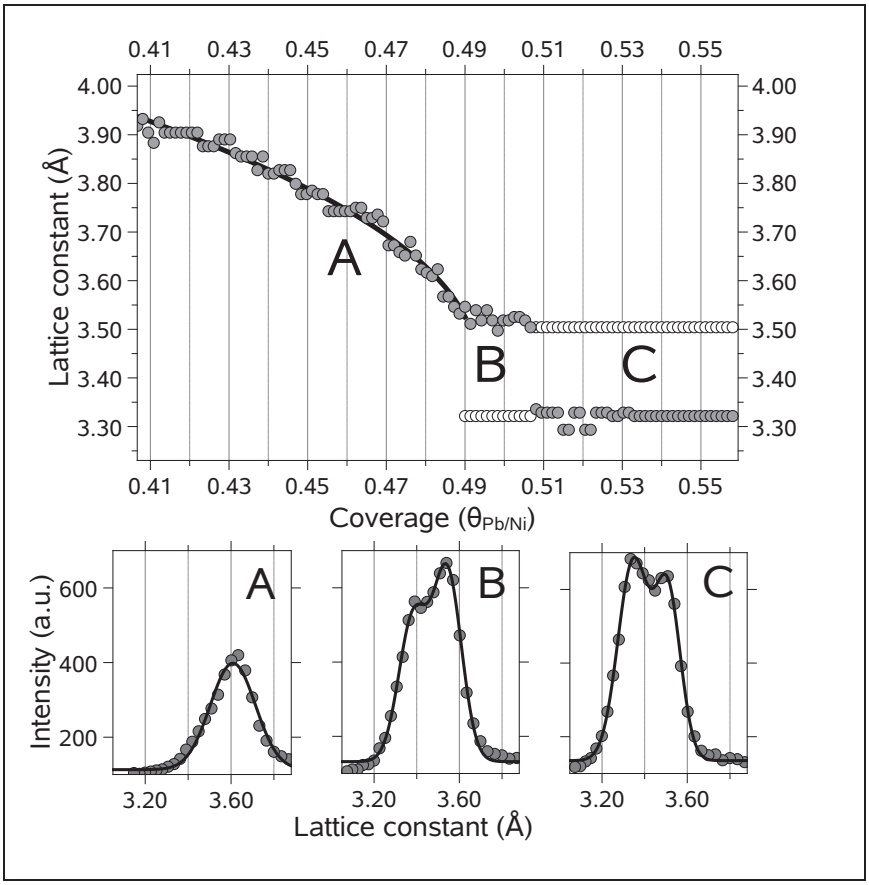

FIG. 6.1: LEED data obtained at 35.0 eV during Pb deposition at 474 K. Upper panel: The in-plane lattice constant, as derived from the position of the Pb(1,0)-peak as a function of coverage. The solid curve serves to guide the eye. Lower panels: Lineprofiles of this peak, taken along the (1,0) direction at the coverage indicated by A, B, and C.

growth for Pb/Ni(111). Thus where the interfacial energies clearly favor wetting and no sizeable misfit related stress energies play a role, we find the evolution of a rough growth front with preferred heights, which can only be attributed to QSEs.

The Pb mesas most likely nucleate on the domain boundaries or on low density domains since adatom diffusion is slower on patches with tensile strain [83]. The progressively growing islands lock-in at these sites, eventually leading to large coalesced Pb mesas that anchor at multiple nucleation sites, see Fig. 6.3. Note that μLEED shows that the wetting layer maintains its double domain structure even after deposition of more than 10 ML Pb. The most eye-catching

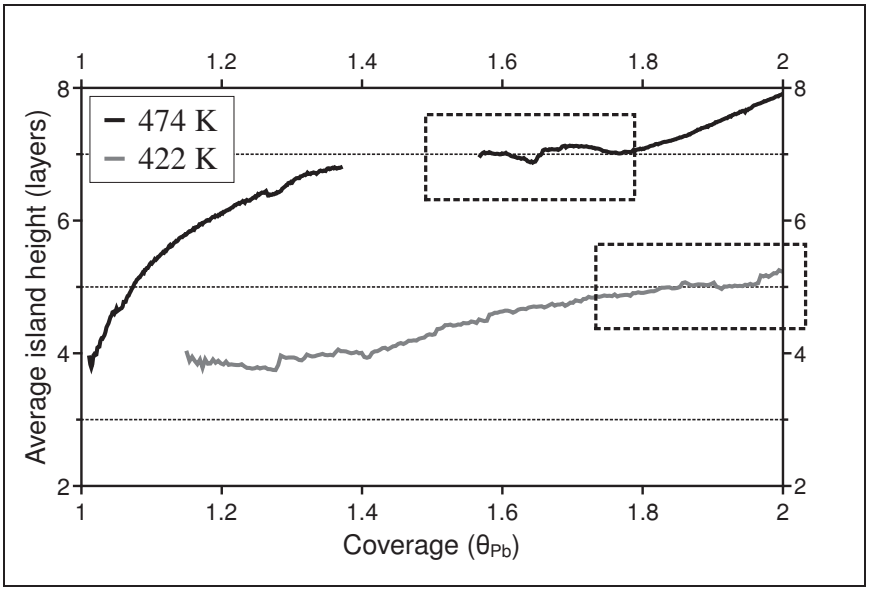

FIG. 6.2: The average island height during growth at 422 K and 474 K as a function of coverage in ML. The dashed boxes indicate situations were the vast majority of the islands attains preferred heights of 5 layers (422 K) and 7 layers (474 K).

observation is illustrated in Fig. 6.3, showing three LEEM images acquired after depositing 12.5 ML of Pb on Ni(111) at 474 K. The left panel shows the surface just after deposition. Subsequently, the sample is heated slowly and the middle and right images have been taken one second apart at 526 K. The grey field represents the wetting layer and the dark features are Pb mesas, which cover 31% of the visible area. The fully relaxed Pb mesas have an *average* height of about 38 layers. The central image was recorded at a critical temperature of 525 K. It shows a large central island with a projected area of about 1.14×10^7 nm^2, which is thus composed of about 4.1×10^9 Pb atoms. The right hand image was taken just one second later. Within less than the image acquisition time (80 ms), the huge Pb mesa collapses into several much smaller ones with an integrated projected area of about 0.6×10^6 nm^2. It thus seems that 3.9×10^9 atoms have disappeared.

This unexpected extremely fast apparent disappearance of more than 10^9 Pb atoms needs an explanation. The straightforward options, dissolution into the bulk or desorption into vacuum, both fail: dissolution into the bulk involves Ni bulk vacancy formation; the corresponding adatoms would yield huge step rearrangements, which are not observed [84] and, respectively, remaining compact ad-structures persist at 525 K on a many orders of magnitude larger time-scale. Indeed, the Ni bulk vacancy diffusion length is estimated at less than 1 lattice

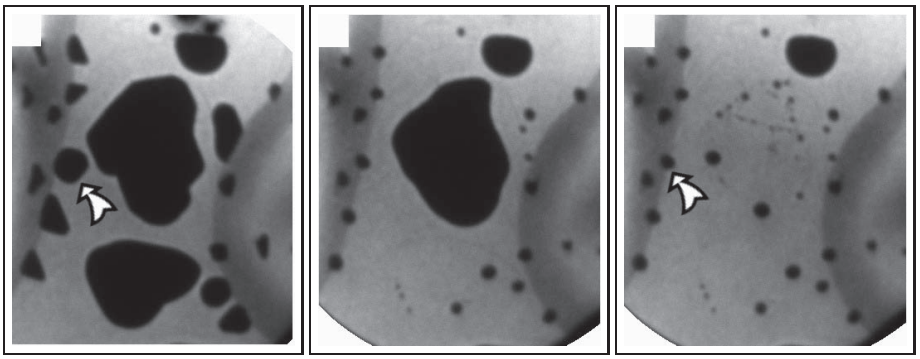

FIG. 6.3: LEEM images (8.4x10.2 μm^2) taken with 20.0 eV primary electrons after deposition of 12.5 ML of Pb at 474 K. The acquisition time for each image is 80 ms. The dark features are Pb mesas and the light grey areas correspond to the wetting layer. The curved features left and right are substrate step-bunches. Fig. 6.3(a) was measured immediately after ceasing the deposition. Figures 6.3(b) and 6.3(c) were measured at 525 K within a time interval of one second, during subsequent slow heating. The white arrows indicate the Pb island displayed in Fig. 6.4(b).

constant within the transition time and the Pb vapor pressure at 525 K is $> 10^6$ times too low to account for the swift disappearance of more than 10^9 Pb atoms. Ostwald ripening is also ruled out since no mass exchange with Pb mesas in the vicinity is observed. Therefore, due to conservation of mass, the spectacular lateral shrinkage of the Pb mesas must be accompanied by a rapid height increase. This leads to an estimated height of a few hundred nanometers and implies that compact 3D structures emerge [85, 86].

Figure 6.4 provides more insight into the mechanism underlying the sudden transition of the mesas into compact 3D-structures. Figure 6.4(a) shows a cartoon exemplifying this transition. A circular disk (mesa) is transformed into a hemisphere based in the center. The latter geometry is inspired by the findings for an equilibrium shaped Pb particle on Cu(111) [86]. This is consistent with Fig. 6.4(b), which is a snapshot from the area centered around the Pb mesa indicated by the white arrow in Fig. 6.3(a). Within the first part of the acquisition of this image (80 ms) the Pb island is still a circular Pb mesa represented by the larger, lighter grey circle. After the collapse, a smaller, darker grey circular feature representing the compact state is seen near the center of the gone mesa. This observation is rare: in less than 5% of the events we could record the transition as it happened. This implies that the transition time is very short indeed. This is further reiterated by the lack of additional contrast within the larger circle. The transition time, τ, is estimated to be only a few milliseconds.

If we assume that the mesa with a diameter, $2 \times r_{2D}$, and a height, h, of 109 Å

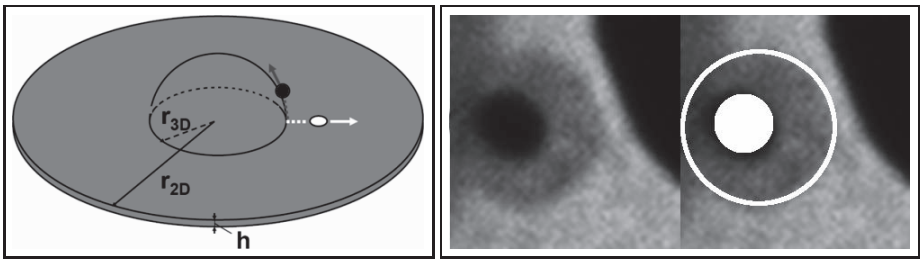

(a) (b)

FIG. 6.4: (a) Cartoon of the shape transition process. Vacancy-adatom pairs are generated thermally at the contact line between the hemisphere and mesa. The mass transfer takes place via radial motion of vacancies (white) to the outer mesa-rim and of adatoms (dark) moving until its accommodation on the hemisphere featuring the compact island. (b) Part of an image (1 μm^2) at 519 K during slow heating with the collapse of a Pb mesa. The Pb island shown in this Fig. is indicated by the white arrow in Fig. 6.3(a) and Fig. 6.3(c). The lighter grey area illustrates the Pb mesa before its collapse, while the darker central area represents the compact island (see text). The circle and disk represent the shapes described in the text.

(38 layers) collapses into a hemisphere with radius r_{3D} (dark grey circle in Fig. 6.4(b)), we can determine the radius of the sphere by using the relation: $r_{3D} = (3h/2)^{1/3} \times r_{2D}^{2/3}$. For the example in Fig. 6.4(b) with $r_{2D} = 3570$ Å, we obtain $r_{3D} = 1280$ Å, which is consistent with Fig. 6.4(b). This finding strongly supports the above assignment for the compact Pb structure.

This finding is highly significant. First of all, the equilibrium shape of an fcc crystal is a truncated octahedron with (111)- and (100)-facets. At elevated temperatures, as is the case here (only 12.5% below the bulk melting temperature), the ridges are rounded and the equilibrium shape of a crystallite quite closely resembles a sphere. Second, and more important, a hemisphere implies a contact angle with the substrate of 90° and therefore at 525 K the surface free energy of the interface between the wetting layer and vacuum and the free energy of the interface between the Pb crystallite and the Ni(111) surface must be (about) identical. Therefore, in considerations of the total interfacial free energy of this system the size of the contact area between the Pb crystallites and Ni(111) can be disregarded.

A comparison of Figs. 6.3(a) and 6.3(c) shows that nearly all other ad-structures underwent a similar shape transition. The large mesa that still persists in the upper region transforms only a few seconds later. Without exception the transitions are almost instantaneous and occur first near pre-existing steps. The decay of the Pb mesas occurring at about 525 K is driven by the gain in total free energy that results from the increased volume-to-surface ratio in the transition from mesas to hemispheres. We can now estimate the gain in surface free energy using the

example of Fig. 6.4(b). Using the measured numbers for r_{2D} (3570 Å) and r_{3D} (1280 Å) we obtain a reduction of the Pb-vacuum interface area of 0.722 μm^2. Using a surface tension 0.272 J/m^2 [87], we obtain a total gain in free energy of 1.23×10^6 eV. This leads to a reasonable energy gain of 6.3 meV/atom. An analysis of the transition of the large central island into several compact ones leads to a similar estimate.

The ultrafast collapse of the Pb mesas involves giant mass transport rates. In the example of Fig. 6.4(b) about 2×10^8 Pb atoms have to assume different positions within milliseconds. For an estimate of the classic mass transfer rate we use the cartoon in Fig. 6.4(a). Note that the nearest neighbor distance, a_{nn} for Pb is 3.50 Å. As a work hypothesis we assume that the mass transfer takes place via the creation of adatom-vacancy pairs at the mesa-hemisphere contact line. The vacancies diffuse towards the mesa-rim and the adatoms diffuse to the top of the hemisphere across ascending steps with an associated effective energy barrier E_{As}. The adatom-vacancy pair formation energy is denoted by E_{VA} and the activation barrier for diffusion of vacancies by E_D. Diffusion is assumed to be strongly biased, resulting in a radial motion of the vacancy from the center towards the outer rim. One then obtains for the transition time τ with activated hopping:

$$\tau \approx \frac{38}{\nu_0} \times \pi[(r_{2D}/a_{nn})^3/3] \times \exp[(E_D + E_{VA} + E_{As})/kT]$$

with $\nu_0 \approx 10^{13}$ s^{-1}; ($r_{3D}^3 \ll r_{2D}^3$). The prefactor (0.004 s) is already of the order of the few milliseconds found experimentally for τ, while the effective ascent energy equals 0.26 eV [30] and the activation energy for vacancy diffusion in Pb(111), E_D, is lower than that for Cu(111) (0.25 eV [87]) and higher than that for Pb adatoms on Pb(111) (80 meV [62]). The inevitable conclusion is that traditional hopping processes are unable to explain the extremely fast mass transport during the decay of the giant islands. The same is true for other scenarios we could think of. Some kind of concerted motion in which the Pb atoms move collectively towards global positions with a lower free energy must take place. Unfortunately, the process is too fast to access with currently available techniques.

The still remaining question is why the double domain structure of the wetting layer disappears at 520-525 K. A conclusive answer cannot be given since no access to the morphological details of the domains is available. However, we stress that the transition of the mesas into hemispheres coincides with the disappearance of the double domain type wetting layer. LEED measurements invariably show a relaxed wetting layer with a single in-plane lattice constant of 3.50 Å after the decay of the mesas. It thus appears that the disappearance of the double domain structure of the wetting layer destabilizes the earlier mentioned lock-in of the large Pb-mesas at anchor sites related to the domain walls.

6.3 Summary

In conclusion, we have found that electronic QSEs are responsible for the initial shape of the rough surface of the Pb films grown on Pb(111). The delicate balance between surface energies, elastic energies and QSEs is initially tilted towards QSEs, as discrete layer heights are observed. When the character of the film gradually changes from 2D to 3D, the balance between these forces becomes more and more dominated by interfacial energies, until it reaches a tipping point. The sudden decay of the electronically stabilized mesas is indeed just that, as the energetic balance is tipped for good in favor of the surface free energy, towards a compact structure. The spectacular speed at which the transition takes place is many orders of magnitude larger than what is expected, based on arguments involving thermally activated behavior. With a widespread interest in nanostructures in general, our results illustrate the generic need to characterize all aspects of nanostructures, both structural and electronic, since small excursions away from equilibrium can have dramatic consequences.

Growth and decay of hcp-like Cu hut shaped structures on W(100)

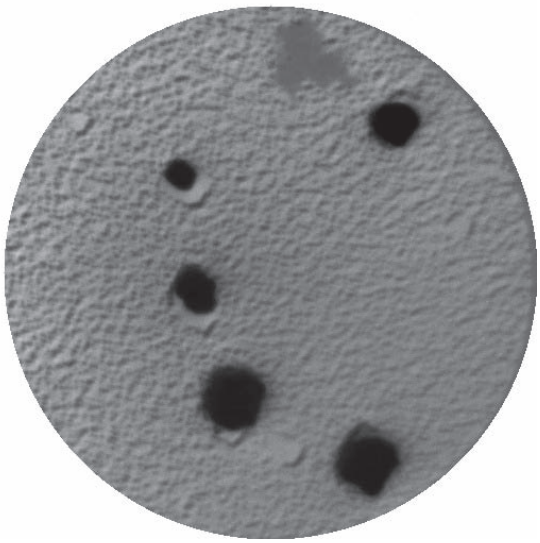

We have studied both the morphology and structure of thin Cu deposits on W(100) during growth and desorption, using Low Energy Electron Microscopy (LEEM) and selective area Low Energy Electron Diffraction (μLEED). During growth at 674 K hut shaped Cu crystallites with steep facets ($> 54^\circ$) coexist with a pseudomorphic Cu monolayer. The μLEED data suggest that these crystallites predominantly have a hcp structure with a high density of stacking faults and the $(11\bar{2}0)$ plane parallel to W(100). The boundaries run along the $[\bar{1}50]$ azimuth on W(100), which is explained by cancellation of shear stress exerted by Cu on the W(100) surface. Upon slow heating, Cu desorbs and the pseudomorphic wetting layer is transformed into coexisting surface alloy patches, with respectively a Cu-rich $p(2 \times 2)$ and $p(2 \times 1)$ structure at 815 K. At about 950 K the islands are fully desorbed, leaving $p(2 \times 1)$ footprints behind. The $p(2 \times 2)$ patches disappear at about 1020 K, resulting in a homogeneous $p(2 \times 1)$ surface. Upon continued Cu desorption this surface transforms into small $c(2 \times 2)$ domains until all Cu has been desorbed at 1150 K.

7.1 Introduction

In thin film growth, the misfit related stress between substrate and adsorbate together with the combined interfacial free energies govern the characteristic Stranski-Krastanov or Volmer-Weber type growth modes. Strong film-substrate interaction in combination with a large misfit will lead to accumulation of misfit induced strain energy. The system usually responds by growing in a Stranski-Krastanov mode with relatively strain-free 3D deposits. Examples are the (hut shaped) clusters with specific facet crystallography and alignment with respect to the substrate, e.g. Ge on the Si(001) substrate which results in clusters that consist of four-sided pyramids with (four equivalent) facets [88]. With increasing distance to the interface, stress can be relieved efficiently [89].

For adsorbates having different crystal structures that energetically slightly deviate from their equilibrium crystal structure, the growth can be further complicated. Noble metals like Cu, with its equilibrium fcc structure, can be grown in its near equilibrium hcp or bcc structure [90], depending on the substrate properties. It has been shown that on bcc (100) substrates, coexisting hcp and bcc structures, or solely hcp structures can be formed, depending on the ratio of the atomic radii of substrate and adsorbate and its bonding to the substrate [91, 92]. With their ratio near one, e.g. Pd [91] and Co [93] show growth of coexisting hcp and bcc structures on W(100). For Cu on W(100), this ratio is slightly lower, resulting in hcp(11$\bar{2}$0) structures for coverages over 2.5 ML [94].

The growth of a few layers of Cu on W(100) has been studied in detail [95–97]. For sub-monolayer coverages a number of ordered surface structures are found to be in dynamic equilibrium at 800 K. These correspond to areas of pseudomorphic Cu, as well as of surface alloys with a $p(2 \times 1)$, $p(2 \times 2)$ and $c(2 \times 2)$ structure [95, 96]. Having a smaller atomic radius, the Cu atoms increase the tensile surface stress of the surface alloys [98]. Studies of the transition to, and growth of hcp structures, as well as their morphology at temperatures over 500 K, is rather limited [91, 94].

Here, we present a study on the growth, decay and interrelationship of Cu structures grown on W(100) at temperatures ranging from 674 K to 1150 K. By using in situ LEEM and μLEED we are able to probe the properties and ordering of both the first Cu layer as well as the growth of 3D islands.

This Chapter is organized as follows. We describe the experimental conditions in Sec. 7.2. In Sec. 7.3, we describe the formation of the first Cu layer along with the morphology of the Cu islands that form. In Sec. 7.4 we discuss the structure of the islands, followed in Sec. 7.5 by their growth dynamics. The decay of the Cu islands at elevated temperatures is described in Sec. 7.6, and the structural changes of the wetting layer at these temperatures in Sec. 7.7. We summarize our conclusions in Sec. 7.8.

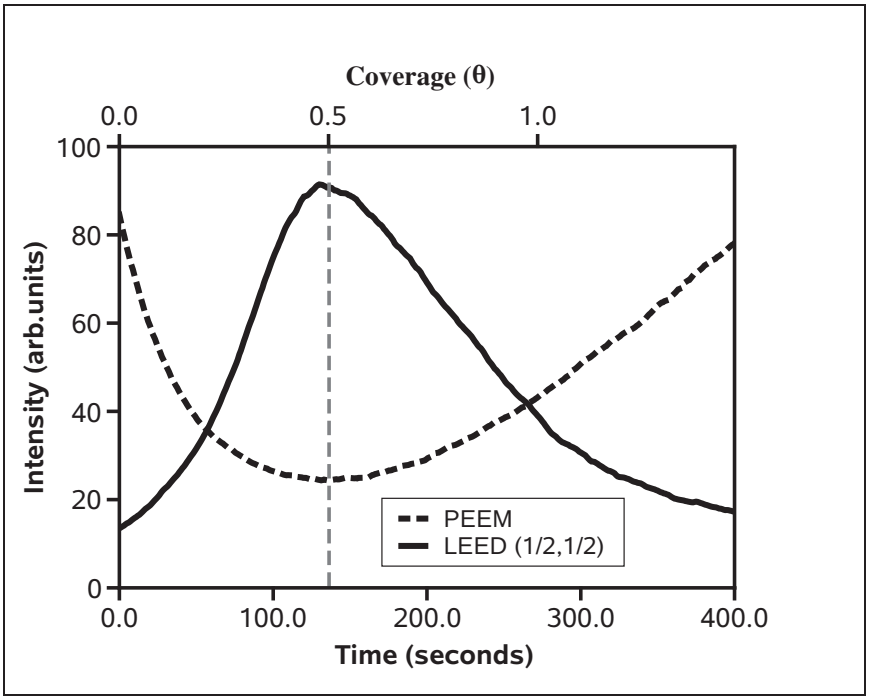

FIG. 7.1: Intensity of the c(2×2) μLEED spot (solid line) measured at 31.0 eV at a temperature of 674 K. The integrated PEEM intensity (dashed line) measured at a temperature of 674 K, shows a minimum at $\theta = 0.5$ ML.

7.2 Experimental

The experiments were performed in an Elmitec LEEM III instrument with a lateral resolution of 7 nm. A W(100) single crystal was cleaned by successive flashing in a background of O_2, monitored by Thermal Desorption Spectroscopy (TDS). Special care has been taken concerning the cleaning by using two-step-flashing as described in Chapter 2 and elsewhere [27]. The procedure was completed by sputtering cycles of 1 keV Ar^+ bombardment at RT followed by flash annealing. During cleaning, C contamination was observed, with a characteristic c(2×2) and p(5×1) LEED pattern [25]. The cleanliness of the sample was verified by Auger Electron Spectroscopy (AES) and LEEM. Copper was deposited from a Knudsen cell.

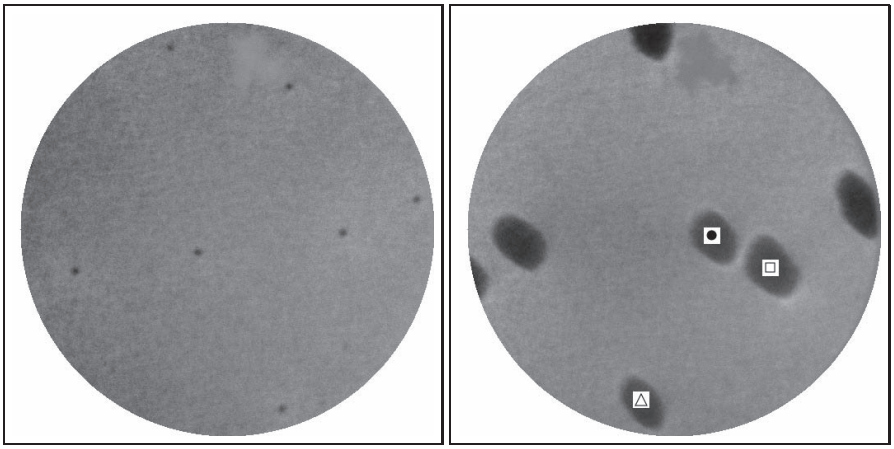

(a) (b)

FIG. 7.2: (a) and (b) LEEM images of Cu islands (dark) on a Cu wetting layer at a coverage of $\theta = 1.5$ ML (a) and $\theta = 38.2$ ML (b). The fractional area of Cu islands is small, 0.1% for (a) and 7.9% for (b), revealing strong 3D growth. Both images have a FoV=10 μm, electron energy 8.0 eV, T=673 K.

7.3 Morphology

We monitor the growth of Cu using LEED at a temperature of 674 K. Shortly after deposition has started, c(2×2) LEED spots appear. This structure can be a simple adlayer, as well as a surface alloy having identical coverage [95–97]. Using the maximum peak intensity for the $(\frac{1}{2}, \frac{1}{2})$ diffraction peak, a precise in situ calibration of the coverage can be made, see Fig. 7.1. For the c(2×2) structure $\theta = 0.5$ ML, where $\theta = 1$ ML corresponds to 1 Cu atom per W(100) surface atom. The measured deposition rate is 3.7×10^{-3} ML/s. The corresponding threshold Photo-Emission Electron Microscopy (PEEM) intensity is a measure for the change in work function during deposition. The minimum in PEEM intensity as shown in Fig. 7.1, corresponds to a maximum in the work function. This is in agreement with Cu atoms in a simple c(2×2) adlayer, similar to growth at RT [96].

Completion of the first monolayer of Cu, results in a pseudomorphic wetting layer, as is verified by LEED. The nucleation of islands is lagging slightly behind and only observed after deposition of about 1.35 ML. Note that, for small island sizes below $\theta = 1.5$ ML, the island sizes are hard to detect due to their small size and the finite lateral resolution of our instrument. The total fractional area of the islands only slowly extends to about 8% at a coverage of $\theta = 38.2$ ML, see Fig. 7.2. Therefore, we conclude that the growth of these islands has a strong 3D character, which we attribute to misfit related stress. The island nucleation

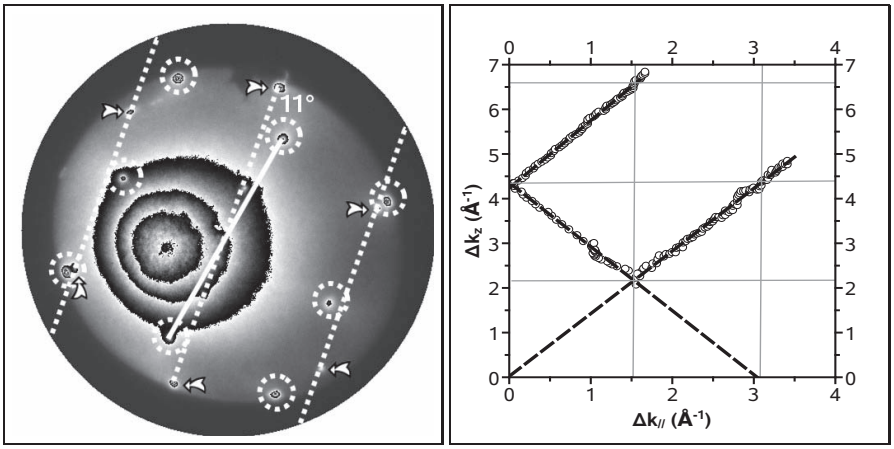

(a) (b)

FIG. 7.3: (a) μLEED pattern of a Cu island measured at 32.5 eV. The LEED peaks for W(100), and thus the pseudomorphic layer, are marked by dashed circles. The arrows mark the (6) facet peaks. The Cu island structure is azimuthally rotated by 11°. (b) A plot of the diffraction facet peak positions in reciprocal space. From the slope of these straight lines we obtain facet angles of $54^\circ \pm 3^\circ$.

is delayed and it requires about 35% of a monolayer to initiate the growth of the 3D structures. A similar supersaturation has been observed for the nucleation of nanocrystals in Al(110) homoepitaxy [99]. The absence of any clear change of slope in the PEEM intensity near the monolayer coverage supports the continuous build up of a diluted, supersaturated phase on top of the Cu wetting layer.

Literature shows some discussion on the wetting layer: the pseudomorphic growth is reported up to a coverage of 2 ML, after which hcp-like island growth is observed [94]. The fractional area of the islands below $\theta = 2$ ML, is however well below the sensitivity of Reflection High-Energy Electron Diffraction (RHEED). Our I/V-LEEM measurements show no indication for a double $p(1 \times 1)$ Cu layer. Apparently, the $p(1 \times 1)$ layer is only energetically favored up to the first layer, which is strongly bound to the substrate.

7.4 Cu hcp-like hut shaped structures

μLEED with a 1.4 μm aperture was used for the structural characterization of the Cu islands shown in Fig. 7.2. For island areas only slightly smaller than the size of the used aperture, the μLEED pattern shown in Fig. 7.3(a) is observed. The peaks originating from the W(100) substrate and thus the $p(1 \times 1)$ Cu layer are indicated by dashed circles. In addition, the pattern shows a number of ad-

ditional intense peaks marked by arrows, which at first sight do not correspond to a distinct pattern. This implies that no clearly developed two-dimensional order is present on top of the Cu islands. Measuring the I/V-μLEED curve on a Cu island, reveals that the additional spots move along the dashed lines in Fig. 7.3(a). Therefore, they represent facet spots arising from strong 3D growth. It is remarkable that the travel of these intense peaks does not coincide with a low index direction on W(100). Its actual azimuthal direction makes an angle of about 11° with the close packed orientation. The rate of motion as a function of electron energy reveals that steep facets are present on the Cu crystallites [100]. A plot of the positions of the diffraction peaks in reciprocal space, i.e. in the ($\Delta k_{//}$,Δk_z) plane, confirms this: the peak positions follow straight lines as is shown in Fig. 7.3(b). From the slopes of these lines we measure facet angles of 54° $\pm$ 3°. The variation of the peak positions in the ($\Delta k_{//}$,Δk_z) plane, also provides information on the perpendicular and in-plane periodicities. For the periodicity along the normal (Δk_z) we obtain 4.42 Å^{-1}, which corresponds to an interlayer spacing of 1.42 $\pm$ 0.01 Å. The periodicity of 1.55 Å^{-1}, found for the in-plane direction ($\Delta k_{//}$) in Fig. 7.3(b), corresponds to a real space periodicity of 4.05 $\pm$ 0.12 Å.

We will now discuss how these findings can be rationalized in terms of the structure of the Cu islands. As a guide we take the hcp structure reported in Ref. [94]. The authors concluded from their RHEED measurements, that in the Cu deposits, the hcp(11$\bar{2}$0) planes run parallel to the W(100) surface. The [1$\bar{1}$00] base vector of the almost square unit cell of the hcp(11$\bar{2}$0) planes fits perfectly along the [110] azimuth of W(100) with a misfit of only -1.1%. The perpendicular [0001] base vector has a misfit of +7.3% along the [1$\bar{1}$0] azimuth of W(100). It is also known from experiments that the close packed facets are easy glide planes giving rise to twinning in fcc crystals. For Cu/W(100), a high density faults in the stacking order perpendicular to the close packed planes has been observed previously [101].

First, we consider the interlayer distance between the Cu planes parallel to W(100). The measured value could hint at either fcc Cu(011), bcc Cu(001) or hcp Cu(11$\bar{2}$0). Since we do not see clear options for either fcc or bcc Cu in terms of a low misfit registry with respect to W(100)-c(2×2), we resort to the hcp structure. The corresponding interlayer distance would be 1.28 Å. The Cu crystallite would therefore be expanded along the [11$\bar{2}$0] direction by about 10%. The combination with the compression of about 7.3% along the [0001] direction of hcp Cu leads to the conclusion that indeed the stress in the hcp Cu crystallite remains low. We note that, similar to the Ge/Si(001) huts the relaxation in higher planes can be very effective [89]. A peculiarity is the fact that the contact lines of the facets with the substrate are not parallel to the $\langle 100 \rangle$ directions of W(100), but rather intersect W(100) at an angle of about 11° with the $\langle 100 \rangle$ azimuth, see also Fig. 7.3(a). This finding can be rationalized by the fact that the square (11$\bar{2}$0) unit cell contains two atoms: one in the fourfold hollow site on W(100) and one on the center line along the W(100)-$\langle 110 \rangle$ azimuth, situated at either $\frac{1}{3}$ or $\frac{2}{3}$ of the unit cell boundary, see Fig. 7.4. This will lead to shear stress along the $\langle 100 \rangle$ exerted

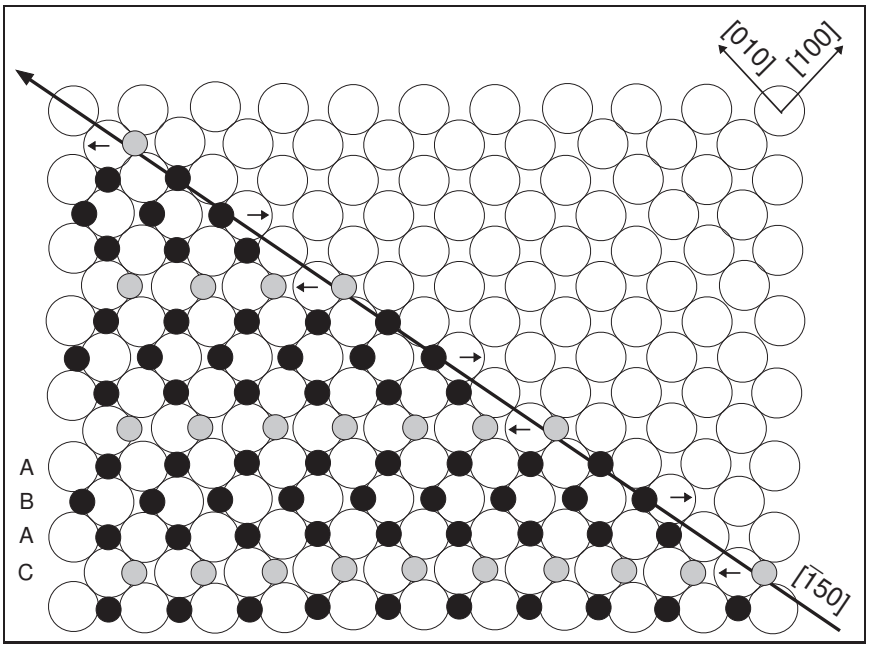

FIG. 7.4: Cartoon of the first layer of Cu atoms in the Cu crystallites (small circles) on the W(100) surface (large open circles). The pseudomorphic wetting layer, not shown for clarity, would consist of Cu atoms in four-fold hollow sites on the right hand side of the black line along the W(100)-[$\bar{1}$50] azimuth. The latter shows the boundary between the crystallite and the wetting layer and makes an angle of 11.3° with the W(100)-[010] azimuth. The Cu atoms are drawn with the hcp crystal (11$\bar{2}$0) plane as a base. The grey small circles represent a fault in the perfect AB-stacking sequence, shown by black circles. The cartoon shows an $(ABAC)_n$-stacking of the close packed layers. The arrows indicate the direction of the exerted stress on the outermost W(100) layer by the Cu directly above. The [$\bar{1}$50] azimuth warrants a complete cancellation of the shear stress, indicated by arrows, along the W(100)-[1$\bar{1}$0] azimuth.

by Cu on the W(100) surface. This stress can be significantly reduced if we allow for stacking faults. For the ideal case of an $(ABAC)_n$-stacking the shear stresses are cancelled and we arrive at a strong candidate for a boundary between Cu and W along the [$\bar{1}$50] azimuth, see Fig. 7.4. It makes an angle of 11.3° with [010] on W(100), in agreement with the experimental observation in Fig. 7.3(a). Also the steep facets can be easily realized: from the hcp (11$\bar{2}$0) structure and the 10% expanded interlayer distance, we obtain a facet angle of about 54°. This leads to quite smooth facets, and also explains the absence of a regular diffraction pattern since no extended areas with (11$\bar{2}$0) orientation are expected on top of the hut shaped Cu crystallites.

In addition, we mention that the average separation of the atoms along the

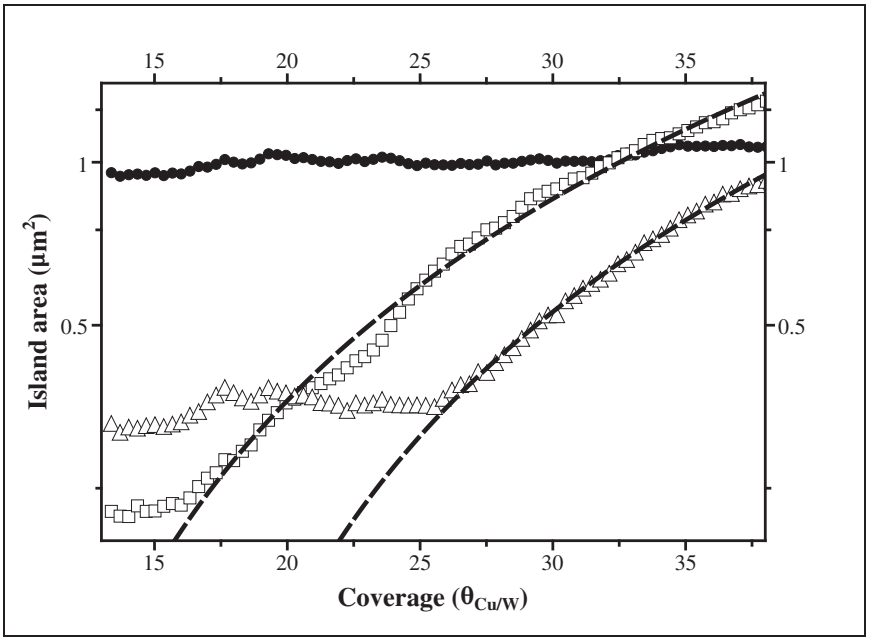

FIG. 7.5: Measured island area for increasing coverage for the islands (within the FoV during a slight drift) labeled with •, △ and □, according to Fig. 7.2. The dashed lines show the best fit to $f \times a^p$, with $p = \frac{3}{2}$ and where a is the actual area of the island. See text for more details.

[$\bar{1}$50] azimuth, and therefore the periodicity, is 4.03 Å, i.e. very close to the experimental result of 4.05 Å. The compression of the Cu along the W(100)-[110] direction may also still lead to grains which are oriented in the [001] direction. The grain boundaries are probably light and their appearance, in line with previous reports [101], would explain why the Cu islands are quite compact.

7.5 Growth dynamics

As can been seen from Fig. 7.2, the hcp-like Cu island area only slowly increases during deposition. After the deposition of $\theta \approx 45$ ML the hcp-like Cu islands have a fractional coverage of 9.1%, resulting in an *average* island height of about 700 Å. We measured the area of the three marked islands of Fig. 7.2(b) as a function of global coverage, as is shown in the semi-log plot in Fig. 7.5. We can study the growth dynamics where the available material for the hut structure is $\alpha(\theta - \theta_0)$, where α is the number of atoms that has landed in the capture zone during the increase of the global coverage from θ_0 at the nucleation of the island, to the actual value θ. For 3D growth, this has to equal $f \times a^p$, where a is the

actual island area. The prefactor f and exponent p both depend on the exact geometrical shape. Two dimensional growth would e.g. result in $p = 1$, spherical growth in $p = \frac{3}{2}$. In Fig. 7.5 the best fit (dashed lines) represent $p = \frac{3}{2}$, from which we conclude that the island grows in three dimensions.

Figure 7.5 shows some other interesting features. First of all the island denoted by •, hardly grows with time. Its size remains constant at a projected area of about 1 μm^2. The island denoted with $\triangle$ nucleated quite early, then stopped expanding for quite some time and continued its growth at a global coverage of about 25 ML. Its further growth follows the functional dependence given above. We conclude from the behavior of the growth rates, that the local environment plays an important role.

7.6 Cu island decay

Increasing the temperature to about 1000 K leads to the decay of the hcp-like Cu structures, as is shown in Fig. 7.6(a-d). The island fractional area, dark in Fig. 7.6, decreases until the islands have completely disappeared at time t_f, leaving a footprint that is discussed further below.

The decay of the islands is characterized by measuring the effective island radius r as a function of time at a constant temperature of 1015 K, assuming almost circular shaped islands. Using the classical continuum theory in its general form [102] we can describe the time evolution of the cluster sizes using $r \propto \tau^{\gamma}$, where the decay time is defined as $\tau = t_f - t$, with t the actual time. The exponent γ is characteristic for the mass transport limiting conditions. This description was demonstrated to be valid for e.g. single layer high Ag island decay on Ag(111) [103], where the diffusion limited kinetics lead to $\gamma \approx \frac{1}{3}$, similar to Ostwald ripening. From the log-log plot of the normalized r versus the decay time shown in Fig. 7.7, we derive $\gamma = \frac{1}{2}$, shown by the dashed line. This exponent implies that island decay can be viewed as thermal desorption of Cu from the entire island surface into vacuum [102]. Although there is considerable scatter in the experimental values for gamma, the value of $\gamma = \frac{1}{3}$ is definitely outside the error margins. We can not exclude some deviations from the ideal behavior in terms of interaction with the 2D diluted phase, but think that the direct desorption into vacuum is the dominant process.

7.7 Wetting layer desorption

When the decay of the hcp-like Cu islands is completed, the islands leave a footprint, see Fig. 7.6(b-d) and Fig. 7.8(a). Characterization of this footprint by μLEED in the position indicated by the dashed circle in Fig. 7.8(a) shows two orthogonal orientations of p(2×1) ordering, shown in Fig. 7.8(b). Such a structure indicates a surface coverage of $\theta = 0.5$ ML.

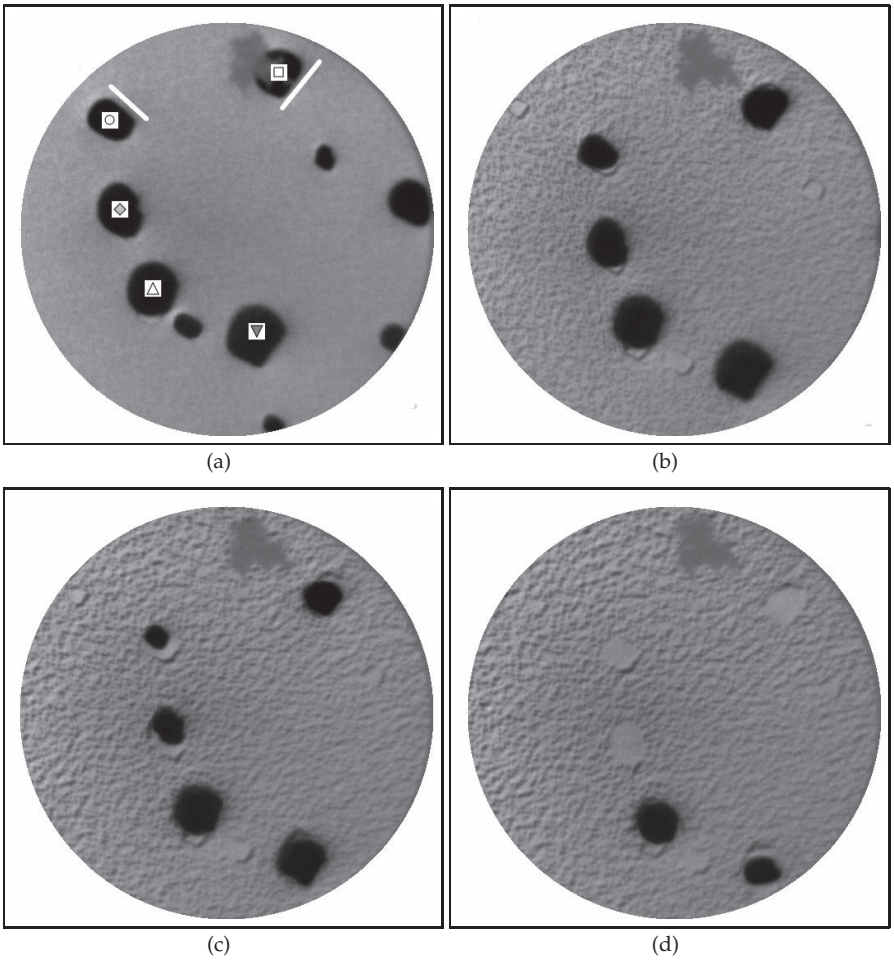

FIG. 7.6: (a) LEEM images of hcp-like Cu islands surrounded by a single p(1×1) Cu layer at a coverage of $\theta = 46.2$ ML. (b-d) At a temperature of 950 K the islands start decaying, leaving a footprint. Temperatures are 950 K (a), 1000 K (b) and 1015 K (c,d). All images have FoV=10 μm, electron energy 8.0 eV.

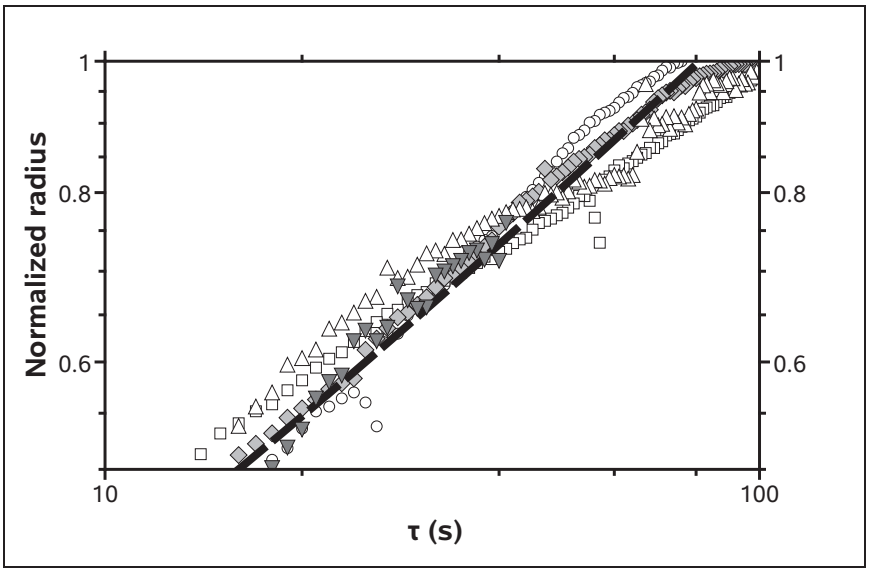

FIG. 7.7: Normalized island radius versus decay time τ in a log-log plot. Labels for the experimental data are according to island labeling in Fig. 7.6(a). The dashed line represents $r \propto \tau^{1/2}$.

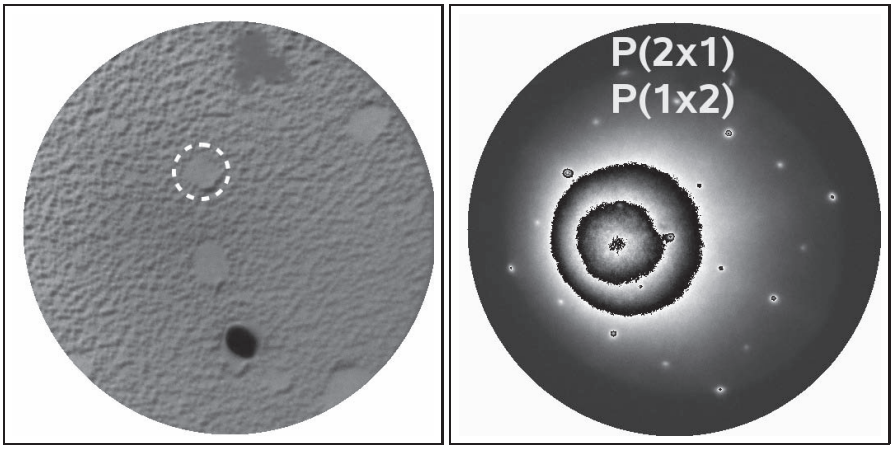

(a) (b)

FIG. 7.8: (a) LEEM image of the surface after the decay of the hcp-like Cu structures. FoV=10 μm, electron energy 8.0 eV, T=1000 K. (b) The footprints show p(2×1) ordering in the μLEED image taken at the dashed circle position in (a). Electron energy 31.0 eV, T=1000 K.

FIG. 7.9: (a) μLEED image taken at 31.0 eV and (b) LEEM image for the p(1×1) Cu layer found for 674 K$< T <$815 K, FoV=10 μm, electron energy is 8.0 eV. (c) μLEED image for the p(2×2) structure and a p(2×1) structure found for 815 K$< T <$1020 K, electron energy is 31.0 eV. (d) the corresponding LEEM image shows small domains of p(2×2) and p(2×1) surface alloys, FoV=2μm, electron energy is 8.0 eV. (e) μLEED image for a p(2×1) domain created at T=1020 K, electron energy is 31.0 eV. (f) A composite image constructed of dark field images from the $(\frac{1}{2}, 0)$ and $(0, \frac{1}{2})$ diffraction spots, revealing the domains of the p(2×1) and p(1×2) structures. Image size is 6.8×6.8 μm^2. (g) μLEED image of the diffuse c(2×2) surface alloy diffraction pattern at T=1075 K, electron energy is 31.0 eV. The integrated spot intensity, see Fig. 7.10, is measured in the area marked by the small white square. (h) The corresponding LEEM image, FoV=10μm, electron energy is 8.0 eV.

At a temperature of about 815 K, well below the temperature where hcp-like Cu island decay sets in, the wetting layer surrounding the island shows a transition. Before this transition, the wetting layer shows $p(1 \times 1)$ ordering, as is shown in Fig. 7.9(a). The corresponding LEEM image shows no contrast, see Fig. 7.9(b). When the wetting layer is imaged after the transition in more detail, see Fig. 7.9(d), we find that it consists of small domains that have contrast that is identical to what is found in the footprints. μLEED reveals a $p(2 \times 2)$ pattern, shown in Fig. 7.9(c). It is the result of the coexistence of small $p(2 \times 2)$ and $p(2 \times 1)$ domains, where the latter is the more stable one. The observed structures and corresponding temperatures are in agreement with literature where the $p(2 \times 2)$ structure is attributed to a Cu rich surface alloy with one W atom and three Cu atoms in its unit cell [96]. We must conclude that a local variation in coverage results in a reduction of the Cu coverage through thermal desorption from $\theta = 1$ ML, via $\theta = 0.75$ ML ($p(2 \times 2)$) to $\theta = 0.5$ ML ($p(2 \times 1)$). Temperature Programmed Desorption (TPD) measurements show thermal desorption at 1100 K for coverages $\theta < 1$ ML [95, 96]. Note that the time scales used are radically different. Here we deal with a typical time scale of 900 s, while the heating rate in the TPD literature data vary between 4 and 130 K/s. The surface alloying that is revealed by the appearance of the $p(2 \times 2)$ pattern, is confirmed by a corresponding increase in the W(1,0) diffraction spot intensity of about 25% between 800-900 K. The increase results from the alloying in which more W atoms become visible in the outermost layer. Their larger atomic scattering factor, in comparison to Cu, gives rise to enhanced intensity in the integral order spots.

For temperatures above 1000 K we find that the small and dark Cu-rich $p(2 \times 2)$ patches disappear and we loose contrast on the surface in our bright field images. This is indicative of the desorption of Cu from the ordered Cu-rich patches. We are left with the $p(2 \times 1)$ patches and the total coverage decreases to a value of $\theta = 0.5$ ML, shown in the μLEED pattern in Fig. 7.9(e). By measuring the corresponding dark-field images on the $(0, \frac{1}{2})$ and $(\frac{1}{2}, 0)$ spots we are able to image both rotations of the $p(2 \times 1)$ domains, clearly segregated. Combining these images results in the composite image shown in Fig. 7.9(f).

Upon reaching a coverage of $\theta = 0.5$ ML, we anticipated to observe $c(2 \times 2)$ ordering, as known from literature [96]. This structure has been reported to be stable up to thermal desorption at 1100 K [96]. However, the different route of formation via a Cu-rich phase leads to the $p(2 \times 1)$ domain. Only at T=1075 K do we find a diffuse $c(2 \times 2)$ diffraction pattern, as is shown in Fig. 7.9(g), where the corresponding LEEM image in Fig. 7.9(h) reveals no contrast. The broad $(\frac{1}{2}, \frac{1}{2})$ diffraction peaks indicate small $c(2 \times 2)$ and probably defect rich surface alloy structures [96].

This remarkable structural ordering towards complete thermal desorption is followed in situ with LEED and illustrated in Fig. 7.10. The spot intensities for the $(\frac{1}{2}, \frac{1}{2})$, $(\frac{1}{2}, 0)$ and $(0, \frac{1}{2})$ spot during heating of the sample at a linear rate of 2.64 K/s is depicted. The intensity in the $(\frac{1}{2}, \frac{1}{2})$ diffraction spot corresponds to

both p(2×2) and c(2×2) structures, where the intensity in the $(\frac{1}{2},0)$ spot corresponds to both p(2×2) and p(2×1) ordering. Unlike earlier reports in literature [96], the $(\frac{1}{2},0)$ diffraction peak of the p(2×2) structure does not show attenuation before the $(\frac{1}{2},\frac{1}{2})$ peak does. At T=985 K the $(\frac{1}{2},\frac{1}{2})$ spot intensity shows a maximum, revealing the onset of the transition of p(2×2) domains into p(2×1) domains by thermal desorption. The p(2×1) shows its maximum diffraction intensity at T=1010 K as a sharp peak where the $(0,\frac{1}{2})$ spot intensity does not, since no intensity of the p(1×2) domains contributes to the $(\frac{1}{2},0)$ diffraction spot at this temperature. At a temperature of 1075 K, we find broad diffuse intensity at the $(\frac{1}{2},\frac{1}{2})$ diffraction spot, corresponding to small c(2×2) domains. From these findings we suggest that at a coverage of $\theta = 0.5$ ML, both the p(2×1) and c(2×2) surface alloy structures are stable, where the first occurs as the result of desorption from a Cu-rich coverage of $\theta > 0.5$ ML. Apparently the energy barrier for the transition from the p(2×1) structure into the more favorable c(2×2) structure is almost similar to the desorption energy. The energy barrier from the (meta)stable p(2×1) structure towards the more stable c(2×2) surface alloy can only be overcome at temperatures where desorption occurs simultaneously. Probably, desorption induced vacancies which are known to enhance diffusion [104], are necessary to lower the effective energy barrier, which has to be passed to form the c(2×2) phase. Therefore, a diminishing coverage is left to create small c(2×2) domains for T $>$ 1020 K, resulting in the corresponding broad diffraction peaks. For temperatures over 1150 K, no signature of any Cu surface structure was measured.

7.8 Summary

Using LEEM and μLEED we studied the morphology and structure of thin Cu layers on W(100). During deposition at 674 K, we observe strong 3D growth of hut shaped Cu crystallites having steep facets. Using μLEED we found no clear long range ordering, suggesting these crystallites predominantly have a hcp structure with the $(11\bar{2}0)$ plane parallel to W(100), and a high density of stacking faults. From the measured facet diffraction spots, we obtain facet angles of about 54°. The boundary between the facets and the W(100) face with the pseudomorphic Cu wetting layer is found experimentally to cross the close packed W azimuth directions at an angle of 11°. This is attributed to a perfect cancellation of the shear stress exerted by the hcp Cu crystallite on the underlying W(100) along the $[1\bar{1}0]$ direction when choosing an $(ABAC)_n$ stacking sequence. This leads to a $[\bar{1}50]$ boundary orientation, intersecting the W(100)-$[1\bar{1}0]$ azimuth at 11.3°.

Upon slow heating, the pseudomorphic Cu layer transforms into a surface alloy at 815 K. This surface shows small coexisting domains of Cu-rich p(2×2) and p(2×1) ordering. Increasing the temperature to 950 K results in the

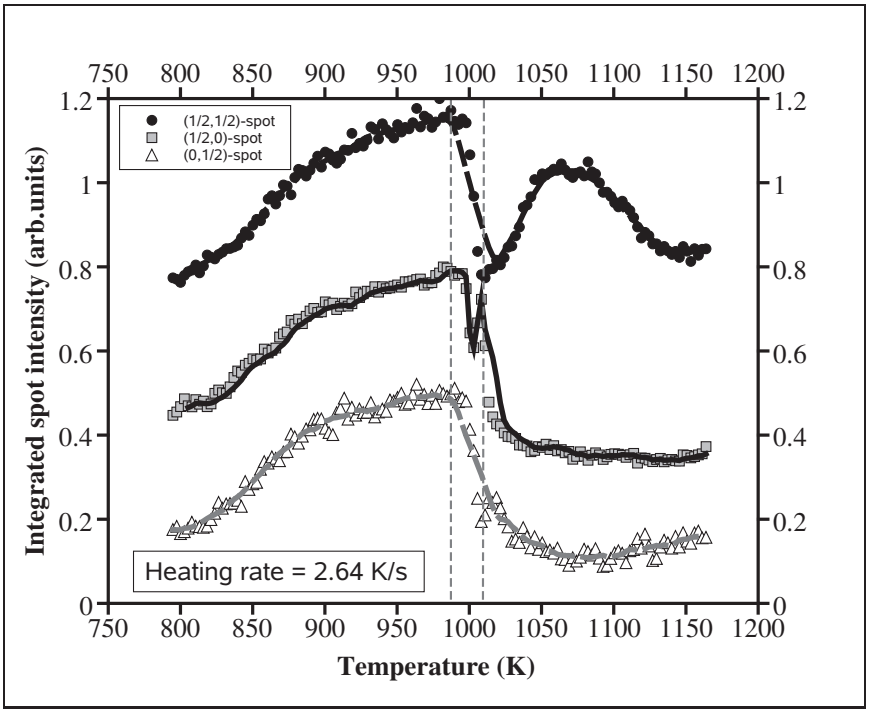

FIG. 7.10: The integrated spot intensities for the $(\frac{1}{2}, \frac{1}{2})$, $(\frac{1}{2}, 0)$ and $(0, \frac{1}{2})$ diffraction spots (offset) as a function of temperature. The lines at T=985 K and T=1010 K show the maximum integrated intensity for the $(\frac{1}{2}, \frac{1}{2})$, $(\frac{1}{2}, 0)$ and $(0, \frac{1}{2})$ LEED spots measured with a 1.4 μm aperture. The aperture size is smaller than the typical domain size, see Fig. 7.9(e), hence only one of the two possible orientations is visible.

decay of the hut shaped structures. From the island decay we derive a radial decay rate proportional to $\tau^{1/2}$, indicating desorption into vacuum. The hcp-like islands leave footprints that show $p(2 \times 1)$ ordering. The $p(2 \times 1)$ domains grow in lateral size, further desorbing Cu down to a coverage of $\theta = 0.5$ ML. This surface alloy shows remarkable thermal stability. Only slightly before complete desorption, small $c(2 \times 2)$ domains are found.

Temperature calibration

A

In the experimental setup the temperature is measured using a type C thermocouple with a reference junction positioned at the back of the sample. The thermocouple is spot-welded right underneath the sample. To calibrate the reading of the thermocouple, we make use of atomic steps flowing uphill during sublimation at a stationary situation representative for the entire surface. This retraction of steps is observed in a temperature range above 1150 K for Ni(111) with a velocity of the order of 100 nm/s. Since this process is relatively slow it is to be expected to take place with surface defects very close to equilibrium. Uphill flow of steps will be caused by the creation of adatoms to the terraces followed by their sublimation. The energy for this process is equal to the cohesive energy of 4.45 eV for Ni. To be absolutely correct we need to correct for thermal contributions to the free energy difference with the vapor phase. This, being less than tenths of eV's, falls within the error bar of our measurements.

Figure A.1(a) and (b) shows steps on Ni(111) taken during sublimation. Sublimation causes the steps to flow uphill as time proceeds. In this specific Fig. the steps flow about 2.8 μm in 25.888 seconds. This distance is measured using a screw dislocation as a marker on the surface, assuming the immobility of it relative to the Ni substrate. This eliminates temporal drift.

When combining the equation for the dimensionless diffusivity D

$$D = C \times exp(-E/k_B T) \tag{A.1}$$

where C is a constant, E the activation energy, k_B the Boltzmann constant and T the temperature; with a (in first assumption) linear relation between the real temperature T (293.2 K) and the corresponding thermocouple readout T_{th} at the same time (257.6 K)

$$T = A \times T_{th} + B \tag{A.2}$$

with A and B constants, we are able to express B in terms of A:

$$B = 293.2 - A \times 257.6 \tag{A.3}$$

Now we are able to rewrite equation A.1 as:

$$ln(D) = ln(C) - \frac{E}{k_B(A \times T_{th} + 293.2 - 257.6 \times A)} \tag{A.4}$$

When measuring the diffusivity at three different temperatures we can make a least-squares fit using the cohesive energy, taken to be constant in the measured temperature window, as the activation energy for this process (see Fig. A.1(c)). From this we can calculate the real temperature (T) using the relation:

$$T = (1.002 \pm 0.04) \times T_{th} + (34.9 \pm 1.4) \tag{A.5}$$

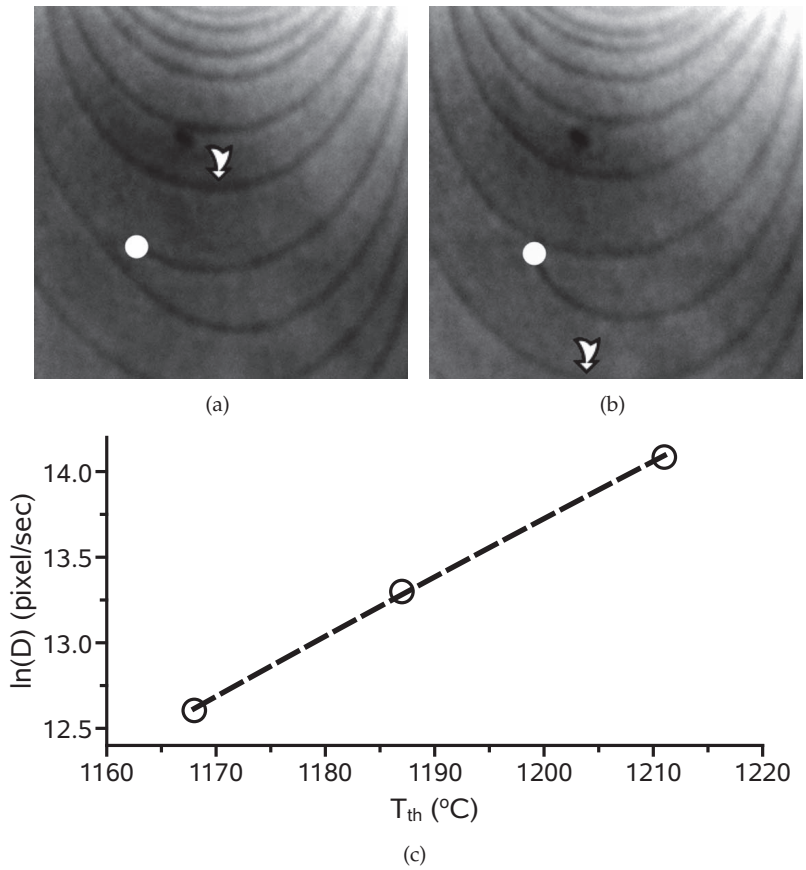

FIG. A.1: (a) and (b) Uphill step flow from sublimation at 1206 K on Ni(111). Images taken 25.888 seconds apart (arrows indicate current position). FoV=5.4 $\times$ 5.4 μm^2, electron energy 1.5 eV. A screw dislocation is used as a marker. (c) Plot of $ln(D)$ versus thermocouple temperature with the least-squares fit.

Therefore, by making use of the atomic steps flowing uphill during sublimation we are able to accurately calibrate the temperature reading with an error within 5%.

Tensor LEED

B

Low Energy Electron Diffraction (LEED) is a well established and powerfull technique to determine the detailed surface structure of crystalline materials: the measured diffraction pattern can be used qualitatively. The spot positions in the pattern give information on the periodicity and rotational alignment of the surface structure with respect to the bulk, or ultrathin film with respect to the substrate. LEED can be also used in a quantitative manner by measuring the spot intensities as a function of incident electron energy, so called I/V-LEED curves. We are then able to obtain information on the atomic species and atomic coordinates on the surface as well. For the comparison of experimental I/V-LEED curves with theoretical calculations, see Chapter 3. we used dynamical LEED theory. This approach allows an accurate determination of the geometrical structure (and chemical composition) of the top layers of a 2D periodic surface slab and an underlying bulk crystal. The computation was done using the Erlangen Tensor LEED package `TensErLEED` designed by Blum and Heinz [40]. The package provides an efficient computer code in which standard methods such as the muffin-tin approach and the layer stacking method are used. For the calculation of the phaseshifts we used the `EEASiSSS` package designed by Rundgren [41] which calculates the real part of the inner potential $V_0(E)$ as well. In general, in the energy range for 0 to 600 eV, the $V_0(E)$ curve is well approximated by an analytical expression

$$V_0(E) = max\left[c_0, \frac{c_1}{\sqrt{E + c_2}}\right] \tag{B.1}$$

with parameters $c_0 < 0$, $c_1 < 0$ and c_2. The constant c_0 closely approximates the ground-state interstitial potential.

For a comparison between calculation and experimentally obtained results one should be aware of the angular dependence of I/V-LEED curves, see e.g. [19]. In LEEM the incident beam is perpendicular to the surface, as is never the case for a conventional LEED setup. The quality of the fit is then expressed by the Pendry R-factor (R_P) which emphasizes positions of maxima and minima rather than their heights. In general, $R_P < 0.2$ is considered as good, where $R_P \simeq 0.3$ are considered mediocre.

In Fig. B.1 we show the result of a Tensor LEED calculation for the specular beam in comparison to the experimental results obtained for Ni(111) after background subtraction at a temperature of 474 K. This substrate shows no surface reconstruction and its surface relaxation is limited to within 1.2% [105]. Since the calculations were restricted to a simplified bulk geometrical structure not taking into account any relaxations, and since no fitting was performed, the Pendry R-factors quantifying the comparison are relatively high. Besides that, we have to note that for higher energies the S/N-ratio of the I/V-μLEED measurement, as

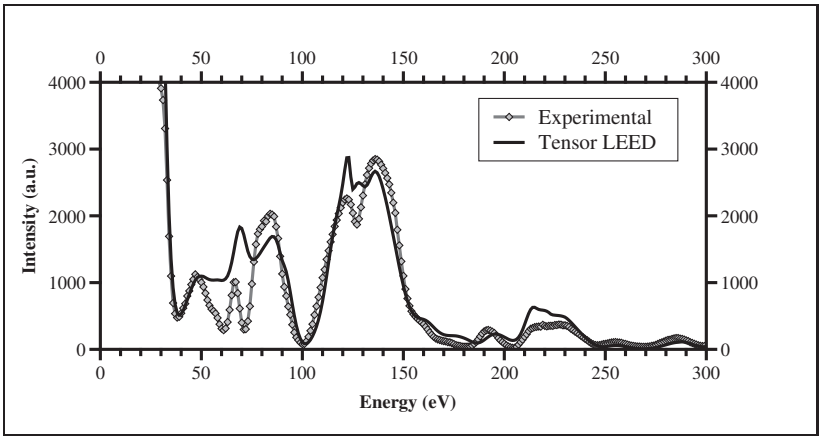

FIG. B.1: A comparison of a Tensor LEED calculation for the Ni(111) specular beam to the experimental result using an illumination aperture of 1.4 μm at 474 K. The resulting $R_P = 0.13$ concludes the fit to be of a good quality.

used in our applications, is limited by the available intensity using the smallest illumination aperture. The Pendry R-factor can be minimized through a Debye-Waller factor, resulting in $R_P = 0.13$, which can be considered a good result. The minimization results in a surface Debye temperature of about 160 K which is only slightly lower than experimentally obtained using LEED [106]. This reduced value can be explained by the larger vibrational amplitudes of surface atoms compared to bulk atoms. This holds in particular for the perpendicular component of the vibrational amplitudes of the surface atoms, which are probed extensively in the specular beam.

A full structure determination of a particular system requires an extensive set of data including intensities of a multitude of diffraction peaks, taken over a wide energy range. Since we are interested mainly in obtaining information on the interlayer spacing we make use of the intensity variation of the specular beam, since this peak contains the required information most directly. As already mentioned, the S/N-ratio of the higher diffraction orders is limited by the available intensity when using the smallest illumination aperture. The latter is also severely reducing the availability of the higher energy data for the specular beam, due to Debye-Waller effects. In spite of these uncertainties complicated by the limited reliability of the used electron-matter interaction potential at very low energies, good semi-quantitative information was obtained, in fact the only possible one in our instrument.

Image processing

C

Data acquisition and storage

LEEM is an imaging technique capable of high resolution, video rate imaging of surfaces. To record the backscattered electrons coming from the surface through the imaging column, a microchannel plate (MCP) detector is used. This component detects the impinging electrons and intensifies the signal by multiplication of electrons via secondary emission. The channel plates are imaged using a high performance 12 bit CCD camera. The exposure time of the camera can range from 1 ms up to 1000 seconds. A fiber optic link connects the camera to the computer. There the data is stored in a 12 bit 512×512 array of pixel values. To create a screenshot of the data, the array is converted to 8 bit.

To keep up with the amount of data captured by the camera, the data is stored as a binary file. Since binary data is directly stored from memory to disk (and vice versa) it has fast access times, limited only by the disk access time. Converting the raw data to an image, means loss of information due to the conversion from 12 to 8 bits for visual interpretation in 256 grayscale values.

Through the use of (normal) contrast stretching we optimize the contrast by stretching the intensity range of the raw data to span the available grayscale values. When the lowest and highest values are unrepresentative for scaling we can use a fraction of the histogram or define a cutoff fraction in it, thereby preventing outliers from affecting the scaling too much.

Drift correction in the frequency domain

A common problem in many microscopy techniques is drift of the imaged sample. When attempting long measurements (e.g. measuring a sample for many hours, which is quite common in LEEM experiments) this drift can be severe. To compensate for this drift we make use of a fast image cross-correlation (XC) technique which we use for post-acquisition drift compensation. This method is a computational one. Other methods in e.g. Scanning Tunneling Microscopy (STM) or Atomic Force Microscopy (AFM) are instrumentation based solutions [107, 108]. In our method we assume a series of images, with constant image size and resolution, can have only lateral (not rotational) drift. This assumption is valid in the case of a proper alignment so that the image geometry is orthogonal. A simple XC can be used to find the best alignment, represented by the maximum of the 2D XC, between successive images and therefore the drift. The deviation of this maximum represents the drift in integer pixels between two images.

The real XC $C(x,y)$ for two images $a_{n-1}(i,j)$ and $a_n(i,j)$, can be calculated from a comparison of two subsets of each image at multiple offsets (x and y) given by the equation:

$$C(x,y) = \frac{\Sigma_i \Sigma_j (a_{n-1}(i+x, j+y) a_n(i,j))}{\sqrt{(\Sigma_i \Sigma_j a_{n-1}(i+x, j+y)^2)(\Sigma_i \Sigma_j a_n(i,j)^2)}} \tag{C.1}$$

While this approach gives the desired XC it is, especially for larger images, computationally demanding. The available search window is limited by the subset images and therefore it limits the maximum detectable shift from the origin. By doubling the size of the search window one squares the amount of calculations of equation C.1. Making use of the Discrete Fourier Theorem (DFT) we can calculate the XC of the entire image in the frequency domain with significant less computations. We make use of the FFTW subroutine library [109]. In this case the XC can be calculated using the equation:

$$C(x,y) = \mathcal{F}^{-1}[\mathcal{F}(a_{n-1}(i,j))\mathcal{F}(a_n^*(i,j))] \tag{C.2}$$

where $\mathcal{F}^{-1}$ denotes the inverse Fourier transform operator using the complex conjugate of the Fourier domain image $a_n^*(i,j)$. To rule out any influence from borders we could set them to zero using (e.g.) a Hanning window. This would improve the resolution in the frequency spectrum, but since we use larger images, windowing is not needed as long as we find a single, clearly distinguishable maximum. In the case of smaller window sizes we find an incorrect response in agreement with [110] which can be corrected by using a Hanning window.

The major drawback of calculating the XC in Fourier space is its inability to measure drift less than 1 pixel for successive images. The additive error propagation can therefore lead to drifts that are incorrectable. We tested this using a series of images with a 2D Gaussian that drifted with constant fractional diagonal velocity. When we perform the drift correction method as discussed before, we are unable to track this drift.

To be able to correct for fractional drift velocities with no impact on the computational load we implemented the key frame technique [110]. A key frame is an image with a frame number $(n+1)$ that is a multiple of the key frame interval k. The concept of key frames is that successive images are correlated, with the expectation that every key frame is correlated with the previous key frame. E.g. $k = 5$ would compare frame 2 to 1, 3 to 2, 4 to 3, 5 to 4, 6 to 1 and then 7 to 6, etc. $k = 1$ equals sequential XC as described in equation C.2. It can be seen that the perfect key frame interval is the inverse of the fractional velocity, since that number of frames gives a propagation of exactly one pixel drift. By setting k too low or too high we are not able to track the drift accurately, see Fig. C.1. We can improve this by monitoring an average velocity to adjust k during the drift correction process. The velocity is measured in both orthogonal directions. The

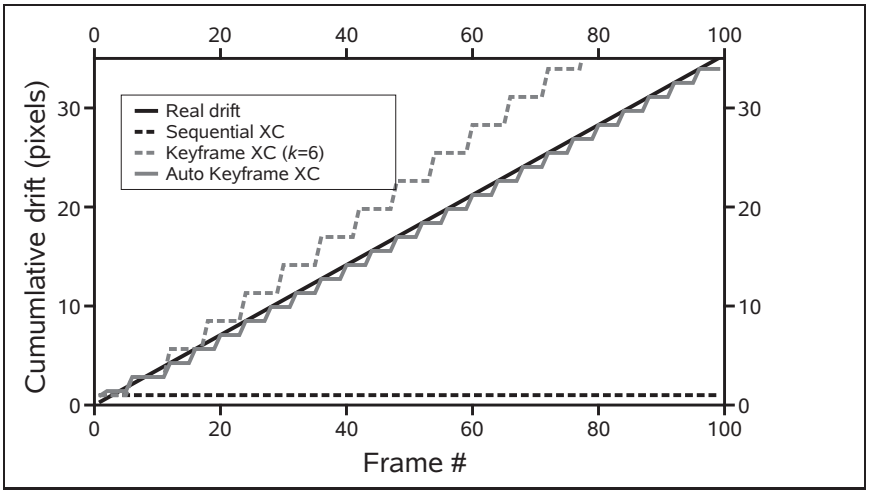

FIG. C.1: Fractional drift velocity ($v_x = v_y = 0.25$ pixel/frame) can not be tracked by the sequential XC method. Using a key frame we are able to track the drift more accurately. Monitoring the average velocity enables adjustment of the key frame interval, see curve labeled auto keyframe, to converge to the inverse of the fractional velocity thereby accurately tracking the drift.

lowest velocity is used since it is the limiting one to add to exactly one pixel drift. Using successive images to XC instead of correlating with the image at the initial time step allows us to correct drift even when the image differs significantly from the one at the initial time step.

Noise supression by filtering in the spatial domain

To extract and quantify the relevant information from the data, we used several filtering techniques. The goal of the filters is to suppress noise. All of these filters are well-known filters and can be found in any textbook on image processing [111], therefore only a brief description of their operation is given in the following sections. The reliability of the procedures has been proven for STM and AFM images [112].

Erosion, dilation and median

The erosion, dilation, median and Kuwahara filters calculate a new value for every pixel on the basis of the surrounding pixels. In the case of erosion (dilation) the new pixel value equals the minimum (maximum) pixel value of this 3×3 pixel region. Applying this type of filter therefore shrinks (grows) islands. Repetitive use of the filter equals using it with a larger matrix of surrounding

pixels. After many calls to this filter we can end up with square like structures caused by the shape of this filter technique. This filter is also used in STM imaging to restore the image from the dilation-like tip convolution.

The median filter uses the median value of the matrix, thereby removing outlying pixel values skewing the statistical quantities. This filter is very CPU-intensive. Its speed was improved by implementing the QuickSelect algorithm [113, 114].

Kuwahara

Smoothing the image by replacing the matrix with the median or average value smears out the steps. By using the more advanced Kuwahara filter, we can suppress the noise on the terraces to make them flat, but also keep the steps as sharp as possible. It uses a 5×5 pixel environment in which four sub-environments of 3×3 pixels are defined for which the average and standard deviation are calculated. The pixel value is then replaced by the average value of the sub-environment with the smallest standard deviation, corresponding to the value of the nearest 'flat' region.

Background subtraction

By subtracting a reference measurement for every image we can correct for defects in the MCPs as well as (part of) the illumination gradient. The reference measurement is obtained by defocussing the objective to project a homogeneously illuminated image onto the MCPs.

Image segmentation

To probe the properties of objects in which we are interested, it is useful to separate these objects from the background. Thresholding provides an easy and convenient way to do this. In particular, thresholding has been applied to measure the properties of the individual Pb and Bi mesas on Ni(111), described in Chapters 3, 5 and 6, as well as for the hut shaped Cu islands grown on W(100) described in Chapter 7.

Thresholding

By thresholding, every pixel value is compared to an intensity threshold in a single pass. If the pixel intensity is higher than the threshold, the pixel value is set to zero in the output. Otherwise it is set to 1. To accurately segment foreground and background, the histogram should show a distinct peak for the foreground objects such that the intensity value can be chosen to isolate this peak. In the histogram the peak for the background and foreground can easily overlay as a

result of illumination gradients across the image. In that case, reasonable results can only be achieved by using adaptive thresholding.

Adaptive thresholding

Whereas the conventional thresholding uses a global threshold for all pixels, adaptive thresholding changes the threshold dynamically over the image. Thereby it can correct for illumination gradients across the image [115]. For finding the optimal local threshold value we can use e.g. the mean, median or the mean of the minimum and maximum value in the immediate vicinity of the pixel, depending on the image. The size chosen for this immediate vicinity, the window, should cover sufficient foreground and background pixels, but should not be too large to violate the assumption that smaller regions of the image are more likely to have approximately uniform illumination. In our LEEM measurements we typically used windows of 10-20% of the FoV.

Otsu's method

To automatically pick the optimal threshold value based on the histogram shape we make use of Otsu's method. This method separates all pixels into two classes (objects and background) by a threshold intensity. The optimum threshold can be obtained by maximizing the separability of the histogram and thus minimizing the intra-class variance, defined as a weighted sum of variances of the two classes. Otsu shows that minimizing the intra-class variance is the same as maximizing the inter-class variance [70]. This approach performs well in situations where there is little contrast between background and object so that the histogram can be modelled as two overlapping Gaussian curves with little separation. Combining the Otsu method with adaptive thresholding gives good results for the detection of the objects in our images, see Fig. C.2(c), as is easily verified by plotting contours. The sensitivity to window size variation was evaluated by examining the effect on segmentation as described in Ref. [116].

Processing binary images

After image segmentation the binary images are processed using erosion and dilation filters. By using a threshold on the feature size, induced noise is removed. By labeling the objects we are able to track properties like e.g. projected area and perimeter of a particular island as a function of coverage over many frames. Examples are shown in Chapters 3, 5 and 7.

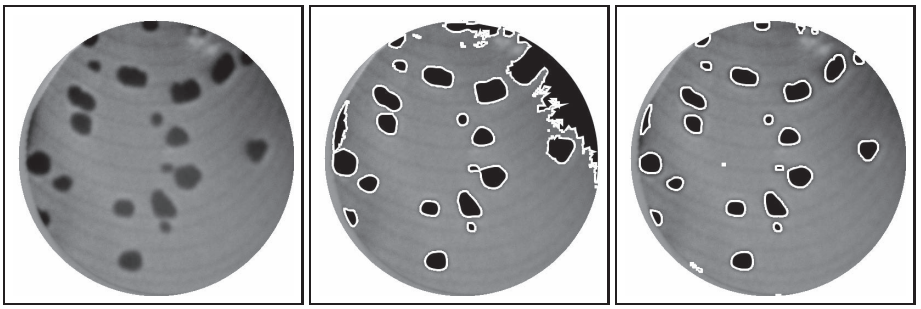

(a) (b) (c)

FIG. C.2: (a) Background subtracted LEEM image of small Pb islands on Ni(111), T=422 K, FoV=4μm, electron energy 20.0 eV. (b) Using a single threshold value for the entire image results in inaccurately measured sizes as a result of the illumination gradient. Islands in the upper part of the image are e.g. overestimated. (c) Combining the Otsu method with adaptive thresholding gives good results.

References

[1] V. Marchenko, JETP Lett. **33**, 381 (1981).

[2] R. Plass, N. C. Bartelt, and G. L. Kellogg, J. Phys.: Condens. Matter **14**, 4227 (2002).

[3] M. M. Özer *et al.*, Phys. Rev. B **72**, 113409 (2005).

[4] M. Jałochowski, H. Knoppe, G. Lilienkamp, and E. Bauer, Phys. Rev. B **46**, 4693 (1992).

[5] Y. Jia *et al.*, Phys. Rev. Lett. **105**, 066101 (2010).

[6] B. Wu and Z. Zhang, Phys. Rev. B **77**, 035410 (2008).

[7] Y. Qi *et al.*, Appl. Phys. Lett. **90**, 013109 (2007).

[8] A. Mans, J. H. Dil, A. R. H. F. Ettema, and H. H. Weitering, Phys. Rev. B **72**, 155442 (2005).

[9] Y. Guo *et al.*, Science **306**, 1915 (2004).

[10] M. M. Özer, J. R. Thompson, and H. H. Weitering, Phys. Rev. B **74**, 235427 (2006).

[11] T. L. Chan *et al.*, Phys. Rev. Lett. **96**, 226102 (2006).

[12] Y.-S. Fu *et al.*, Phys. Rev. Lett. **99**, 256601 (2007).

[13] M. M. Özer *et al.*, Science **316**, 1594 (2007).

[14] E. Bauer, Surf. Sci. **299/300**, 102 (1994).

[15] E. Bauer, Surf. Rev. Lett. **5**, 1275 (1998).

[16] R. M. Tromp, IBM J. Res. Dev. **44**, 503 (2000).

[17] R. M. Tromp *et al.*, Ultramicroscopy **110**, 852 (2010).

[18] W. Telieps and E. Bauer, Surface Science **200**, 512 (1988).

[19] M. K. Debe and D. A. King, J. Phys. C Solid State **15**, 2257 (1982).

[20] M. S. Altman, W. F. Chung, and C. H. Liu, Surf. Rev. Lett. **5**, 1129 (1998).

[21] E. Bauer, J. Phys.: Condens. Matter **13**, 11391 (2001).

[22] E. Bauer, J. Electron Spectrosc. Relat. Phenom. **114-116**, 975 (2001).

[23] A. M. Horgan and I. Dalins, J. Vac. Sci. Technol. **10**, 523 (1973).

[24] M. Ondrejcek, M. Rajappan, W. Swiech, and C. P. Flynn, Phys. Rev. B **73**, 035418 (2006).

[25] D. S. Choi and D. H. Kim, Mod. Phys. Lett. B **23**, 835 (2009).

[26] E. Bauer and T. Engel, Surf. Sci. **71**, 695 (1978).

[27] K. Zakeri *et al.*, Surf. Sci. **604**, L1 (2010).

[28] S. Yaginuma *et al.*, J. Phys. Soc. Jpn. **77**, 014701 (2008).

[29] Z. Zhang, Q. Niu, and C. K. Shih, Phys. Rev. Lett. **80**, 5381 (1998).

[30] K. Budde, E. Abram, V. Yeh, and M. C. Tringides, Phys. Rev. B **61**, R10602 (2000).

[31] M. Hupalo and M. Tringides, Phys. Rev. B **65**, 115406 (2002).

[32] M. M. Özer, C. Z. Wang, Z. Zhang, and H. H. Weitering, J. Low Temp. Phys. **157**, 221 (2009).

[33] N. W. Ashcroft and D. N. Mermin, *Solid State Physics*, 1 ed. (Thomson Learning, Toronto, 1976).

[34] T. Hirahara *et al.*, Phys. Rev. B **75**, 035422 (2007).

[35] K. Gürtler and K. Jacobi, Surf. Sci. **152/153**, 272 (1985).

[36] K. Umezawa *et al.*, Surf. Sci. **365**, 118 (1996).

[37] K. Umezawa *et al.*, Phys. Rev. B **56**, 10585 (1997).

[38] D. Brown *et al.*, Phys. Rev. B **61**, 7706 (2000).

[39] T. Nagao, T. Doi, T. Sekiguchi, and S. Hasegawa, Jap. J. Appl. Phys. **39**, 4567 (2000).

[40] V. Blum and K. Heinz, Comput. Phys. Commun. **134**, 392 (2001).

[41] J. Rundgren, Phys. Rev. B **68**, 125405 (2003).

[42] J. Sun, J. B. Hannon, G. L. Kellogg, and K. Pohl, Phys. Rev. B **76**, 205414 (2007).

[43] K. Heinz, private communication (Bene Poelsema) (unpublished).

[44] Y. Cui, Q. Wei, H. Park, and C. Lieber, Science **293**, 1289 (2001).

[45] S. Evoy *et al.*, Microelectron. Eng. **75**, 31 (2004).

[46] A. Li, F. Liu, and M. G. Lagally, Phys. Rev. Lett. **85**, 1922 (2000).

[47] H. J. W. Zandvliet and R. van Gastel, Phys. Rev. Lett. **99**, 136103 (2007).

[48] J. Tersoff and R. M. Tromp, Phys. Rev. Lett. **70**, 2782 (1993).

[49] B. J. Hinch, C. Koziol, J. P. Toennies, and G. Zhang, Europhys. Lett. **10**, 341 (1989).

[50] R. van Gastel, R. Plass, N. C. Bartelt, and G. L. Kellogg, Phys. Rev. Lett. **91**, 055503 (2003).

[51] S. Yaginuma *et al.*, J. Phys. Soc. Jpn. **77**, 014701 (2008).

[52] T. Nagao *et al.*, Phys. Rev. Lett. **93**, 105501 (2004).

[53] P. Nash, J. of Phase Equilib. **6**, 345 (1985).

[54] P. Feschotte and J.-M. Rosset, J. Less Common Met. **143**, 31 (1988).

[55] G. P. Vassilev, X. J. Liu, and K. Ishida, J. Phase Equilib. Diffus. **26**, 161 (2005).

[56] S.-K. Seo, M. G. Cho, and H. M. Lee, J. Electron. Mater. **36**, 1536 (2007).

[57] L. K. Verheij, B. Poelsema, and G. Comsa, Surf. Sci. **162**, 858 (1985).

[58] S. M. Binz, M. Hupalo, and M. C. Tringides, J. Appl. Phys. **105**, 094307 (2009).

[59] K. L. Man, Z. Q. Qiu, and M. S. Altman, Phys. Rev. B **81**, 045426 (2010).

[60] M. Li *et al.*, Phys. Rev. B **79**, 113404 (2009).

[61] K. L. Man, M. C. Tringides, M. M. T. Loy, and M. S. Altman, Phys. Rev. Lett. **101**, 226102 (2008).

[62] S. M. Binz, M. Hupalo, and M. C. Tringides, Phys. Rev. B **78**, 193407 (2008).

[63] C. M. Wei and M. Y. Chou, Phys. Rev. B **66**, 233408 (2002).

[64] A. Goldmann, V. Dose, and G. Borstel, Phys. Rev. B **32**, 1971 (1985).

[65] R. Otero, A. L. Vázquez de Parga, and R. Miranda, Phys. Rev. B **66**, 115401 (2002).

[66] H. Okamoto, in *Binary alloy phase diagrams*, edited by T. B. Massalski (ASM International, Metals Park, 1991).

[67] K. Gürtler and K. Jacobi, Surf. Sci. **134**, 309 (1983).

[68] A. Krupski and S. Mróz, Surf. Rev. Lett. **10**, 843 (2003).

[69] B. Dodson, Phys. Rev. Lett. **60**, 2288 (1988).

[70] N. Otsu, IEEE Transactions on Systems, Man, and Cybernetics **9**, 62 (1979).

[71] Y. Jia, B. Wu, H. H. Weitering, and Z. Zhang, Phys. Rev. B **74**, 035433 (2006).

[72] K. Pussi *et al.*, Surf. Sci. **603**, 2759 (2009).

[73] I. Bartos *et al.*, Surf. Sci. **402-404**, 697 (1998).

[74] R. C. Jaklevic and L. C. Davis, Phys. Rev. B **26**, 5391 (1982).

[75] K. Horn *et al.*, Phys. Rev. B **30**, 1711 (1984).

[76] Y. S. Li, F. Jona, and P. M. Marcus, Phys. Rev. B **43**, 6337 (1991).

[77] H. Yamauchi, K. Takagi, I. Yuito, and U. Kawabe, Appl. Phys. Lett. **29**, 638 (1976).

[78] L. Vitos, A. Ruban, H. Skriver, and J. Kollár, Surf. Sci. **411**, 186 (1998).

[79] I. Markov, *Crystal growth for beginners: fundamentals of nucleation, crystal growth and epitaxy* (World Scientific Singapore, Singapore, 2003).

[80] M. Hupalo and M. Tringides, Phys. Rev. B **75**, 235443 (2007).

[81] L. Kuipers and J. Frenken, Phys. Rev. Lett. **70**, 3907 (1993).

[82] M. Nowicki, C. Bombis, A. Emundts, and H. Bonzel, Phys. Rev. B **67**, 075405 (2003).

[83] H. Brune *et al.*, Phys. Rev. B **52**, R14380 (1995).

[84] B. Poelsema, J. B. Hannon, N. C. Bartelt, and G. L. Kellogg, Appl. Phys. Lett. **84**, 2551 (2004).

[85] J. Heyraud and J. Métois, Surf. Sci. **128**, 334 (1983).

[86] S. Surnev *et al.*, J. Vac. Sci. Technol. **A 16**, 1059 (1998).

[87] M. Sano, T. Adaniya, T. Fujitani, and J. Nakamura, J. Phys. Chem. B **106**, 7627 (2002).

[88] Y.-W. Mo, D. E. Savage, B. S. Swartzentruber, and M. G. Lagally, Phys. Rev. Lett. **65**, 1020 (1990).

[89] A. J. Steinfort *et al.*, Phys. Rev. Lett. **77**, 2009 (1996).

[90] A. T. Paxton, M. Methfessel, and H. M. Polatoglou, Phys. Rev. B **41**, 8127 (1990).

[91] H. Wormeester, E. Hüger, and E. Bauer, Phys. Rev. Lett. **77**, 1540 (1996).

[92] H. Wormeester, E. Hüger, and E. Bauer, Phys. Rev. Lett. **81**, 854 (1998).

[93] W. Wulfhekel *et al.*, Phys. Rev. B **64**, 144422 (2001).

[94] H. Wormeester, M. Kiene, E. Huger, and E. Bauer, Surf. Sci. **377**, 988 (1997).

[95] E. Bauer, H. Poppa, G. Todd, and F. Bonczek, J. Appl. Phys. **45**, 5164 (1974).

[96] G. A. Attard and D. A. King, Surf. Sci. **188**, 589 (1987).

[97] P. Hu *et al.*, Surf. Sci. **286**, L542 (1993).

[98] M. Harrison, D. Woodruff, and J. Robinson, Surf. Sci. **572**, 309 (2004).

[99] F. Buatier de Mongeot *et al.*, Phys. Rev. Lett. **91**, 016102 (2003).

[100] S. van Dijken, L. C. Jorritsma, and B. Poelsema, Phys. Rev. B **61**, 14047 (2000).

[101] L. Bruce and H. Jaeger, Philos. Mag. A **37**, 337 (1978).

[102] M. Zinke-Allmang, L. C. Feldman, and M. H. Grabow, Surf. Sci. Rep. **16**, 377 (1992).

[103] K. Morgenstern, G. Rosenfeld, and G. Comsa, Phys. Rev. Lett. **76**, 2113 (1996).

[104] R. van Gastel *et al.*, Phys. Rev. Lett. **86**, 1562 (2001).

[105] J. E. Demuth, P. M. Marcus, and D. W. Jepsen, Phys. Rev. B **11**, 1460 (1975).

[106] A. Grudniewski and S. Mroz, J. Phys. C Solid State **18**, 3387 (1985).

[107] M. S. Hoogeman *et al.*, Rev. Sci. Instrum. **69**, 2072 (1998).

[108] P. Rahe *et al.*, Rev. Sci. Instrum. **82**, 063704 (2011).

[109] M. Frigo and S. G. Johnson, Proceedings of the IEEE **93**, 216 (2005).

[110] B. A. Mantooth, Z. J. Donhauser, K. F. Kelly, and P. S. Weiss, Rev. Sci. Instrum. **73**, 313 (2002).

[111] J. C. Russ, *The Image Processing Handbook*, 5 ed. (CRC Press, Inc., Boca Raton, FL, USA, 2006).

[112] M. J. J. Jak *et al.*, Surf. Sci. **494**, 43 (2001).

[113] W. H. Press, S. A. Teukolsky, W. T. Vetterling, and B. P. Flannery, *Numerical Recipes in C: The Art of Scientific Computing* (Cambridge University Press, New York, NY, USA, 1992).

[114] N. Devillard, Fast Median Search: an ANSI C implementation, http://www.eso.org/ndevilla/median/.

[115] Q. Huang, W. Gaoa, and W. Caib, Pattern Recogn. Lett. **26**, 801 (2005).

[116] R. Rodriguez, Comput. Meth. Prog. Bio. **82**, 1 (2006).

Summary

Thin film growth is governed by a delicate balance between thermodynamic parameters and kinetic barriers. In the case that the latter can be easily overcome, each of the classical growth modes denoted by Franck-Van der Merwe, Stranski-Krastanov or Volmer-Weber may occur. In the latter cases accumulated strain is often an important factor. In the 1990s a novel growth mode was found, which resembles Stranski-Krastanov growth, but is qualitatively different from the classical growth modes in that quantum size effects (QSEs) seem to dominate, leading to non-trivial smooth film growth described as electronic or quantum growth. In this novel growth mode, the growth of thin Pb(111) films has attracted particular interest, since its Fermi wavelength is nearly commensurate to the bilayer atomic spacing and QSE driven growth sometimes persists even over 30 layer thick islands. Another candidate we propose is Bi, since the Fermi energy calculated from a free electron model of bulk Bi is only slightly higher than Pb. Besides that, Bi is also a soft metal, making electronic effects more pronounced than strain effects. This property makes thin Bi films prime candidates for allotropism and a candidate for electronic growth. QSEs are usually found on surfaces with a bandgap in the surface projected bulk bands, making a direct coupling between the electrons of the film and the substrate bulk impossible. Examples are Cu(111) and Ag(111), but Ni(111) just misses such a bandgap. However, the intrinsic modification of the electronic properties of the Ni(111) surface by the mere presence of a Bi- or Pb-film may just suffice to generate a situation with a surface projected bandgap. This would enable quantum well states which is also subject of the present study.

Using a combination of (I/V-) Low Energy Electron Microscopy (LEEM) and selective area (I/V-) Low Energy Electron Diffraction (μLEED) in combination with modeling and Tensor LEED calculations, we investigated the growth of thin metal layers and nanostructures on both Ni(111) and W(100), thereby showing growth dominated by respectively QSEs and strain, which may be further complicated by surface alloying.

In Chapter 3, we presented LEEM and μLEED measurements illustrating indeed the QSE driven growth of thin Bi film structures on Ni(111). The measured I/V-LEEM curves show well-defined quantum-size oscillations, that are in agreement with the results of a simple Kronig Penney (KP) model for three and five layer thick films. Three different film structures, characterized as (3×3), $\begin{bmatrix} 3 & -1 \\ 1 & 2 \end{bmatrix}$, and (7×7), grow at very specific heights of 3, 5 and 7 atomic layers. Comparing Tensor LEED calculations to I/V-μLEED curves we are able to calculate the interlayer distance, and therefore the height of these film structures. The structure heights perfectly accommodate $n/2$ times their Fermi wavelength, thereby illustrating the relevance of the QSE for quantization of island heights and ultimate film structure.

The formation of self-assembled nanostructures through a stabilizing interaction can be further complicated by surface alloying. Examples of this are the observed nanowires and the Bi-rich wetting layer, which are both formed before nucleation of the QSE driven stabilized structures just mentioned. Using LEEM and μLEED, we have characterized both the (7×7) wetting layer and $BiNi_9$ nanowires in Chapter 4. The nanowires show lengths up to about 10 μm and are only about 60 nm wide. Making use of I/V-μLEED data we found the height of the nanowires to be 4-6 atomic layers with respect to the substrate. The nanowires assume a $\begin{bmatrix} 2 & 0 \\ -2 & 5 \end{bmatrix}$ superstructure, containing 90% Ni. They have an fcc stacking with each fifth (113) intercalated plane containing 50% Bi. Due to the incomplete dealloying of the $(\sqrt{3} \times \sqrt{3})$-R30° surface alloy at coverages $\theta_{Bi/Ni} > 0.33$ ML, the (7×7) wetting layer in fact comprises two layers of which the lower one, the top substrate layer, contains a small but finite Bi content. The (7×7) wetting layer may contain a minor fraction of Ni. Upon the QSE driven growth of three and five layer high structures on top of the bare Ni(111) substrate, dealloying of the wetting layer and nanowires results in meandering of substrate steps in the step down direction, as is imaged with LEEM.

In comparison to the key examples of QSEs, i.e. Pb films on Si(111) and Ge(111), we also show QSE driven growth for Pb on Ni(111) in Chapter 5. First, a one layer high wetting layer develops consisting of small (7×7) and (4×4) domains, where the former has a stronger binding to the Ni(111) substrate. This results in the accumulation of tensile lateral stress, forcing the system to relieve this by allowing the growth of compressively stressed (4×4) domains. Since the density in both domains is very similar and their azimuthal orientation is identical, the domain wall energy will be low. These low energy cost domain walls result in small domain sizes. For coverages $\theta_{Pb/Ni} > 0.55$ ML, QSE driven Pb mesas form, which are embedded in the wetting layer. We have shown distinct QSE driven preferred heights for the Pb mesas in a number of specific examples for relatively thin and thick films. This is apparent from island height transitions both on wide terraces as well as at substrate steps. The average island heights that evolve during deposition at 422 K and 474 K show a clear signature of QSE driven preferred heights, distinctly including stable heights of 5, 7 and 9 atomic layers. These correspond nicely to the values obtained in the key examples of QSEs mentioned.

An unanticipated observation is highlighted in Chapter 6, where the approximately 40 layer high Pb mesas decay within 1 - 10 ms at about 526 K to form compact 3D-structures, induced by a thermal instability in the bi-domain wetting layer. The delicate balance between surface energies, elastic energies and QSEs is initially tilted towards QSEs, as the discrete layer heights are observed. When the character of the film gradually changes from 2D to 3D, the balance between these forces becomes more and more dominated by interfacial energies mainly between film and vacuum, until it reaches a tipping point. The sudden decay of the QSE stabilized mesas is indeed just that, as the energetic balance is

tipped for good in favor of the surface free energy towards a compact structure, thereby reducing the interfacial free energy. The spectacular speed at which the transition takes place is many orders of magnitude larger than what is expected on the basis of atomistic models for Pb on bulk.

As an example of strain dominated growth, we studied the morphology and structure of Cu on W(100), a system with a large misfit, in Chapter 7. Growth can be complicated for noble metals like Cu, which has different crystal structures that are energetically close to its equilibrium one. With its equilibrium fcc structure, Cu e.g. can be grown in a hcp- or bcc structure, depending on the substrate properties. During deposition at 674 K, we observe strong 3D growth of hut shaped Cu crystallites having steep facets. The μLEED data suggest that these crystallites predominantly have a hcp structure with a high density of stacking faults and the $(11\bar{2}0)$ plane parallel to W(100). From the measured facet diffraction spots, we obtain facet angles of about 54°. We note that the boundary between the Cu crystallite and the W(100) surface with the pseudomorphic Cu wetting layer crosses the close packed W azimuth directions at an angle of 11°. This can be explained by the complete cancellation of shear forces exerted by the hcp Cu crystallite on the underlying W(100) for an ideal $(ABAC)_n$ stacking of the hcp$(11\bar{2}0)$ like crystallite.

Upon slow heating, the pseudomorphic Cu layer transforms into a surface alloy at 815 K. This surface shows small coexisting domains of Cu-rich $p(2 \times 2)$ and $p(2 \times 1)$ ordering. Increasing the temperature to 950 K results in the decay of the hut shaped structures. From the island decay we derive a characteristic radial decay rate, indicating desorption into vacuum. The hcp-like islands leave footprints that show $p(2 \times 1)$ ordering. The $p(2 \times 1)$ domains grow in lateral size, by further desorbing Cu. Only slightly before complete desorption, small $c(2 \times 2)$ domains are found.

We thereby showed the influence of and subtle balance between QSE and strain stabilizing interactions on the growth, structural and electronic properties of nanostructures. Our results illustrate the generic need to characterize both the structural and electronic properties of nanostructures since small excursions away from equilibrium might lead to dramatic structural and/or electronic changes.

Samenvatting

De groei van dunne films wordt beheerst door een subtiel evenwicht tussen thermodynamische parameters en kinetische barrières. In het geval dat de kinetische barrières gemakkelijk overwonnen kunnen worden, kan elk van de klassieke groei-modi, Franck-Van der Merwe, Stranski-Krastanov of Volmer-Weber, optreden. Opgebouwde spanning speelt in de laatste twee gevallen vaak een belangrijke rol. In de jaren '90 werd een nieuwe groei modus gevonden, die lijkt op Stranski-Krastanov groei, maar kwalitatief verschillend is van de klassieke groei modi doordat Quantum Size Effecten (QSE) lijken te domineren. Dit leidt tot niet voor de hand liggende gladde film groei omschreven als elektronische of quantum groei. In deze nieuwe groei modus, trok de groei van dunne Pb(111) films in het bijzonder de aandacht, omdat daar de Fermi golflengte bijna passend is aan de dubbele interlaag afstand en omdat QSE gedreven groei soms zelfs nog bij meer dan 30 lagen dikke films voorkomt. Een andere kandidaat die we voorstellen is Bi, omdat de Fermi-energie van bulk Bi, berekend op basis van het vrije elektron model, slechts iets hoger is dan die van Pb. Daarnaast is Bi ook een zacht metaal, waardoor elektronische effecten een meer uitgesproken rol spelen dan spanningseffecten. Deze eigenschappen tezamen maken dunne Bi films een goede kandidaat voor allotropie en elektronische groei. QSE zijn meestal te vinden op oppervlakken met een bandgap in de, op het oppervlak geprojecteerde, bulk bandenstructuur, die een directe koppeling tussen de elektronen van de film en de substraat bulk onmogelijk maakt. Voorbeelden daarvan zijn Cu(111) en Ag(111). Ni(111) mist echter een dergelijke bandgap. De intrinsieke wijziging van de elektronische eigenschappen van het Ni(111) oppervlak door de aanwezigheid van een Bi- of Pb-film kan echter al volstaan om een situatie met een oppervlak geprojecteerde bandgap te creëren. Dit zou quantum well toestanden kunnen toelaten, die ook onderwerp van deze studie zijn.

Met behulp van (I/V-) Lage Energie Elektronen Microscopie (LEEM) en oppervlakte selectieve (I/V-) Lage Energie Elektronen Diffractie (μLEED) in combinatie met modellering en Tensor LEED berekeningen, hebben we onderzoek gedaan naar de groei van dunne metaal films en nanostructuren op zowel Ni(111) als W(100). Daarbij wordt de groei gedomineerd door respectievelijk QSE en spanning, maar hij kan zelfs nog gecompliceerder worden door oppervlakte legering.

In Hoofdstuk 3, presenteerden we LEEM en μLEED metingen die inderdaad de verwachte QSE gedreven groei van dunne Bi films op Ni(111) illustreren. De gemeten I/V-LEEM curves tonen goed gedefinieerde quantum-size oscillaties, die in overeenstemming zijn met de resultaten van een eenvoudig Kronig Penney (KP) model voor de drie en vijf lagen dikke films. Drie verschillende filmstructuren, gekenmerkt als (3×3), $\left[\begin{smallmatrix} 3 & -1 \\ 1 & 2 \end{smallmatrix}\right]$ en (7×7), groeien met zeer specifieke hoogtes. Die zijn respectievelijk 3, 5 en 7 atomaire lagen. Door het vergelijken

van Tensor LEED berekeningen met I/V-μLEED curves zijn we in staat om de interlaag afstanden te bepalen, en daarmee de film hoogtes. De hoogtes van de structuren laten een perfecte passing zien voor $n/2$ maal de Fermi golflengte en illustreren daarmee het belang van QSE voor de kwantisatie van de eiland hoogte, als ook voor de uiteindelijke film structuur.

De vorming van zelfgeordende nanostructuren door middel van een stabiliserende interactie kan verder worden gecompliceerd door de vorming van oppervlakte legering(en). Voorbeelden hiervan zijn de waargenomen nanodraden en de Bi-rijke wetting laag, die beide gevormd worden voordat de QSE gedreven structuren ontstaan. Met behulp van LEEM en μLEED, hebben we zowel de (7×7) wetting laag als ook de $BiNi_9$ nanodraden gekarakteriseerd in Hoofdstuk 4. De nanodraden hebben lengtes van ongeveer 10 μm en zijn daarbij slechts ongeveer 60 nm breed. Door gebruik te maken van I/V-μLEED data, bepaalden we de hoogte van de nanodraden. Die zijn 4-6 atomaire lagen dik ten opzichte van het substraat. De nanodraden nemen een $\begin{bmatrix} 2 & 0 \\ -2 & 5 \end{bmatrix}$ superstructuur aan, met daarin 90% Ni. Ze hebben een fcc stapeling waarbij elk vijfde (113) intercalatie vlak 50% Bi bevat. Als gevolg van de onvolledige ontmenging van de $(\sqrt{3} \times \sqrt{3})$-R30° oppervlakte legering voor bedekkingen $\theta_{Bi/Ni} > 0.33$ ML, bestaat de (7×7) wetting laag in feite uit twee lagen. De onderste daarvan, de bovenste laag van het substraat, bevat een kleine hoeveelheid Bi. De (7×7) wetting laag kan een kleine fractie van Ni bevatten. De groei van QSE gedreven drie en vijf laag hoge structuren bovenop het Ni(111) substraat, resulteren in meanderende substraat stappen in aflopende richting. Dit wordt veroorzaakt door de ontmenging van de wetting laag en de nanodraden, die we hebben afgebeeld met de LEEM.

In vergelijking met de belangrijkste voorbeelden van QSE, nl. Pb films op Si(111) en Ge(111), hebben we ook QSE gedreven groei laten zien voor Pb op Ni(111) in Hoofdstuk 5. In het begin groeit er één enkele wetting laag, die bestaat uit kleine (7×7) en (4×4) domeintjes, waarbij de eerste een sterkere binding met het Ni(111) substraat hebben. Dit resulteert in de opbouw van laterale trekspanning, die het systeem compenseert met de groei van de (4×4) domeintjes met drukspanning. Aangezien de dichtheid in beide domeinen zeer vergelijkbaar is en hun azimutale oriëntaties dezelfde zijn, zal de energie van de domeingrenzen laag zijn. Deze 'goedkope' domeingrenzen resulteren in kleine domeinen. Voor de bedekkingen $\theta_{Pb/Ni} > 0.55$ ML, zien we QSE gedreven Pb mesas vormen, die zijn ingebed in de wetting laag. We hebben duidelijke QSE gedreven voorkeurshoogtes voor de Pb mesas laten zien in een aantal specifieke voorbeelden voor zowel relatief dunne als ook dikke films. Deze voorkeurshoogtes blijken uit de eiland hoogteovergangen die plaatsvinden op zowel brede terrassen als op substraat stappen. De gemiddelde eiland hoogtes die we tijdens de depositie op 422 K en 474 K waarnemen, tonen een duidelijk beeld van de QSE gedreven geprefereerde hoogtes van 5, 7 en 9 atomaire lagen. Deze hoogtes komen goed overeen met de hoogtes gevonden in de belangrijkste voorbeelden

van QSE.

Een onverwachte observatie is beschreven in Hoofdstuk 6, waar de circa 40 lagen hoge Pb mesas binnen 1 - 10 ms bij een temperatuur van ongeveer 526 K compacte 3D-structuren vormen. Dit wordt veroorzaakt door een thermische instabiliteit in de bi-domein wetting laag. Het subtiele evenwicht tussen de oppervlaktevrije energie, elastische energie en QSE is in eerste instantie in het voordeel van de QSE, waarvan we dan ook de discrete laag hoogtes zien. Wanneer het karakter van de film geleidelijk van 2D naar 3D verandert, wordt het evenwicht tussen deze krachten meer en meer gedomineerd door grensvlak energieën, met name tussen film en vacuüm, tot het omslagpunt wordt bereikt. Het plotselinge verval van de QSE gestabiliseerde mesas wordt inderdaad veroorzaakt doordat de energetische balans voorgoed in het voordeel van de oppervlakte vrije energie omslaat. Het gevolg is een compacte structuur, waarbij de grensvlak vrije energie is verminderd. De spectaculaire snelheid waarmee de overgang plaatsvindt is vele ordes van grootte groter dan wat men zou verwachten op basis van atomaire modellen voor Pb op bulk.

Als een voorbeeld van spanning gedomineerde groei, bestudeerden we in Hoofdstuk 7 de morfologie en structuur van Cu op W(100), een systeem met een slechte passing. Groei kan gecompliceerd zijn voor edele metalen zoals Cu, die ook andere kristalstructuren energetisch dicht bij zijn evenwichtsstructuur heeft. Met zijn fcc evenwichtsstructuur, kan Cu bijvoorbeeld worden gegroeid in een hcp- of bcc-structuur, afhankelijk van de eigenschappen van het substraat waarop het wordt gegroeid. Tijdens de depositie op 674 K, zien we een sterke 3D groei van Cu kristallieten die een hutvorm met steile facetten laten zien. De μLEED data suggereren dat deze kristallieten vooral een hcp-structuur met een hoge dichtheid van stapelfouten heeft, waarbij het $(11\bar{2}0)$ vlak evenwijdig aan W(100) is. Uit de gemeten facet posities, bepalen we facet hoeken van ongeveer 54°. We merken daarbij op dat de grens tussen het Cu kristalliet en het W(100) oppervlak met de pseudomorfe Cu wetting laag de dicht gepakte W azimut richtingen doorkruist met een hoek van 11°. Dit kan worden verklaard door de ideale $(ABAC)_n$ stapeling van het hcp$(11\bar{2}0)$ kristalliet, wat resulteert in een volledige opheffing van de schuifspanning, die wordt uitgeoefend door de hcp Cu kristallieten op het onderliggende W(100).

Bij langzame verwarming, transformeert de pseudomorfe Cu laag bij 815 K in een oppervlakte legering. Dit oppervlak toont kleine co-existerende domeinen van de Cu-rijke $p(2 \times 2)$ en $p(2 \times 1)$ ordening. Het verhogen van de temperatuur tot 950 K resulteert in het verval van de hutvormige structuren. Uit het eiland verval leiden we een karakteristiek radiëel verval af, wat we verklaren met Cu desorptie in het vacuüm. De hcp-achtige eilanden laten daarbij afdrukken achter die $p(2 \times 1)$ ordening laten zien. De $p(2 \times 1)$ domeinen groeien vervolgens lateraal door meer Cu te desorberen. Kleine $c(2 \times 2)$ domeintjes ontstaan slechts kort voordat volledige desorptie van het Cu plaatsvindt.

We hebben de invloed van, en de subtiele balans tussen QSE en spanning stabiliserende interacties laten zien op zowel de groei, als ook op de structurele en

elektronische eigenschappen van nanostructuren. Onze resultaten laten de algemene noodzaak zien om zowel de structurele als ook de elektronische eigenschappen van nanostructuren te karakteriseren. Kleine uitwijkingen weg van het evenwicht kunnen immers leiden tot dramatische structurele en/of elektronische veranderingen.

Dankwoord

Een proefschrift is en blijft een wetenschappelijke proeve van bekwaamheid. Veel personen hebben hun steentje daaraan bijgedragen, in allerlei vormen. Ik wil daarom graag van de gelegenheid gebruik maken om iedereen te bedanken die bij dit onderzoek betrokken is geweest, voor het enthousiasme en vertrouwen dat ze me hebben gegeven.

Enkele personen wil ik echter in het bijzonder bedanken:

Prof. dr. ir. B. Poelsema. Beste Bene, net voor mijn afstuderen heb je me gevraagd om bij je te komen promoveren. Met name je eerlijkheid, begrip en natuurlijk je onuitputtelijke wetenschappelijke input in mijn onderzoek heb ik altijd zeer gewaardeerd. Dank voor deze kans tijdens het spitsuur van mijn leven.

Prof. dr. J.W.M. Frenken. Beste Joost, dank voor je interesse als tweede promotor. Je kritische blik en expertise hebben zeker hun vruchten afgeworpen.

Dr. R. van Gastel. Beste Raoul, dank voor je hulp over de gehele linie bij mijn onderzoek. Je hebt me thuisgebracht in de wereld van de LEEM en het werken met UHV in al zijn aspecten.

Dr. ir. H. Wormeester. Beste Herbert, dank voor de gezellige en uiterst leerzame tijd in Grenoble en je hulp bij de interpretatie van resultaten wat leidde tot Hoofdstuk 7. Je aanstekelijke enthousiasme en enorme parate kennis zullen me nog lang bijblijven.

Ook dank aan alle **ondersteuning** vanuit de groep. Hans en Herman, dankzij jullie snelle en enthousiaste inzet was ik met panne aan de LEEM telkens weer snel op weg.

Ik wil ook al mijn (oud-)**collegæ** bedanken voor hun bijdrage in de groep. Mijn kamergenoten Fawad en Gregor, Vasilisa en James voor de fijne tijd. Frank, bedankt voor de gezelligheid en onze (praktische) discussies, zowel in Grenoble als in Twente. James, bedankt voor je aanstekelijke wetenschappelijke enthousiasme en onze discussies op vele vlakken.

Dank ook aan alle **familie, (muziek) vrienden en kennissen** die altijd weer oprecht hun interesse in mijn onderzoek toonden. Ook al werd mijn uitleg over mijn werk al snel gedetailleerd, jullie bleven altijd geïnteresseerd.

Natuurlijk ook dank aan **mijn vader**(†) **en moeder** voor jullie onvoorwaardelijke steun, vertrouwen en eeuwige liefde. Waar zou ik zonder dat alles zijn geweest. Pap, ik weet dat je trots op me bent.

Tot slot: **Sherien**! Zonder jouw hulp en steun was dit natuurlijk nooit mogelijk geweest. Zoals men zegt: achter elke succesvolle man staat een sterke vrouw. Vooral jij hebt heel wat offers moeten brengen, waarvoor mijn dank. Samen met onze **Avira** weet je alles weer te relativeren en in het juiste perspectief te plaatsen. Ik ben iedere dag weer innig dankbaar met jullie in mijn leven.

Tjeerd Bollmann

Curriculum Vitæ

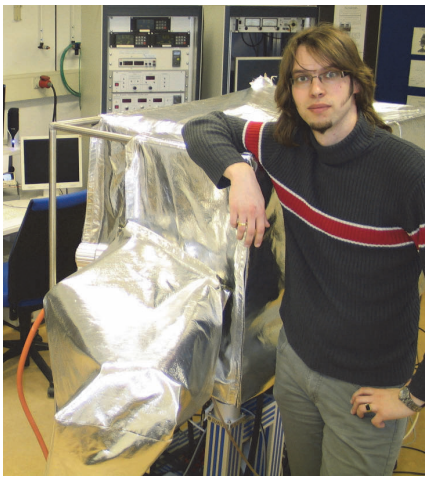

The LEEM prepared for bake-out.

Tjeerd Bollmann was born in Doetinchem on November 8, 1982. He finished his pre-university education (VWO) at the Almende College in Silvolde in 2001.

Then he studied Applied Physics at the University of Twente where he finished his B.Sc. in 2004. A nine months internship was carried out at the Chemical Particle Technology (CPT) group of Akzo Nobel Chemicals, Arnhem, under the supervision of dr. Paul Verwer where he studied dynamical microphase modeling.

The nine months graduate research were a combined study of Molecular Dynamics (MD) and Kinetic Monte-Carlo (KMC) simulations and Scanning Tunneling Microscopy (STM) experiments on the sputtering processes on Cu(001) done within the Solid State Physics group at the University of Twente under supervision of prof. dr. ir. Bene Poelsema and dr. ir. Herbert Wormeester.

In August 2006 Tjeerd obtained his M.Sc. degree with distinction and accepted the Ph.D. position in the same group. His research in this period resulted in several papers, conference contributions and finally this thesis.

Besides being a graduate student, Tjeerd is a proud father and has a passion for music. After playing several instruments in several bands he started to develop as a conductor in 1999. Since then he orchestrates and lead several bands which resulted in conducting the choirs Jong Vocaal (Bentelo), Vocal Motion (Steenderen) and Westendorps Fanfare (Westendorp) where he has been for several years now.